DNA Tetrahedra as Structural Frameworks for Catalytic Centers

by

Kimberly Nicole Rendek

A Dissertation Presented in Partial Fulfillment
of the Requirements for the Degree
Doctor of Philosophy

Approved November 2012 by the
Graduate Supervisory Committee:

Petra Fromme, Chair
Alexandra Ros
Julian Chen

ARIZONA STATE UNIVERSITY

December 2012

ABSTRACT

The need for a renewable and sustainable light-driven energy source is the motivation for this work, which utilizes a challenging, yet practical and attainable bio-inspired approach to develop an artificial oxygen evolving complex, which builds upon the principles of the natural water splitting mechanism in oxygenic photosynthesis. In this work, a stable framework consisting of a three-dimensional DNA tetrahedron has been used for the design of a bio-mimic of the Oxygen-Evolving Complex (OEC) found in natural Photosystem II (PSII). PSII is a large protein complex that evolves all the oxygen in the atmosphere, but it cannot be used directly in artificial systems, as the light reactions lead to damage of one of Photosystem II's core proteins, D1, which has to be replaced every half hour in the presence of sunlight. The final goal of the project aims to build the catalytic center of the OEC, including the Mn4CaCl metal cluster and its protein environment in the stable DNA framework of a tetrahedron, which can subsequently be connected to a photo-stable artificial reaction center that performs light-induced charge separation. Regions of the peptide sequences containing Mn4CaCl ligation sites are implemented in the design of the aOEC (artificial oxygen-evolving complex) and are attached to sites within the tetrahedron to facilitate assembly. Crystals of the tetrahedron have been obtained, and X-ray crystallography has been used for characterization. As a proof of concept, metal-binding peptides have been coupled to the DNA tetrahedron which allowed metal-containing porphyrins, specifically Fe(III) meso-Tetra(4-sulfonatophenyl) porphyrin chloride, to be encapsulated inside the DNA-

tetrahedron. The porphyrins were successfully assembled inside the tetrahedron through coordination of two terminal histidines from the orthogonally oriented peptides covalently attached to the DNA. The assembly has been characterized using Electron Paramagnetic Resonance (EPR), optical spectroscopy, Dynamic Light Scattering (DLS), and x-ray crystallography. The results reveal that the spin state of the metal, iron (III), switches during assembly from the high-spin state to low-spin state.

DEDICATION

I dedicate this dissertation to my parents, Pete and Debbie Rendek, my brother Greg Rendek, and my boyfriend Kyle Meehan. Thank you, Dad, for helping me discover the exciting world of science and research from a very young age and for inspiring me to pursue a professional degree in science. Thank you, all of you, for always believing in me and for encouraging me to pursue my dreams. This path would not have been possible without all of your love and support.

ACKNOWLEDGMENTS

First and foremost, I would like to thank my advisor, Dr. Petra Fromme, for her support and encouragement through the years and for inspiring me with her true passion for science. She is truly dedicated to sharing her knowledge with others and is also a talented teacher. Her enthusiasm for science is unparalleled, and she has shown me through the years what it means to be a true scientist. I am so fortunate to have been given the opportunity to spend the last several years working with Dr. Fromme.

I am grateful for the support and helpful discussions from my supervisory committee, Dr. Alexandra Ros and Dr. Julian Chen. I had set forth to strengthen my background in physics, physical chemistry, and analytical chemistry, and the courses in microfluidics and biochemistry helped significantly. Thank you for the helpful advice through the years with my research and fundamental understanding of chemistry.

I would like to thank Dr. Rob Lawrence and Jay-How Yang for all of the help they provided me with when I first started working in the lab. Rob and Jay-How showed me everything I know today about molecular biology, and it was a pleasure working with both of them. Thank you for also being great friends and sharing many fun times in and out of the lab.

A large portion of my understanding of isolating and purifying photosystems and crystallography comes from Dr. Ingo Grotjohann and Dr. Raimund Fromme. Thank you, Ingo and Raimund, for being so kind through the

years and always offering your help. We have had lots of great memories working together.

I would like to thank Michael Vaughn for showing me how to set up crystallization experiments. As a first year student, I had a lot of questions, and Michael was always willing to answer them and share with me his knowledge of biochemistry.

I would like to thank Chad Simmons, who was kind and showed me how to make different DNA structures and helped explain crystallography when I had lots of questions, and also Dr. Chenxiang Lin, for providing me with helpful advice while working on the DNA project. I would like to thank Dr. Hao Yan and Dr. Yan Liu for allowing me to work extensively in their lab to learn new techniques, and for sharing with me their expertise in DNA nanotechnology.

I would like to thank Dr. Andrei Astashkin at the University of Arizona for all of his hard work with analyzing our EPR samples. His extensive knowledge of EPR helped us obtain excellent data, and I have gained a lot of valuable knowledge from this collaboration.

The EFRC project is a large, interdisciplinary collaboration among several research groups, and I have been so fortunate to be a part of this. First, I would like to thank Dr. Devens Gust for offering me the opportunity to work on an exciting project within the EFRC to work on a solar-fuel system. Dr. Gust has always been so willing to advise me on many different projects and always has wonderful ideas.

I would like to thank Dr. Josifina Sarrou, who is one of the kindest people I have met during my graduate studies at ASU. She is very knowledgeable in many subjects and has always been so willing to help with so many things, especially explaining EPR to a biochemist! All of the porphyrin work would not have been possible without Josifina's help and encouragement. She has not only been a wonderful colleague, but has also become a great friend.

I would like to thank Jesse Bergkamp and Dr. Matthieu Koepf for being such kind, helpful colleagues with the porphyrin work. I have a much better understanding of porphyrins after working with both of you. Thank you also for the many fun times and many laughs and for being great friends as well as colleagues.

I would also like to thank Martha McDowell for always being so kind, helpful, and supportive of not only me but all of the chemistry and biochemistry graduate students.

Finally, the Department of Energy must be acknowledged for providing generous support for this work as part of the Center for Bio-Inspired Solar Fuel Production, an Energy Frontier Research Center funded by the U.S. Department of Energy, Office of Science, Office of Basic Energy Sciences under Award Number DE-SC0001016, which made all of this research possible.

TABLE OF CONTENTS

Page

CHAPTER Page

CHAPTER Page

CHAPTER Page

CHAPTER Page

CHAPTER Page

Page

LIST OF TABLES

LIST OF FIGURES

Figure Page

Figure Page

LIST OF SYMBOLS

Symbol	Definition
μL	microliter
μM	micromolar
20T	20T tetrahedron
20TP8P	tetrahedron-peptides-porphyrin
20x30T	20x30T tetrahedron
30T	30T tetrahedron
A_{260}	absorbance at 260 nm
A_{280}	absorbance at 280 nm
aOEC	artificial oxygen-evolving complex
ASU	Arizona State University
CT-D1	C-terminal D1 protein
CW	Continuous Wave
DLS	dynamic light scattering
DNA	deoxyribonucleic acid
EFRC	Energy Frontier Research Center
EPR	electron paramagnetic resonance
ETC	electron transport chain
kDa	kiloDalton
Mn	Manganese
MnCaCl	Manganese cluster
MW	molecular weight

OEC ..... oxygen-evolving complex

PEG ..... polyethylene glycol

rpm ..... revolutions per minute

SMCC ... succinimidyl-4-(N-maleimidomethyl)cyclohexane-1-carboxylate

1. INTRODUCTION

1.1 Oxygenic Photosynthesis

Photosynthesis is one of the most fascinating and important processes on Earth, as it enables light energy to be converted into chemical energy to provide organisms with necessary food and energy. The general reaction of photosynthesis is shown below.

$$6CO_2 + 6H_2O \rightarrow C_6H_{12}O_6 + 6O_2 \quad \textit{(in the presence of light)}$$

It is this pathway that paved the way for an oxygenic atmosphere for all higher life on Earth including humans to exist. In photosynthetic organisms, the electron transport chain consists of three large multimeric membrane complexes that are key components in generating chemical energy from solar energy. Oxygenic photosynthesis occurs in the thylakoid membranes of photosynthetic organisms.

Excitation energy transfer begins with the absorption of a photon by the peripheral antenna systems surrounding PSII and PSI. From there, excitation energy is transferred to P680 and P700, the primary donors in PSII and PSI which results in an excited state, leading to a charge separation event in the reaction centers [1,2]. The electrons for the electron transfer reactions come from the oxidation of $2H_2O$ to dioxygen, four protons, and four electrons catalyzed by the oxygen-evolving complex in PSII. Four electrons are subsequently extracted from two water molecules in the oxygen-evolving complex (OEC) which consists of a manganese-calcium cluster, causing the water to become oxidized to molecular oxygen (O_2) and released into the atmosphere, while four protons are released into the lumen and four electrons are provided for the electron transport

chain. The electrons from water are used to re-reduce $P680^+$ upon charge separation. The final electron acceptor in PSII is a mobile plastoquinone Q_B (PQ) which leaves PSII upon binding of 2 protons as plastoquinol (PQH_2). Electrons are transferred via PQH_2 to the cytochrome b_6f complex which pumps protons across the membrane and reduces the electron transfer protein plastocyanin, or cytochrome c_6 at the lumenal side which transfers the electrons to PSI. PSI catalyzes the second light-induced charge separation event. The excitation energy from the antenna chlorophylls is transferred to P700, the primary electron donor in PSI. Upon excitation, $P700^*$ donates an electron that is transferred along the electron transport chain to the terminal FeS cluster F_B from which it is transferred to ferredoxin, the soluble electron transfer protein located on the stromal side of the membrane. Ferredoxin transfers the electron to ferredoxin-$NADP^+$-reductase (FNR). Two ferredoxins dock subsequently to the FNR which reduces $NADP^+$ to NADPH [2]. During these electron transfer processes a proton gradient is formed across the thylakoid membrane, creating a pH difference (ΔpH) and electrochemical membrane potential. ΔpH and $\Delta\psi$ gradient drive the synthesis of ATP, via a rotational mechanism of the ATP synthase [F_0F_1]. ATP and NADPH are the high-energy products that drive synthesis of carbohydrates in the dark reactions of photosynthesis (the Calvin Cycle).

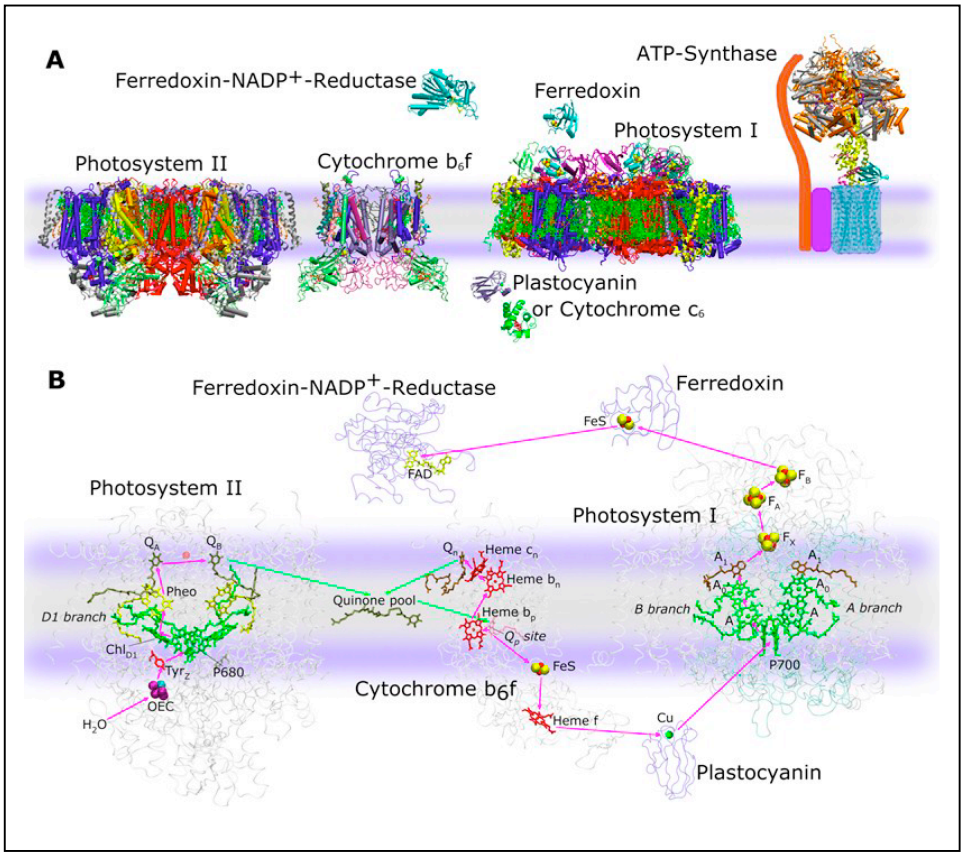

Figure 1.1. (A) A schematic of the electron transfer chain of photosynthesis and critical proteins involved in photosynthesis, and the electron transport chain (B). Figure used with permission from Dr. Petra Fromme.

1.2. Evolution of Oxygenic Photosynthesis and the Relevance of Photosystem II

Prior to the evolution of cyanobacteria 2.5 billion years ago on Earth, an anoxygenic environment persisted. Eventually, evolution of biomolecules such as pigments took place, which paved the way for the first anoxygenic photosynthetic organism to develop ~3.5 billion years ago by the use of water as an electron source for the photosynthetic transport chain. [3] Around 2.5 billion years ago, oxygenic photosynthesis was initiated and gave rise to new biosynthetic

pathways. Cyanobacteria thereby evolved 2.4 billion years ago from non-oxygenic photosynthetic ancestors, which resulted in oxygen production in the atmosphere. There are many current hypotheses for the invention of oxygenic photosynthesis; however it is known that O_2 appeared in the atmosphere 2.4 billion years ago, and many organisms were forced to adapt to the conditions. The "great oxygenation event" occurred between 2.0 and 2.4 billion years ago [4], when atmospheric oxygen increased to 1-2% and remained stable until 850 million years ago, when oxygen concentration in the atmosphere increased to 20%, as it remains today [3]. PSII is the protein responsible for oxidizing water into molecular oxygen, and without this, humans and other oxygen-dependent organisms would cease to exist.

1.3. Strucure of Photosystem II (PSII)

The initial light-driven charge separation events in oxygenic photosynthesis are catalyzed by two large membrane complexes: Photosystem II (PSII) and Photosystem I (PSI). Cyanobacterial PSII consists of 19 transmembrane subunits, including core reaction center proteins D1 (PsbA) and D2 (PsbD), core antenna proteins CP43 (PsbC) and CP47 (PsbB), and more than 50 cofactors. Cyanobacterial PSII also contains 3 extrinsic proteins (more extrinsic proteins are present in eukaryotes) which are critical in stabilizing the 4MnCa cluster and have been shown to be necessary for oxygen evolution – a 33 kDa "basket" shaped protein, PsbO, PsbV, and PsbU in cyanobacteria. Several pigments are also associated with PSII – 35 chlorophyll molecules, two

pheophytins, two plastoquinones, one non-heme iron, two hemes, and 11 β-carotenes. Additionally, more than 20 lipids are bound to PSII. The OEC contains four manganese atoms and one calcium atom. Furthermore, 2 Cl^- ions are located in the vicinity of the 4MCa cluster. Inaddition, two more Ca^{2+} and one more Cl^- have been identified in the most recent x-ray structures of PSII [5,6]. In nature, PSII is a dimer. The PSII monomer is 350 kDa in size, spanning about 10.4 nm (4.5 nm of which is in the membrane). The diameter of PSII is approximately 10 nm across. The dimer is found in all organisms. Monomers also exist but are very likely assembly intermediates. The dimensions of the dimer are 104 Å deep (45 Å is in the membrane), 205 Å long, and 110 Å wide.

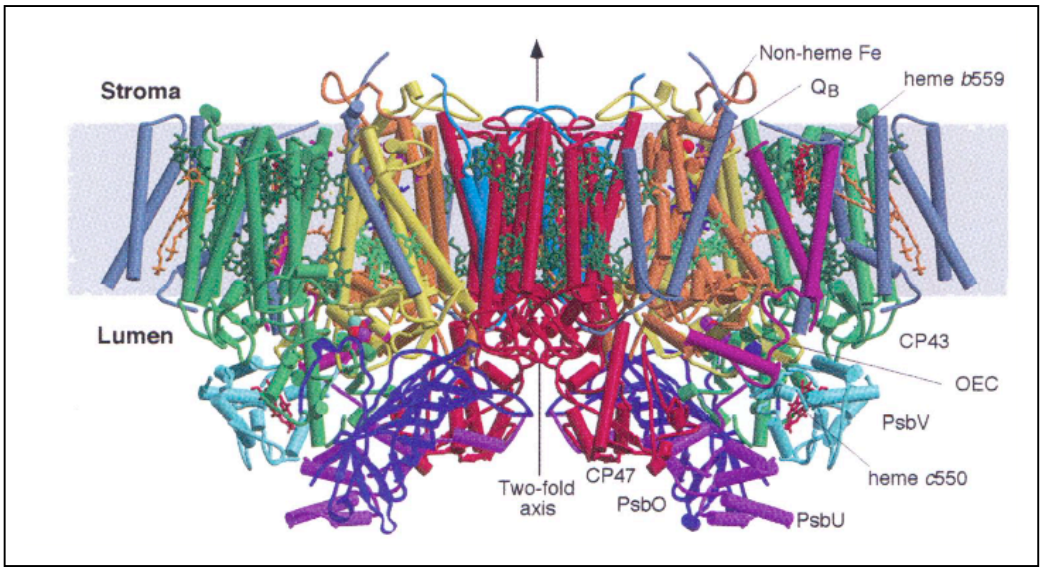

Figure 1.2. Photosystem II dimer depicting its subunits and environment surrounding the Mn cluster. Figure taken from reference [7]

1.4. PSII: Electron Transport Chain and its Role in Oxygenic Photosynthesis

PSII is the key protein in oxygenic photosynthesis because it is responsible for extracting the electrons from water that are utilized further down the electron transport chain. In addition, molecular oxygen (O_2) is a product of the water-splitting reaction and 4 protons are released into the lumen thereby contributing to the formation of the ΔpH gradient across the membrane. The sum reaction of water oxidation is given by:

$$2H_2O \rightarrow O_2 + 4H^+ + 4e^-$$ (in the presence of light)

Remarkably, PSII's main pigments responsible for catalysis of the charge separation, P680, are highly oxidizing, possessing a redox potential of +1.1V (in standard electrochemical conditions). This redox potential is one of the strongest oxidizing species known in a biological system.

The D1 and D2 membrane intrinsic subunits of PSII are responsible for forming the dimeric core and binding the cofactors of the electron transport chain (ETC). The PSII ETC consists of four pseudo-symmetrically oriented chlorophylls, two pheophytins, and two plastoquinones, as shown in Figure 1.3.

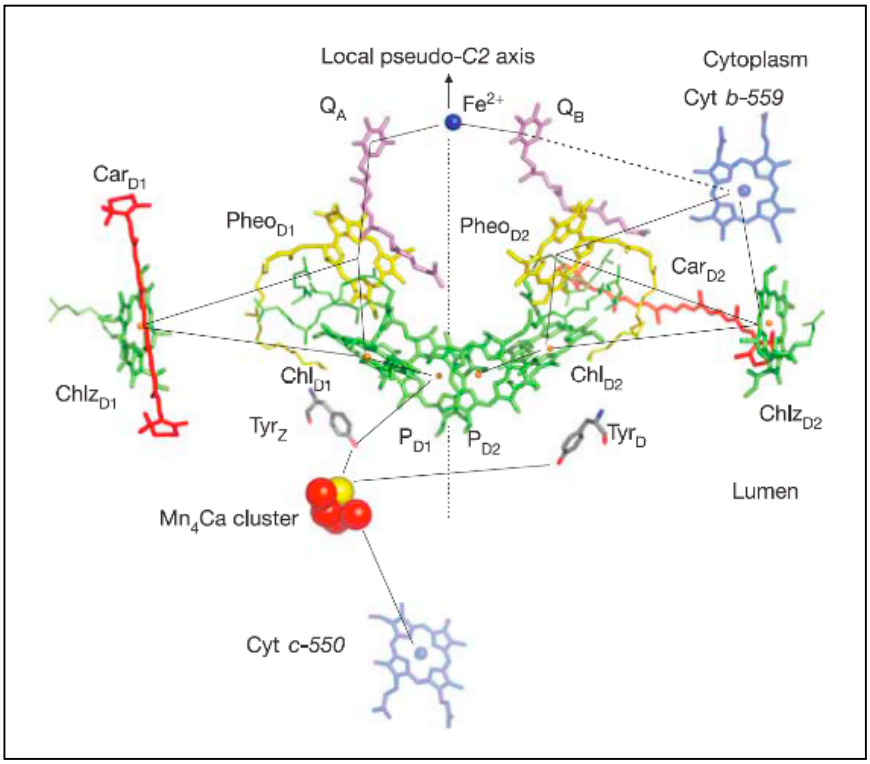

Figure 1.3. Detailed view of the electron transport chain in PSII. There are two branches shown in the electron transport chain, the D1 branch and the D2 branch. Figure taken from reference [8]

Upon excitation and energy transfer from the antenna chlorophylls, charge separation occurs at P680, the primary donor chlorophyll pair. Then one electron is accepted by the monomeric chlorophyll of the D1 branch and subsequently the pheophytin molecule on the D1 branch. Once the pheophytin is reduced, electron transfer proceeds to the tightly bound plastoquinone (Q_A) from where it is transferred to the mobile quinol PQ in the Q_B site, Once Q_B is doubly reduced by 2 charge separation events, Q_B is released as a neutral plastoquinol (PQH_2) into the membrane and replaced by a PQ from the pool of PQ molecules which is in the membrane. P680 is re-reduced by the OEC and this process is mediated by a

redox-active tyrosine residue (Y_Z) of the D1 protein. (Y161). Four photochemical turnovers provide the OEC with four oxidizing equivalents which drive it through the S-state cycle. Molecular oxygen is released during the S_4 to S_0 transition. [6,8]

1.5. Structure of the OEC

Many different techniques have been used in order to understand the structure of the OEC. It is known that the cluster is composed of four Mn atoms, five oxygens, and one calcium. A cubane-like structure is formed from three of the manganese atoms, one calcium, and four oxygens. The fourth Mn is linked to the cubane via a μ-oxo bridge [5], as shown in Figure 1.4 below. The amino acids that play an integral role in stabilizing the Mn cluster are depicted in green (from the D1 subunit) and pink (from the CP43 subunit). Glu189 provides one ligand to the Mn cluster, while Asp170, Glu333, Asp342, and Glu354 as shown below provide bidentate ligands to the Mn cluster [5]. His337 is linked to the cluster through an oxygen atom.

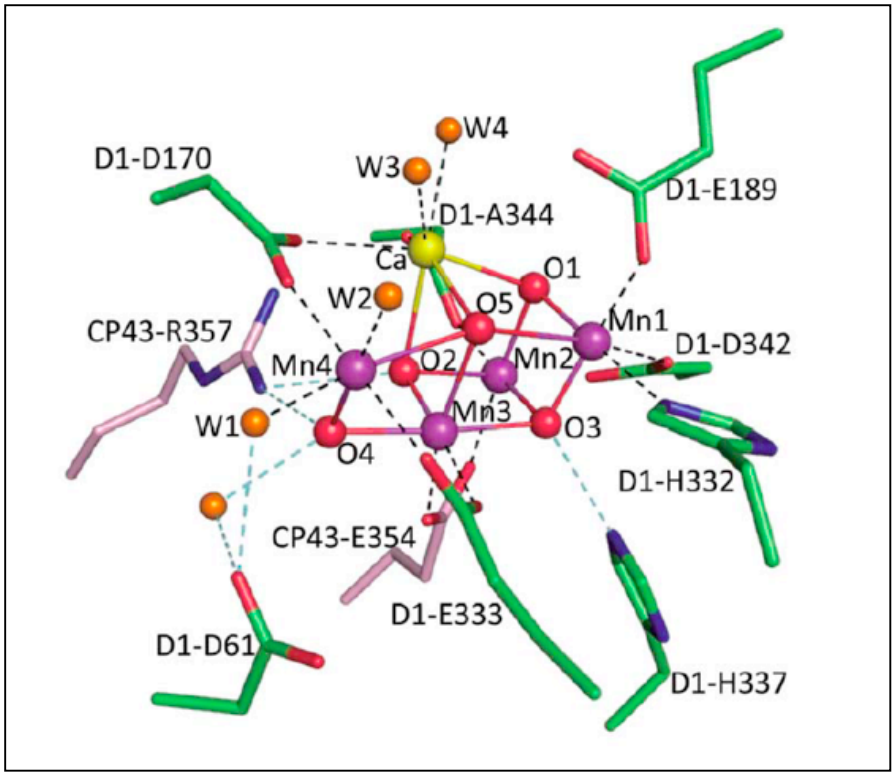

Figure 1.4. Structure of the manganese cluster in PSII to 1.9Å resolution, revealing how the critical amino acids ligate the Mn cluster. Figure taken from reference [5]

1.6. S-state Cycle of PSII and the State of the Manganese (Mn) Cluster

Probably the most elusive mechanism in nature is the S-state cycle in PSII. This is the cycle in which four successive light-driven turnovers result in oxidation of 2 water molecules and the formation of O_2. This mechanism is very sophisticated, and has been occurring for 2.5 billion years. In this mechanism, four oxidizing equivalents (most likely the mechanism is that in each step one proton and one electron are extracted) are accumulated at the OEC before O_2 is released. The OEC consists of four manganese atoms, five oxygen atoms, and one

calcium atom forming the Mn_4CaO_5 cluster. Three manganese, four oxygen, and one calcium atom form a cubane-like structure in the highest resolution (1.9Å) x-ray structure of PSII to date. (See Figure 1.4). However, the x-ray exposure reduces the Mn cluster, so whether or not the structure really represents the dark state is controversial. Many published EXAFS and XAS studies have explored the structure and mechanism of the MnCa cluster as well [9]. Furthermore, many models exist for the actual mechanism of water oxidation [10,11,12,13,14,15,16,17] but without an x-ray structure of the cluster in different S states it is still unknown how the actual water splitting mechanism works as the structures of each of the intermediates in the S-state cycle are still unresolved. This is the motivation for the PSII crystallization reported later in this work. A schematic of the S-state cycle is shown in Figure 1.5.

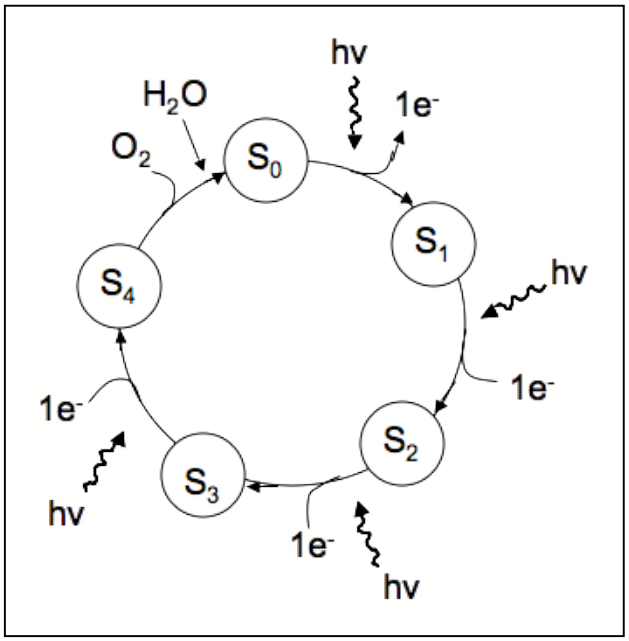

Figure 1.5. Schematic of the S-state cycle, as first described by Bessel Kok, et al [18,19]. This is a four-electron process, in that four electrons must be extracted

from water to evolve one molecule of oxygen. Oxygen is evolved in the $S_4 - S_0$ state.

1.7. Photodamage of PSII and In Vivo Repair Mechanisms

Excess energy, causes photodamage of PSII which is primarily caused by the triplet formation of P680. [20] However, even under moderate light conditions where no photoinhibition occurs, the chance of photodamage in PSII is roughly one in a million. PSII's subunit D2 is stable in the presence of light; however, D1 is turned over *in vivo* every half hour in direct sunlight [2]. The D1 protein, encoded by the gene psbA, has a very intricate mechanism for replacement. First, it is important to mention that PSII is disassembled in the damage-repair cycle, during which D1 and D2 are decoupled, and biosynthesis of D1 occurs independent of D2 before the protein is reassembled by a translational coupled mechanism [21]. Research conducted on D1 revealed that the D1 protein is synthesized as a precursor polypeptide containing anywhere from a 5-16 residue C-terminal extension that when inserted into the thylakoid lumen is cleaved by a peptidase following the light-induced assembly of two Mn atoms. The peptidase responsible for this process is CtpA, and studies have shown that without this cleavage process occurring, no oxygen-evolving activity was observed. In prior studies, it was found that the mature D1 protein is 2 kDa smaller than the precursor polypeptide, indicating that cleavage of a significant portion of the polypeptide occurs [22]. Figure 1.6 below shows the process of D1 turnover.

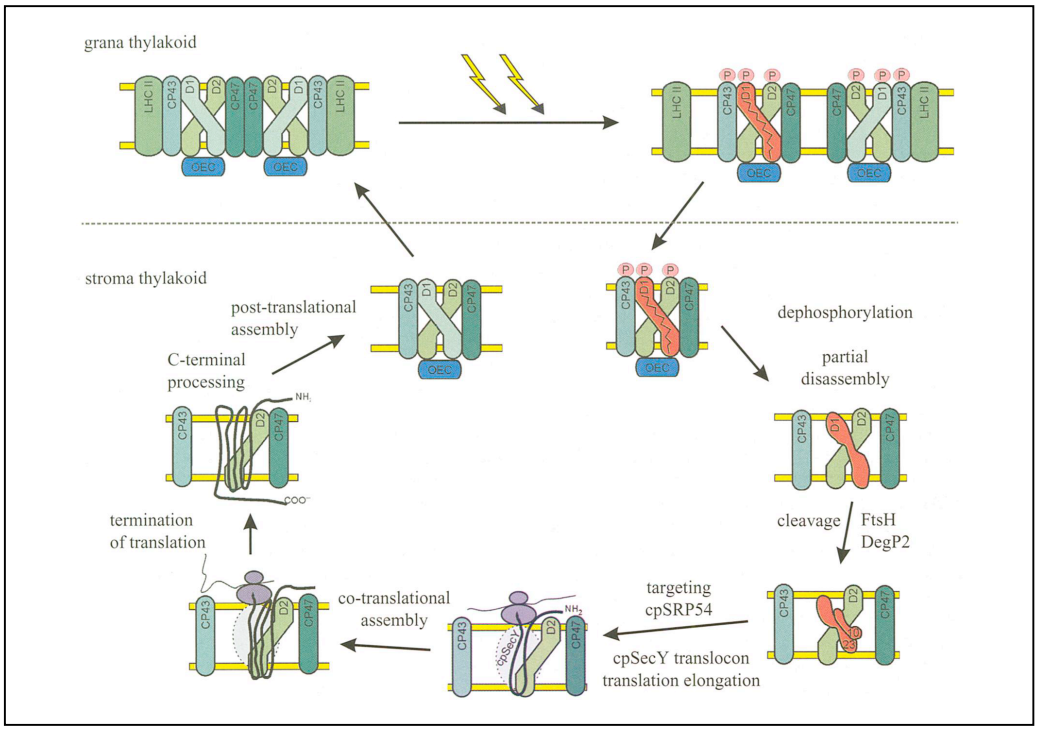

Figure 1.6. Damage-repair cycle of the D1 subunit of PSII. Figure taken from reference [21]. PSII has an elaborate repair mechanism which consists of the D1 and D2 subunits being decoupled (right side) in a degradation pathway, and D1 being co-translated in the presence of D2 before re-assembling.

This damage-repair cycle hinders the direct use of PSII for man-made water-splitting devices. This work aims to design a construct that is not negatively affected by the sunlight by decoupling of the OEC and the light excitation processes. The generation of reactive oxygen species (ROS) due to triplet formation by P680 is likely the reason PSII has an elaborate damage-repair cycle, and our construct isolates and aims to build an artificial oxygen-evolving complex (aOEC) that can be coupled to an artificial reaction center that is based on the reaction center in PSII.

1.8. “Isolating” the aOEC from $P680^{+}$

Extracting natural PSII from cyanobacteria or plants and using this in a solar fuel system is not possible due to PSII’s photodamage. This photodamage emanates from the reactive triplet formation of P680 [20], with P680 being responsible for the initial charge separation event in PSII. It would not be feasible to isolate and incorporate natural PSII into a solar to fuel system because in nature, the D1 protein is degraded every 30 minutes in the presence of sunlight. Therefore, the final goal of the Energy Frontier Research Center (EFRC) at ASU is to design a clean solar-to-fuel system that is based on nature. There are 5 subtasks that work on a critical part of the solar-fuel system, and ours focuses on rebuilding the OEC in a more stable environment so it can serve as an electron donor.

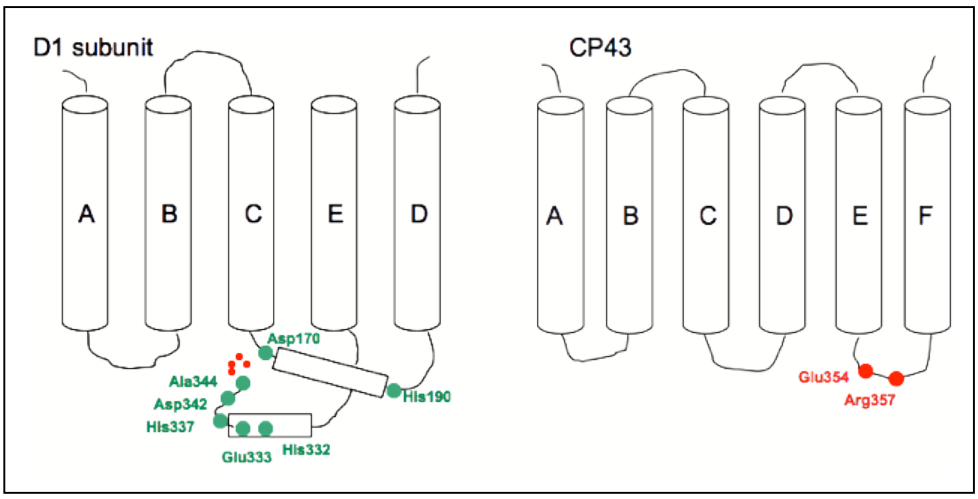

Figure 1.7. Schematics of both the D1 subunit and CP43 extrinsic subunit of PSII. Each cylinder represents a transmembrane helix. The Mn cluster ligands are shown in green (left) for the D1 subunit, and in red (right) for the CP43 subunit. These amino acids provide ligands to the Mn cluster and are used in our construct which aims to synthesize peptide sequences containing these critical amino acids. All of the critical amino acids are on the lumenal side of the membrane.

1.9. Deoxyribonucleic Acid – From Genetic Material to its Use in Nanoengineering – Why Use DNA as a Scaffold?

The structure of B-DNA was solved in 1954 by x-ray crystallography [23]. Over the past 60 years, not only do we know the structure and function of this macromolecule as a genetic tool, but we are now using it as a platform for nanoengineering a broad range of biological systems. The physiochemical stability and repeating helical structure of DNA offers a molecular framework for designing functional materials for drug delivery [24], nanomechanical devices [25], and synthetic catalysts [25]. DNA offers desirable characteristics like sequence specific base-pairing that allow for its use as stable frameworks in

nanotechnology [26,27]. The physiochemical stability of DNA makes it a desirable candidate for designing nanostructured materials as DNA is inherently nanoscalable. Double-stranded DNA (dsDNA) readily hybridizes in a highly reproducible process. Strands are separated at a 90°C peak temperature followed by a cooling step which facilitates the hydrogen bonding between the complementary bases adenine-thymine and guanine-cytosine, and allows the dsDNA to relax into its characteristic helical B-DNA structure. Structural building blocks comprised of DNA offer even more stability than protein-based scaffolds [28]. Because of the reproducibility of experiments and well-established protocols present in DNA technology, diverse 3-dimensional nanostructures have been previously designed [28,29], including a tetrahedron structure with 20 bp edges (20T tetrahedron) [29]. The pioneering work of Seeman and colleagues showed the first structure of a DNA crystal lattice formed by annealing [30]. Prior characterization of the 20T tetrahedron included a 8 Å resolution cryo-electron microscopy structure [31], providing the overall topography and verifying the expected assembly of the structure. However, the resolution limit of cryo-EM prevents the distinguishing between diastereomers and does not allow for the identification of individual bases. The fairly large cavity size of the 20T (inner diameter of 7 nm) tetrahedron structure enables small proteins and designed functional molecules to be enclosed in the center of the construct. DNA bases can be chemically modified to include many different linkers such as primary amines, thiols, dyes, polyethylene glycols, and carbon chains to serve as attachment sites for peptides, proteins, and nanoparticles. Prior published work

involving 3D DNA scaffolds includes the encapsulation of proteins, peptides, nanoparticles [32,33], dyes [34], and redox-active components [35]. Prior research utilizing these conjugation strategies include the encapsulation of cytochrome c in the center of a 3D DNA tetrahedron [36], the introduction of a two-dimensional scaffold of tetrahedra [30,37], and incorporation of the tetrahedron into antimony-doped tin oxide porous material [38]. A rationally designed three-dimensional network has many useful applications, especially having the ability to host macromolecules in a periodic array, similar to a crystal lattice [37,39]. Additionally, encapsulating redox-active proteins or molecules inside of the tetrahedron would allow for the use of the system for electron transfer reactions. Organizing functional proteins and biomolecules inside of 3D DNA-based nanostructures also offers the potential for catalytic enhancement, as the framework serves as a stable network for molecules in solution .

1.10. Structure Determination of Nucleic Acid Complexes

The PDB database (as of September 2012) reveals that of currently 65,950 structures solved by x-ray crystallography, only 1,346 (1.9%) are of nucleic acids, and 3,261 (4.6%) are of protein-nucleic acid complexes. Most of the published DNA structures solved by x-ray crystallography are DNA-protein complexes, short DNA sequences, and tetraplexes. However, to date, no x-ray crystallographic structures of three-dimensional DNA nanostructures have been reported.

2. HYPOTHESES AND DISCUSSION

2.1. DNA as a stable framework for engineering catalytic centers

DNA possesses many characteristics that allow for its use as a stable framework in this work. The physiochemical stability is known to be greater than that of proteins and peptides [28,40], and the specificity of base-pairing allows for reliable and reproducible experimental procedures. Additionally, DNA can be functionalized through many different chemical modifications; therefore, different peptide sequences or proteins can have multiple conjugation sites within the DNA tetrahedron. In this work, a three-dimensional DNA tetrahedron has been used as the stable framework for encapsulating peptides and cofactors. Four 63-base long oligonucleotides self-assemble to form the double-stranded tetrahedron, consisting of six 20 base pair edges, and four apexes which form the corners and are comprised of unpaired adenines. This nanostructure provides the structural framework to attach synthetic peptides that will coordinate cofactors. The ultimate final goal in the future of this project will be the assembly of the manganese cluster necessary for water oxidation inside the DNA nanocage.

2.2. Engineering a complete solar fuel production system based on water oxidation

A solar-based clean fuel system is necessary for human proliferation, as atmospheric CO_2 levels continue to rise, leading to significant climate change. The continuously rising atmospheric CO_2 levels have already left astronomical

footprints on our planet, as evidenced by the acidification of oceans and deterioration of carbonate coral reef systems [41], and the gradual shrinking of the arctic polar ice cap (National Snow and Ice Data Center: http://nsidc.org/arcticseaicenews/). Worse yet, atmospheric CO_2 emissions are predicted to rise to over 500 ppm (parts per million) between the years of 2050-2100 [41]. Rather than obtaining energy from hydrocarbons, solar energy can instead be harnessed using elaborate pigments that aid in capturing photons and transferring that energy to engineered catalytic systems based on what nature has already provided for us.

Water oxidation in PSII serves as the basis for our design, providing four electrons, four protons, and molecular oxygen as products. The goal of the EFRC is to build an artificial leaf mimicking nature, but making the system more efficient and robust. By understanding and mimicking the photosynthetic electron transport chain (that already exists in nature), a system has been designed by the EFRC that uses the *aOEC* as the Photosystem II mimic, the *arc* (artificial reaction center) as the reaction center mimic, the *fpc* (fuel production complex) as the hydrogenase mimic, and the *nte* (nanostructured, transparent wide band gap semiconductor electrode) as the transparent semi-conductor to absorb sunlight and aid the *arc* in promoting electron transfer. Protons produced from the oxidation of water by the aOEC are transferred through an ion-selective membrane to the proton reduction side of the system, where protons are reduced to hydrogen. See Figure 2.1 for an overview of the design.

aOEC design

The first design of the aOEC is comprised of three peptide sequences that are coupled in

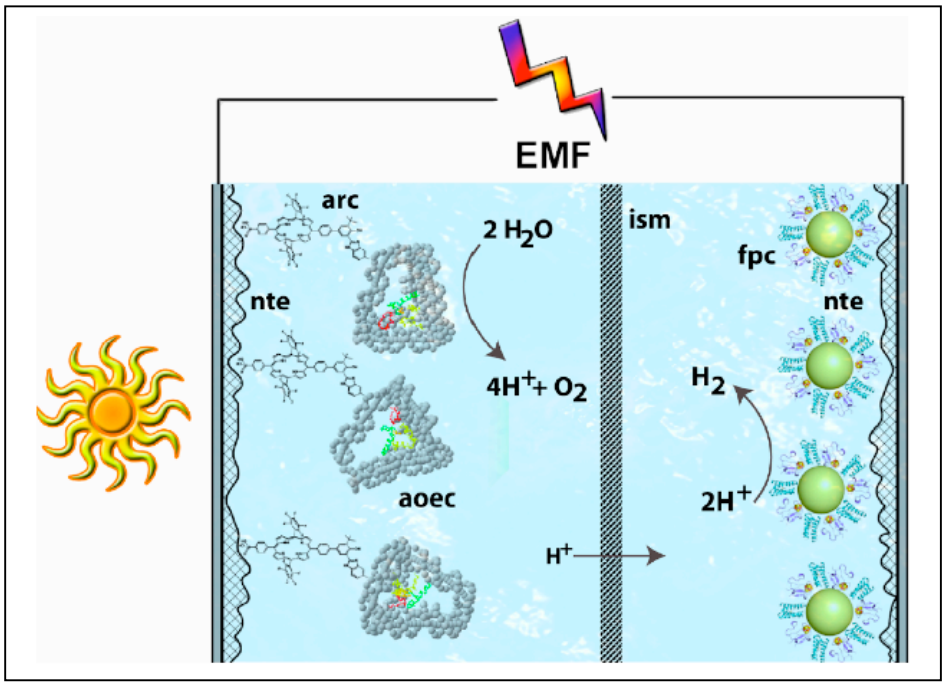

Figure 2.1. Schematic of the solar to fuel system based on water oxidation, the core of the Energy Frontier Research Center at ASU. The *aOEC* is the PSII mimic which will utilize the electrons generated by the *arc*. The *arc* is the reaction center mimic and consists of porphyrins which will absorb the light, and the *fpc* is the fuel production complex and serves as the hydrogenase mimic. Furthermore, the *nte* (nanostructured, transparent wide band gap semiconductor electrode) serves as the transparent semi-conductor to absorb sunlight and aid the *arc* in promoting electron transfer. The *ism*, or ion-selective membrane, allows the protons produced from water oxidation to be transferred to the proton reduction side of the system, where protons are reduced to hydrogen. Figure courtesy of the BISFuel team at ASU.

five different locations in the 20T tetrahedron. Specific linker chemistries such as click chemistry, maleimide-thiol linkages, and SMCC could be used to covalently attach the peptides to the tetrahedron. The peptide sequences are derived from the

natural peptide environment that coordinates the manganese cluster in PSII. The sequences are shown in Figure 2.2.

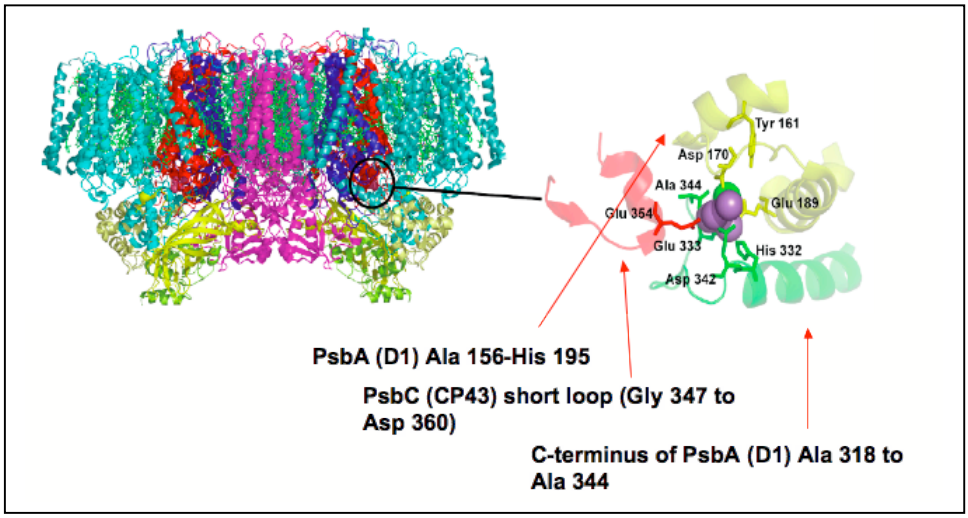

Figure 2.2. The peptide sequences implemented in this work, all providing critical ligation sites to the active site of PSII, the oxygen-evolving complex. These sequences will comprise the synthetic OEC described.

The green sequence is 34 aa long and consists of the C-terminal region of the D1 (PsbA) subunit of PSII (CT-D1) from Ala318-Ala344 and contains 4 ligation sites to the manganese cluster. The yellow sequence is also based on PsbA and is 40 aa long spanning from Ala156-His195 (156-195-D1) and is the lumenal loop between transmembrane helices d and e, which includes the redox-active TyrZ (Tyr161) and provides 3 ligation sites. Lastly the red sequence is 14 aa long and is designed based on the CP43 extrinsic protein subunit of PSII from Gly347-Asp360 (347-360-CP43), spanning the lumenal loop between helices e and f and provides one metal ligation site. Figure 1.7 shows the location of the peptide sequences in the PSII dimer. The final goal of this work is to build the 4MnCa

cluster with its surrounding ligands inside DNA nanocages. The synthetic peptides must have individual conjugation sites within the DNA tetrahedron and should be covalently attached to provide stability. The goal for the peptide conjugation is to covalently couple the peptides to the single-stranded DNA oligonucleotides first, and then anneal the sequences to form the DNA tetrahedron. Therefore, conjugation strategies must be employed that are specific and temperature tolerant due to the high temperature used for annealing (90°C).

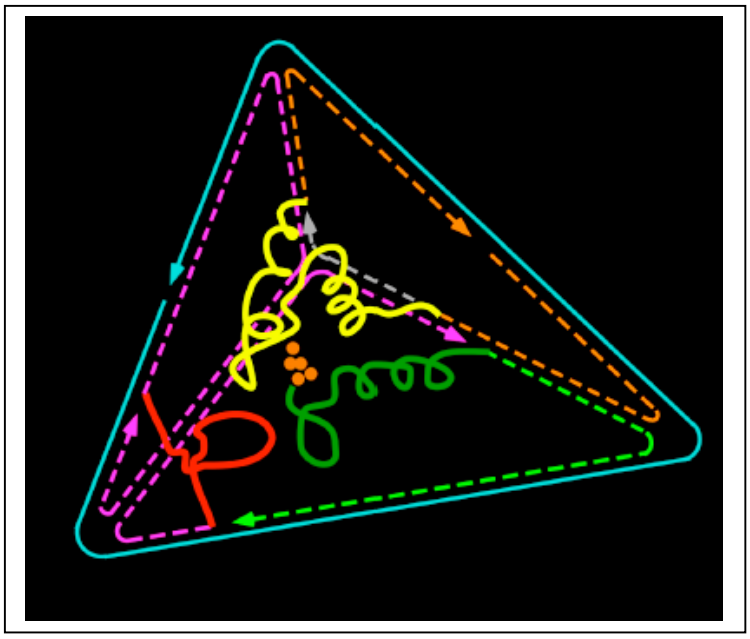

Figure 2.3. Schematic of the aOEC encapsulated inside of a 20 bp tetrahedron comprised of dsDNA. Each peptide sequence shown plays a critical role in water oxidation in nature and we hope to achieve the goal of water oxidation in this stable synthetic system. Figure courtesy of Chenxiang Lin.

3. THEORY OF ANALYTICAL METHODS

3.1. Dynamic Light Scattering (DLS)

3.1.1. Theory

Light has both magnetic and electric properties, and when it interacts with a particle, it results in an induced dipole that oscillates and emits radiation. The emitted radiation is called “scattering”. In solution, particles behave in a random manner, known as Brownian motion [42]. The Brownian motion of particles is affected by the particle size, the electric charge, shape, and abilities to bend or twist. When the light is scattered from the moving particles, it can be either constructive or destructive, depending on where the particles are in relation to one another. The interference between the scattered light changes as the particles are moving in solution, thereby causing fluctuations in the intensity of the scattered light [43]. Larger particles move slower in solution and therefore give slower fluctuations of scattered light, while smaller particles move faster and give faster fluctuations of scattered light [43]. There are three major types of light scattering – dynamic light scattering, static light scattering, and Raman scattering. Dynamic Light Scattering (DLS) is the technique used in this study so the focus will be on the theory of DLS. Upon detecting the fluctuations of the scattered light intensities, a diffusion constant can be derived using an autocorrelation function based on the measured intensities [44]. The software programs used in this study as designed by Dierks, et al. [45] typically use this diffusion constant to calculate

the hydrodynamic radius distribution in the measurements, based on the Stokes-Einstein equation

$$R_h = \frac{kT}{6\pi\eta D}$$

where R_h is the hydrodynamic radius, k is Boltzmann's constant, T is the temperature in K, η is the viscosity of the solution, and D is the diffusion constant. The measurements reveal a molecular weight of the sample based on the chosen parameters, such as the solvation sphere, density, and shape of the molecule, and also the viscosity of the solution. These properties are important as they significantly affect the observed molecular weight.

The experimental setup is shown below in Figure 3.1 and involves the use of a red laser (in this case 785 nm) that is aligned with the detector in a small volume of concentrated sample around 1-5 μL on a glass cover slide that is typically used for a hanging-drop vapor diffusion crystallization experiment. The sample is easily recoverable after measurements, which also makes DLS a desirable technique to use for pre-crystallization characterization. The DLS measurements give a distribution of hydrodynamic radii of the sample, along with the corresponding molecular weight. In order to obtain the molecular weight (MW) of the sample, the following equation is used.

$$MW = (R_h - r_w)^3 N_A \bullet (4\pi/3\nu)$$

Where N_A is Avogadro's number, r_w is the particle radius contribution, ν is the partial specific volume (the inverse of density), and R_h is the hydrodynamic radius [43,44].

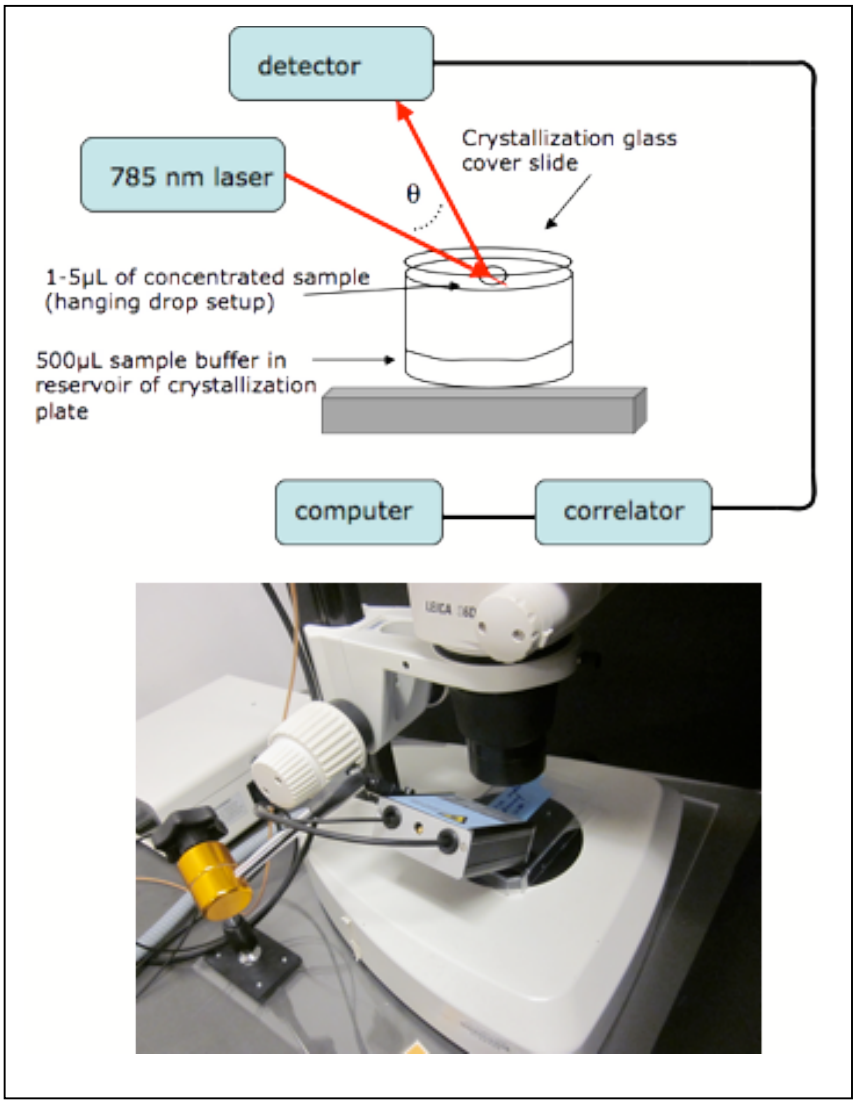

Figure 3.1. DLS setup using a small sample volume. A schematic of the setup is shown at the top, and the bottom shows an image of the instrument, a Molecular Dimensions SpectroSize 302. With this instrument, the angle between the laser pathway and scattered light, θ, can be varied.

3.1.2. Applications

DLS has many useful applications, one of them being very important to macromolecular crystallography. Considering that crystallization experiments require pure monodisperse samples, a technique is necessary to identify possible contaminants during sample preparation. DLS can detect the homogeneity of a protein sample and identify the aggregation state of a protein before any crystallization experiments are even attempted, allowing for earlier detection of problems arising in the sample preparation phase, especially aggregation, that would hinder the production of quality crystals. The aggregation state of the protein and any impurities can not only be identified in a sample [46], but also quantified through DLS. Over the last few years, improvements in DLS technology have lead to more sophisticated instruments [45] that have many more adjustable parameters for viscosity, molecular density, and shape factor - all of which drastically change the outcome of the size and molecular weight distribution determined by DLS. Some commercially available instruments like the instruments from Wyatt Technology do not have such manual input of parameters. The improved instruments are particularly important for novel rationally-designed macromolecules and in particular, DNA nanoarchitectures which need to be characterized and do not necessarily have the same density as a spherical protein. We use a novel design by Dr. Karsten Dierks, commercialized by Molecular Dimensions. Additionally, the pioneering work of K. Dierks et al involves the use of DLS to actually measure the size distribution of particles in the crystallization drop over time, indentifying the nucleation event, the

developing crystals, and the formation of precipitate. Given that aggregates were visualized shortly after setting up the crystallization experiment, the researchers were able to identify the nucleation threshold (once the aggregates stopped growing) and degree of supersaturation of a sample [45]. This DLS method can not only be used for pre-crystallization but also for monitoring the nucleation events in the crystallization in progress, determining the rate of crystal growth.

3.2. X-Ray Crystallography

3.2.1. Theory and Background

X-ray crystallography is a powerful technique to study a molecule's structure at atomic resolution. In solving the high resolution structure of macromolecules, we have improved our understanding of how biochemical pathways function, improved drug-ligand specificity, and revealed many other important mechanisms in biology [47]. Currently, 75,146 structures (biological macromolecular structures) solved by x-ray crystallography are deposited into the Protein Data Bank (www.rscb.org/pdb/statistics) as of October 2012. So far, in 2012 alone, 6800 x-ray structures were solved. Currently, only 9,680 NMR and 464 EM (electron microscopy) biological macromolecular structures in total have been solved.

3.2.2. Crystallization

X-ray crystallography involves the study of proteins and other macromolecules in their crystalline state. The first step of crystallography

involves devising a method and a set of conditions to crystallize the target macromolecule so it can be used in x-ray crystallography experiments. Without crystals, x-ray diffraction is limited to Small Angle X-Ray Scattering (SAXS) [48] and Wide Angle X-Ray Scattering (WAXS) studies [49] which so far do not allow for atomic resolution structures of large biomolecules to be determined. The crystallization step can often be the bottleneck in solving the crystal structure of a large biomolecule like a protein or DNA construct. Crystallization experiments often require many trials, and so sample preparation can also be a limiting factor. The molecule needs to be crystallized in a periodic array or lattice to allow for the x-rays to diffract on the lattice planes, according to Bragg's law

$$2d_{h,k,l} \sin \theta = n \lambda$$

where d is the distance along lattice planes h, k, l, θ is the reflecting angle, and n is an integer [47]. When the x-rays are diffracted from the crystal lattice, they produce a diffraction pattern from which a series of well-developed mathematical formulas are employed to obtain an electron density map, revealing each atomic position in a molecule.

Wave functions are used to describe the x-ray reflections, and a structure factor equation is the term used to describe a diffracted x-ray. The sum of the reflection hkl is called the structure factor, F_{hkl}. F_{hkl} is a term of the superimposed wave functions for every atom. Thus, every atom in a molecule contributes to every reflection in the diffraction pattern [50]. The sum is written as

$$F_{hkl} = f_A + f_B + ... + f_{A'} + f_{B'} + ...+ f_{F'}$$

in which the A', B', and F' values are the reflections. From the Fourier sum, the electron density is calculated, written as $\rho(x,y,z)$.

The equation that relates the electron density to the diffraction pattern is

$$\rho(x,y,z) = \frac{1}{V} \sum_{h} \sum_{k} \sum_{l} F_{hkl}\, e^{-2\pi i(hx+ky+lz)}$$

in which all of the reflections and phases are accounted for [50]. What many crystallographers commonly refer to is the "phase problem", in which the electron density cannot be directly obtained from a data set of diffraction patterns unless the atomic coordinates are already known. (See description of Molecular Replacement below). The "phase problem" in crystallography arises from the inability to distinguish between the periodic waves that comprise the reflections from the atoms. In a general description, structure factor amplitudes are obtained from the reflection intensities, and the structure factors are not directly obtainable from the reflections because the phase of each x-ray is unknown [50].

Therefore, there are several methods to overcome the phase problem – Molecular Replacement (MR), Multiwavelength Anomalous Diffraction (MAD), Single Isomorphous Replacement (SIR), and Multiple Isomorphous Replacement (MIR). In MR, the atomic coordinates from a homology model of a similar structure are used to solve the phases. In MAD, data sets are obtained at the heavy atom's absorption edge. Thus, multiple wavelengths of x-rays are scanned. Because of the different wavelengths of x-rays that the heavy atom derivatives absorb, Friedel's law does not hold and the reflection intensities are unequal.

Thus, in MAD, intensities of Friedel pairs are measured in the data set [50]. In SIR and MIR, heavy-atom derivatives are prepared. In SIR, one heavy atom is used, and in MIR, more than one is used. Selenomethionine derivatives, for example, are prepared during the protein expression phase. In other cases, the crystals are soaked in mercury, iodine, platinum, or gold which bind to specific sites in the protein crystal and are used to obtain the phases.

Crystallization is a phase separation process. In order to crystallize a molecule, the most widely used method involves using a precipitant. Through evaporation in vapor diffusion, the water molecules will slowly be removed from the solution so that the concentration of both the protein solution and the precipitant are increased in the crystallization drop [47]. As the water is removed, the protein solution becomes supersaturated and the molecules are forced out of solution. This could lead to amorphous precipitate as the molecules align together a certain way, ideally in a lattice. The crystallization process is depicted in a phase diagram in Figure 3.2. Crystallization is initiated through a nucleation event, or the formation of a "seed". The formation of the "seed" causes the radius to exceed the critical radius r_c. The supersaturation point where the nuclei reach r_c is marked by the nucleation zone. The protein is effectively forced out as a precipitate or as a crystal, which, if thermodynamically possible, may cause a phase change from the solution to the crystalline state. It is during this step that crystals form in the nucleation zone [47]. By formation of crystals, the soluble protein content continues to decrease, which causes the system to be moved into the metastable zone. In the metastable zone, pre-formed crystals can grow, but no new nucleation

events occur. This zone is therefore ideally suited for growth of large, well-ordered crystals from pre-formed seeds. The crystallization process continues until a kinetic equilibrium is reached between the soluble protein and the crystalline protein. The formation of showers of tiny crystals is a result of many nucleation events occurring at one time. Additionally, if the protein and precipitant concentration are too high, amorphous precipitate can form in the precipitation zone. Therefore, the method of obtaining diffraction-quality crystals is time-intensive and requires many trials with different precipitant, salt, and buffer systems to achieve the best crystals.

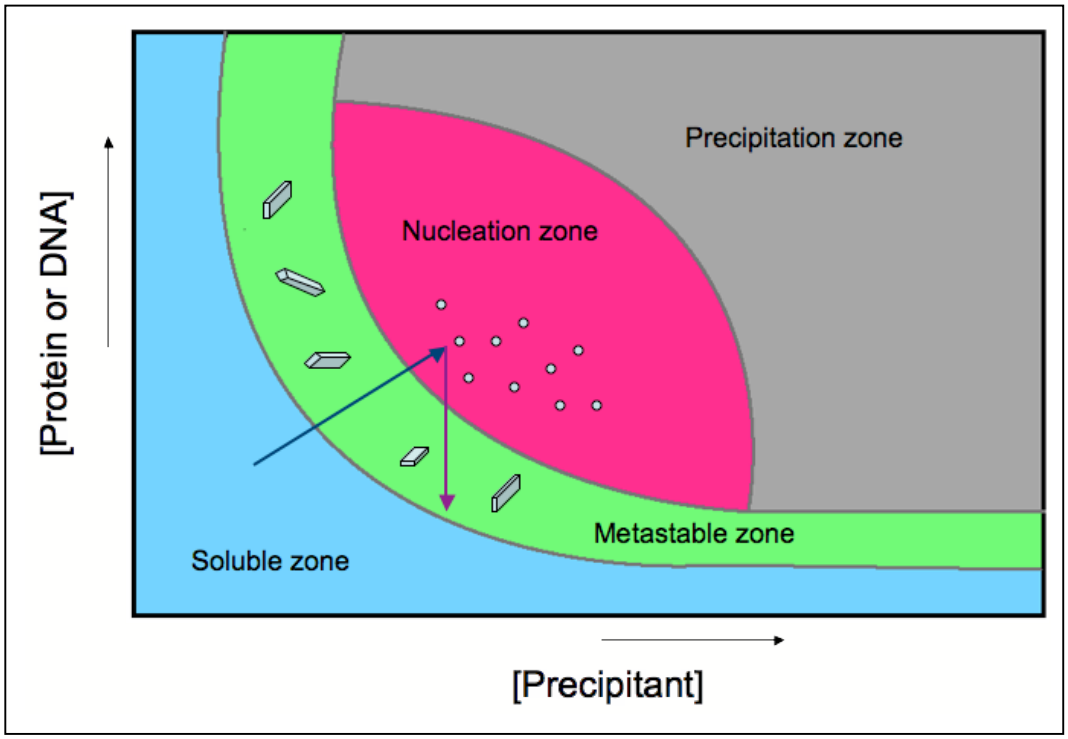

Figure 3.2. Crystallization phase diagram indicating the initial nucleation event (dark blue arrow) and subsequent decrease in soluble protein concentration by crystal growth, which brings the system into the metastable zone (purple arrow) where crystallization continues until the soluble protein and crystalline protein reach an equilibrium, as indicated by the purple arrow pointing to the interface of

the soluble and metastable zones. The x-axis indicates precipitant concentrations which could be salt, PEG, organic solvents, etc.

There are quite a few different techniques used for crystallization - vapor diffusion, batch crystallization, microdialysis, and free-interface diffusion. In this study, vapor diffusion (20T tetrahedron) and batch crystallization (PSII) were performed; therefore, they are described in detail in this text. Vapor diffusion methods require the mixing of protein and reservoir solution (screen solution containing a buffer, salt, and precipitant) in a small volume (1-5 μL) on a cover slide or in a sitting drop in a protein "well". The cover slide is sealed on top of a reservoir containing 500-1000 μL of the screen solution which contains a larger concentration of total molecules than the protein drop. Over time, the water in the protein drop evaporates, increasing the concentration of both protein and precipitant in the protein drop, and crystals form in the drop. As the volume of the reservoir is much larger than the volume in the drop, the "dilution" of the reservoir solution can be neglected and the concentration is thereby approximately constant. The concentration gradient between the drop and reservoir determines the final concentration factor of the protein drop.

In the batch crystallization method, the protein solution is mixed with the precipitant solution. This is usually done in a capillary tube, where the sample starts in the nucleation zone, and as the protein concentration decreases, the system moves to the metastable zone [51]. For this method the phase diagram

must be known. Furthermore, seeding with pre-formed crystals can be applied so that crystal growth directly occurs in the metastable zone.

The crystals are then incubated in cryoprotectants and frozen in liquid nitrogen before beginning x-ray diffraction experiments at either a home source or a synchrotron. Radiation damage has always been a prominent issue in macromolecular crystallography; therefore, the use of cryocooling of crystals began approximately 20 years ago after realization that there was significant radiation damage to the crystal in the presence of x-rays at room temperature [52]. X-ray damage causes the disruption of disulfide bonds, decarboxylation of asparates and glutamates, for example, and can also lead to reduced quality in diffraction patterns [52]. Additionally, the radiation damage problem is particularly significant when working with the current generation of synchrotron radiation sources compared to a home x-ray source such as a rotating anode, as the x-rays are more brilliant at the synchrotron [50], as shown in Figure 3.3 below.

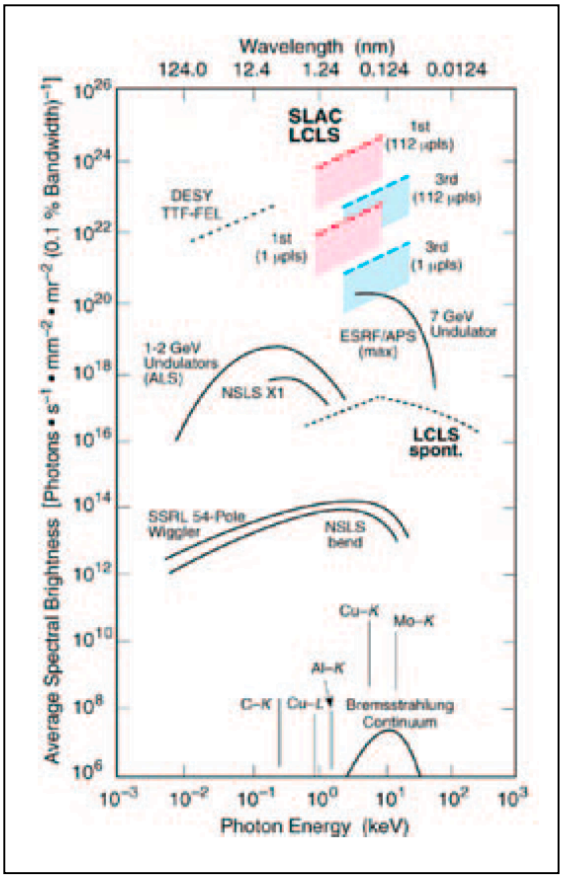

Figure 3.3. The photon energies and average spectral brightness of the x-rays produced by a rotating anode compared to x-rays produced by synchrotron radiation. The average spectral brilliance is much greater in the newest synchrotron sources, as seen at the top of the graph. Figure taken from reference [53].

Because it is necessary to rapidly freeze protein crystals, ice formation becomes an issue. Therefore, cryoprotectants were implemented to avoid ice formation during the freezing process. The most common method of freezing involves plunging the crystal into liquid nitrogen after incubating in cryoprotectant solutions. Other methods include using liquid propane and ethanol. The formation of ice damages the crystal and also the diffraction pattern [50]. Thus, cryoprotectants play a key role in solving a high-resolution structure of a

biological macromolecule. A schematic of a synchrotron is shown below in Figure 3.4, and images from a synchrotron facility are shown in Figure 3.5.

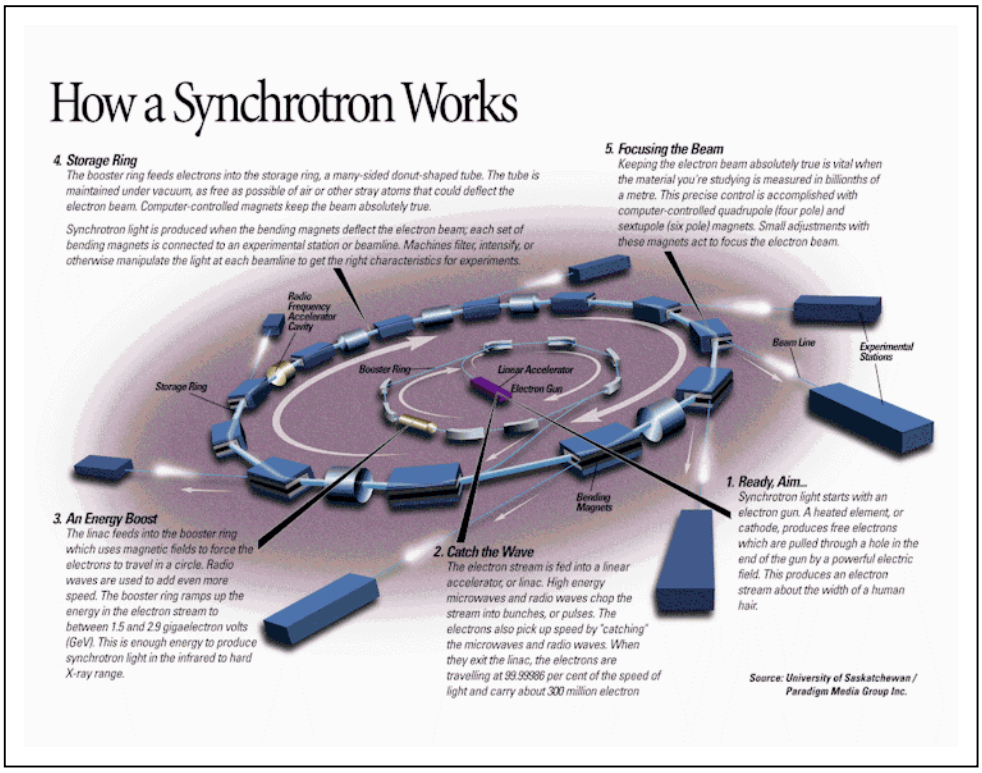

Figure 3.4. Schematic of a synchrotron. Synchrotron radiation is necessary for obtaining very high-energy photons ($\lambda = \sim 1$Å) focused into a small beam (sometimes as small as 5-10 μm in diameter [54] for microfocused beam experiments on tiny crystals) to obtain the highest-resolution structure possible. Image from http://geographyfieldwork.com/SynchrotronWorks.htm.

Figure 3.5. Images from Beamline ID-19 at the Structural Biology Center at the Advanced Photon Source (APS) at Argonne National Laboratory. Behind the door in the image on the left is the actual x-ray source. The image on the right shows the outside of one small section of the storage ring, depicting the large size of the synchrotron facility.

3.3. EPR

3.3.1. Background and Theory

Electron Paramagnetic Resonance (EPR) involves the study of paramagnetic species (compounds with unpaired electrons). Unlike Nuclear Magnetic Resonance, where the operating frequency is varied and the magnetic field is kept constant, EPR involves applying a varying magnetic field and keeping the operating frequency constant. Rather than studying nuclear transitions as in NMR, in EPR the electron transitions are studied. During EPR, molecules, ions, or atoms that contain paramagnetic species absorb radiation of microwave frequency. The unpaired electrons interact with the applied magnetic field, B, and are excited to the upper energy level. This interaction is referred to as the Zeeman effect. [55] See Figure 3.6. Because of the electron's excited state lifetime, the temperature during an EPR experiment is conducted in very low temperatures in the presence of liquid helium or nitrogen (between 4-77K). There are three main equations that explain the interaction of the magnetic field and the unpaired electrons, and they are shown below

(1) $\mu = -g\beta S$

(2) $E = \mu\beta$

(3) $\Delta E = h\nu$

where μ is the magnetic moment of the electron, β is the Bohr magneton, S is the total spin associated with the electron, h is Planck's constant, and ν is the frequency of the electromagnetic wave, E is the energy of a photon, and g is the spectroscopic splitting factor. From these equations and from applying the

constant frequency during the measurements (only the magnetic field is variable in EPR), one can calculate the *g* value based on

(4) $g = h\nu/\beta B_R$

where B_R defines the resonance condition. The resonance condition is defined as the point at which the applied magnetic field causes the energy of the transition to become resonant with the magnetic field. The *g* value is defined as the magnetic intensity at which the EPR absorption is at a maximum as the magnetic field is varied and ranges from less than 1 up to 18 [55]. The absorption curve is displayed as the first derivative in order to reveal more details of the spectra. See Figure 5 below for a schematic of EPR measurements. In this study, the frequency was 9 GHz (referred to as "X" band), and continuous wave (CW) EPR was used.

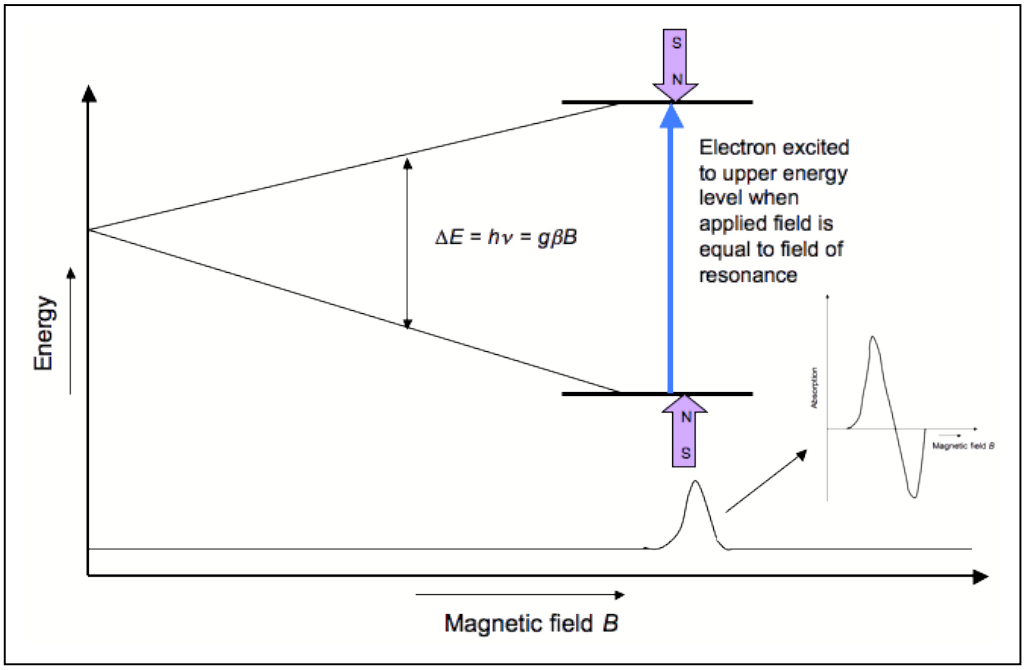

Figure 3.6. Diagram depicting the technique of EPR. Microwave irradiation of a sample causes an electron to become excited to a higher energy level, and this happens when the applied magnetic field, B, shown in the x-axis, is equal to the field of resonance. The energy increase is indicated by a peak. Although this figure depicts an energy diagram, the magnetic intensity at which the EPR absorption is at a maximum as the magnetic field is varied gives the *g* value, which would have absorption on the y-axis. EPR absorption spectra are shown in first derivative form, as shown in the inset.

EPR is a very valuable technique when studying proteins that contain metal centers. Metalloproteins are central to redox chemistry, which is essential to a cell's function. The redox state of proteins can be studied using this technique, which sheds light on their function. In this study, EPR is used to analyze the coordination of a transition metal, iron(III) by two axial ligands, identifying the characteristic spin-state change upon binding.

4. MATERIALS AND METHODS

4.1. PSII ISOLATION AND PURIFICATION

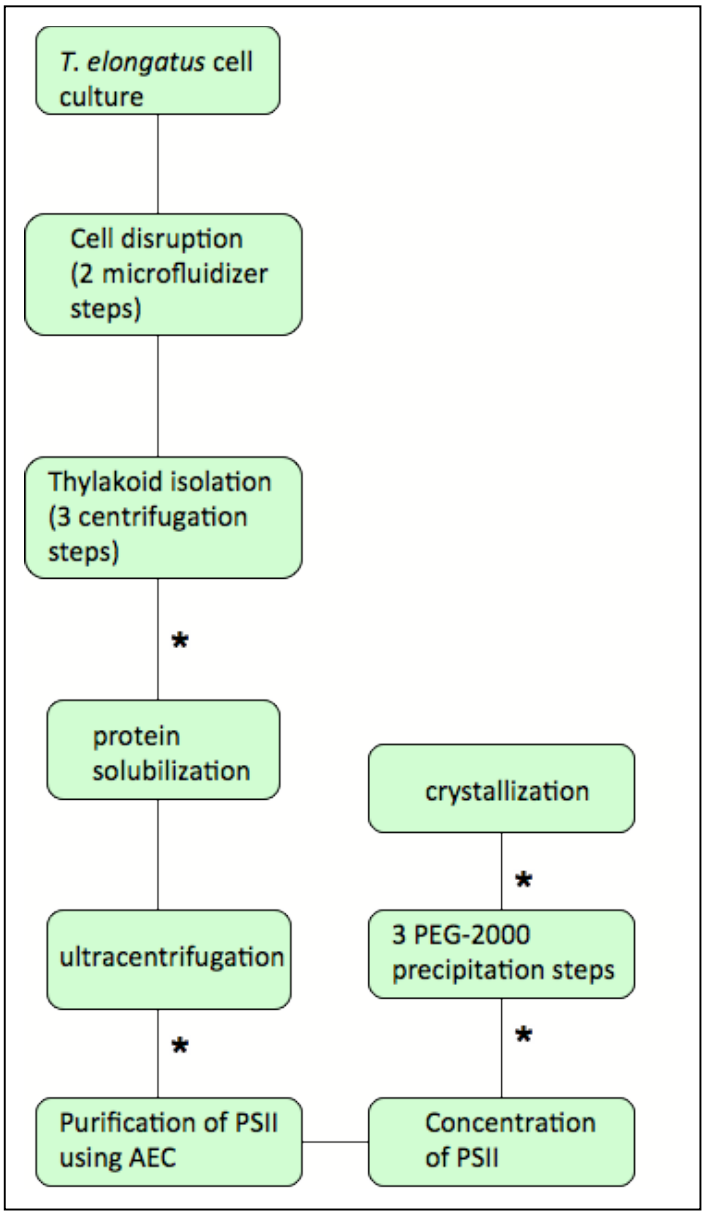

Figure 4.1. Flowchart briefly outlining each of the steps involved in PSII purification. The asterisks (*) indicate that a chlorophyll determination test is necessary before proceeding to the next step.

4.1.1. Cell culture

Photosystem II was isolated from the cyanobacterium *Thermosynechococcus elongatus* (*T. elongatus)* in a series of steps. This cyanobacterium is grown at a temperature of 56°C in a large-scale bioreactor (See Figure 4.2.) which holds approximately 120 L of cell culture. The reactor is operated in a quasi-continuous mode where ~50 L of cell culture are harvested 1-2 times per week in the logarithmic growth phase of the cells. ~20-30g of wet cell pellets are obtained from one harvest. The cells are frozen as a dense pellet at -80°C until use.

4.1.2. Cell disruption

Typically, between 20-25 g (enough for two FPLC runs) of frozen cells (stored at -80°C) were placed in a 220 mL centrifuge vessel and thawed in PREP1 buffer in a water bath with a temperature of 52°C and shaken from time to time until all cells were suspended. This thawing process is used because the intact cells are not stable between 4-8°C. The intact cells were centrifuged (Sorvall, Brea, CA, USA) in the 220 mL centrifuge vessel using a SLA-1500 rotor (Beckman Coulter, Brea, CA, USA) at 7,000 rpm at 24°C for 10 minutes. A paintbrush was used to remove the orange layer on top of the pellet containing *spirillum* cells which are a symbiont of the *T. elongatus*. The cells are disrupted using a microfluidizer (Microfluidics Model M-110L, Newton, MA, USA) where

Figure 4.2. The bioreactor used to grow the thermophilic cyanobacteria, *T. elongatus,* which holds approximately 120 L of cell culture. The cells are grown at 56°C.

cell rupture is achieved through high shear-forces at 9,000-13,000 psi. The microfluidizer was flushed with water and then PREP2 with the pressure reduction valve between 85-90 psi and a working pressure of 9,000 psi. Ice was placed on the microfluidizer coil prior to starting the flushing procedure in order to cool down the system. The sediment of cells from the centrifugation run was homogenized in 100 mL PREP2 + 1 mM PMSF before passing through a sieve and loading into the microfluidizer. The cells were passed through the microfluidizer twice at a pressure of 9,000 psi. Since the cells are very resilient to higher temperatures, the cell wall is very difficult to break and so two microfluidizing steps are necessary to break <90% of the cells. The microfluidizer was immediately flushed with 500 mL of water and then 100% isopropanol to prevent any clogging from cells left in the system. The centrifuge beaker containing the broken cells was filled with ice cold (4°C) PREP1 and centrifuged in a SLA-1500 rotor at 14,000 rpm for 10 minutes at 4°C to remove undesired cell contents.

4.1.3. Thylakoid preparation

The next few steps involve isolation of the thylakoids. The sediment was homogenized in 600 mL ice cold PREP1 and centrifuged in the SLA-1500 rotor at 11,000 rpm at 4°C for 10 minutes and this step was repeated once again. Then the pellets from the two centrifuge vessels were homogenized and combined. 200 mL ice cold PREP1 was added and the sample was centrifuged in the SLA-1500 rotor

at 11,000 rpm at 4°C for 10 minutes. The resulting pellet was homogenized in a small amount of PREP3 to achieve a concentration of at least 1 mM chlorophyll.

4.1.4. Chlorophyll determination

Four 1.5 mL reaction vessels were prepared with 635 mg 100% acetone and 199 μL water. Chlorophyll content was quantified by adding 1 μL of the sample in three of the four tubes, vortexing, and centrifuging in a microcentrifuge for 3 minutes at 12,000 rpm. In this step the chlorophyll is extracted, while the denatured protein and phycobilisomes are precipitated. The bluish colored pellet was visible along with a green supernatant. The supernatant was pipetted into a cuvette to measure the chlorophyll concentration. The chlorophyll concentration was determined by taking the molar extinction coefficient of ε = 76,780 [56] into account as

$$[(A_{664} - A_{700})/76{,}780] \times 1000 \text{ (in molar)}.$$

The chlorophyll concentration was adjusted to 0.75 mM with PREP3.

4.1.5. PSII solubilization

PSII was extracted in PREP3 containing 1% β-DDM and 1 mM PMSF. The solution volume was typically between 150-250 mL and was stirred at room temperature for 45 minutes in the dark. In this step, the solubilization of PSII from the thylakoid membranes takes place, where PSII is extracted in the form of a

protein-detergent micelle. The solution was divided into 8 centrifuge tubes for the ultracentrifugation step and placed into a 70Ti rotor (Beckman Coulter, Brea, CA, USA). The samples were centrifuged at 4°C for 1.5 hours at 50,800 rpm.

4.1.6. Purification of PSII by anion-exchange chromatography

The supernatant was collected from each tube (typical total volume was 200 mL) and purified by anion-exchange chromatography (AEC) using a FPLC (Akta, GE Healthcare, Piscataway, NJ, USA). The column (XK 26/70, GE Healthcare, Piscataway, NJ, USA) was packed with Toyo Pearl DEAE 650 S anion exchange material (Tosoh Bioscience). The column is 70 cm long, 26 mm inner diameter, and has a volume of 200 mL. The column was washed with 100% buffer A_{150} at a flow rate of 10 ml min^{-1} for 10 minutes, and then equilibrated with 10% buffer A_{150}, 90% buffer A_0 at a flow rate of 10 ml min^{-1} for 20 minutes. After the equilibration, the supernatant from the ultracentrifugation step was applied to the FPLC at a flow rate of 10 ml min^{-1}. The fractions containing the purified PSII were pooled and applied to 100kDa MWCO ultra-filtration units (Millipore, Billerica, MA, USA) to concentrate the protein. The PSII was centrifuged at 4000 rcf at 4°C.

4.1.7. PSII crystallization as the last purification step

Following the concentration step, the chlorophyll concentration was analyzed, with the target concentration of 0.75mM for the first precipitation step. Buffer C was added accordingly if the sample was too concentrated. PSII was

precipitated with a series of three PEG solutions for approximately one hour per precipitation, each with different amounts of Buffers D_0 and D_{20}. Buffer D_0 did not have any PEG-2000, while D_{20} had 20% (w/v) PEG-2000. For the first precipitation, the PSII was incubated for 1 hour with the first PEG-2000 concentration, typically between 4-6%. The amorphous precipitate was centrifuged at 4000 rcf at 4 °C for about 5 minutes and the pellet was redissolved in Buffer C to obtain the target chlorophyll concentration of 0.75 mM. This step was repeated twice more, but with decreasing PEG-2000 concentrations. The PEG-2000 concentrations typically used were between 4-6%, and the amount of precipitant needed was calculated based on the chlorophyll concentration. In the third precipitation step, small crystals normally appear. The small crystals can be dissolved to yield the protein solution for further crystallization experiments. The crystals were redissolved in Buffer C to yield a chlorophyll concentration of 4 mM for microbatch crystallization experiments.

4.1.8. PSII Crystallization

Microbatch crystallization experiments were set up with a starting PEG-2000 concentration range between 4-10%, with increments of 0.5%, made by diluting a 40% PEG-2000 stock solution with Buffer D_0. The microcapillary tubes used held 50 μL of sample. 15 μL of PSII was mixed with 15 μL of each PEG-2000 solution for each concentration of PEG. Following crystallization of PSII, the crystals were incubated for 5 minutes stepwise in cryoprotectants ranging

from 0-30% (0,8,15,24,30%) glycerol in Buffer C. The crystals were then frozen in liquid nitrogen.

BUFFERS AND SOLUTIONS USED FOR PSII PREPARATION

Tocopherol stock solution

0.5 M tocopherol in ethanol (10 mL)

PREP1 – 2L

20 mM MES pH 6.0
10 mM calcium chloride
10 mM magnesium chloride
10 μM tocopherol

PREP2 – 1L

20 mM MES pH 6.0
10 mM calcium chloride
10 mM magnesium chloride
10 μM tocopherol
500 mM mannitol

PREP3 – 1L

20 mM MES pH 6.0
10 mM calcium chloride
10 mM magnesium chloride
10 μM tocopherol
500 mM mannitol
20% (v/v) glycerol

PS2LC1 (A_0) – 4 L

20 mM MES pH 6.0
10 mM calcium chloride
10 mM magnesium chloride
10 μM tocopherol
20% (v/v) glycerol
0.02% β-DDM

PS2LC2 (A_{150}) – 2L

20 mM MES pH 6.0
10 mM calcium chloride
10 mM magnesium chloride
10 μM tocopherol
20% (v/v) glycerol
0.02% β-DDM
150 mM magnesium sulfate

PMSF stock (made on the day of the experiment)

0.5 M PMSF in DMSO – 10 mL

Buffer C

100 mM PIPES-NaOH pH 7.0
5 mM calcium chloride
0.03% (w/w) β-DDM

Buffer D_0

100 mM PIPES-NaOH pH 7.0
5 mM calcium chloride

Buffer D_{20}

100 mM PIPES-NaOH pH 7.0
5 mM calcium chloride
20% PEG-2000

4.2. TETRAHEDRA PREPARATION AND PURIFICATION

4.2.1. Oligonucleotide Design – 20T Tetrahedron

For the 20T tetrahedron, four single-stranded DNA oligonucleotides each 63 bases in length were purchased. (Integrated DNA Technologies, Coralville, IA) and purified using 8% denaturing-PAGE. See the figure below for a detailed dispay of the single-stranded oligonucleotides. The four strands were designed to hybridize to other regions of the complementary strands to form the double-stranded DNA (dsDNA) tetrahedron, consisting of six 20 base pair (bp) edges with four apexes containing a single adenine residue. This design was first described by Turberfield, et al. [29]

20T Tetrahedron

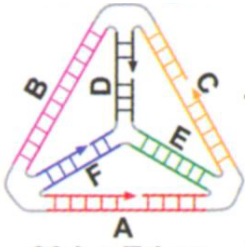

S1 – AGGCAGTTGAGACGAACATTCCTAAGTCTGAAATTTATCACCCGCCATAGTAGACGTATCACC

S2 – CTTGCTACACGATTCAGACTTAGGAATGTTCGACATGCGAGGGTCCAATACCGACGATTACAG

S3 – GGTGATAAAACGTGTAGCAAGCTGTAATCGACGGGAAGAGCATGCCCATCCACTACTATGGCG

S4 – CCTCGCATGACTCAACTGCCTGGTGATACGAGGATGGGCATGCTCTTCCCGACGGTATTGGAC

Figure 4.3. 20T tetrahedron sequences. Each color represents one edge of the tetrahedron, 20bp long. Figure taken from reference [29].

4.2.2. Oligonucleotide Design – 30T Tetrahedron

In order to assemble a 30T tetrahedron which would provide more space for molecules to be incorporated, four single-stranded DNA oligonucleotides, each 93 bases in length were ordered. (Integrated DNA Technologies, Coralville, IA) Figure 4.4 below shows the sequences. 10 extra bases were added to expand the size of the tetrahedron, with the goal of making a larger cage and maintaining the same G-C content in the structure as in the 20T tetrahedron. This designed tetrahedron structure should assemble into a larger tetrahedron consisting of six 30 bp edges with four apexes containing a single adenine residue. This structure was designed to encapsulate even larger proteins and macromolecules and possessed an internal cavity diameter of approximately 100Å.

30T Tetrahedron

S1 –
AGGCAGTTGAGACGAACATTCCTAAGTCTGAATTAGCATAACATTTATCACCCGCCATAGTAGCCATAAGTCCATATCAGCA
TTCGTATCACC
S2 –
CTTGCTACACGATTCAGACTTAGGAATGTTCGAATCGTATTGACATGCGAGGGTCCAATACCGTTACGATGCAAGCTTAGCT
ATCGATTACAG
S3 –
GGTGATAAAACGTGTAGCAAGCTGTAATCGATAGCTAAGCACGGGAAGAGCATGCCCATCCGGATTCAATAAGGACTTATGG
CTACTATGGCG
S4 –
CCTCGCATGACTCAACTGCCTGGTGATACGAATGCTGATAAGGATGGGCATGCTCTTCCCGCCTAAGTTATATGCATCGTAA
CGGTATTGGAC

Figure 4.4. Sequences for the 30T tetrahedron. Image taken from reference [29] and adapted for use with the new sequences. The 30T has 10 extra bp on each edge, providing a larger cavity for the encapsulation of other molecules.

4.2.3. Purification of Single-Stranded Oligonucleotides

In order to verify that the oligonucleotide strands were purified, the amount equal to 4 O.D. at 260 nm of each strand were loaded in each lane (a volume of 16 µL) of a 8% polyacrylamide gel, after mixing with 1X denaturing

tracking dye containing 0.1% bromophenol blue in 90% formamide in water and heating for 5 minutes at 90 ºC. The ssDNA was run for 2 hours at a current of 45 mA (per gel) at 37°C and the band containing the monomer of ssDNA was extracted from the gel. Further detail on the DNA extraction is described later in the Materials and Methods.

BUFFERS AND SOLUTIONS USED FOR DENATURING

POLYACRYLAMIDE GEL ELECTROPHORESIS (d-PAGE)

0% and 20% PAGE buffers were mixed accordingly to produce the desired concentration of polyacrylamide. In most cases, 8% polyacrylamide was used for the separation of single-stranded oligonucleotides. In order to achieve 8% PAGE, 42 mL of 0% PAGE was mixed with 28 mL of 20% PAGE, which made two gels. The gels were each 18 x 16 cm and 1.5 mm thick. To polymerize the gels, 525 μL of 10% ammonium persulfate (APS) stock solution was added, as well as 30 μL of N,N,N',N'-tetramethylethylenediamine (TEMED). The gel was poured and polymerized in 30 minutes. The gel electrophoresis was performed using a SE 600 Ruby (Amersham Biosciences, Piscataway, NJ, USA).

10X TBE (Tris borate EDTA) – 1000 mL
108 g Tris base (0.89 M)
55 g boric acid (0.89 M)
40 mL 0.5 M EDTA•Na_2 pH 8.0 (20 mM)
fill with diH_2O

1X TBE
100 mL 10X TBE
900 mL diH_2O

0% PAGE – 1000 mL
500 g urea (8.3 M)
100 mL 10X TBE
fill with diH_2O

20% PAGE – 1000 mL
500 g urea (8.3 M)
100 mL 10X TBE
500 mL 40% acrylamide stock (19:1 bis:acrylamide)
fill with diH_2O

Elution Buffer – 500 mL
19.27 g ammonium acetate (500 mM)
1.07 g magnesium acetate (10 mM)
2 mL 0.5 M EDTA pH 8.0 (2 mM)
fill with diH_2O

1X Denaturing Tracking Dye (Bromophenol Blue) – 100 mL
90 mL formamide (90%)
40 mg NaOH (10 mM)
37 mg EDTA•Na_2 (1 mM)
0.10 g bromophenol blue (0.1%)

1X Denaturing Tracking Dye (Xylene Cyanol FF) – 100 mL
90 mL formamide (90%)
40 mg NaOH (10 mM)
37 mg EDTA•Na_2 (1 mM)
0.10 g xylene cyanol FF (0.1%)

10% Ammonium Persulfate (APS) stock
1 g ammonium persulfate (10%)
fill up to 10 mL with diH_2O

The gel was removed from the electrophoresis chamber and stained with ethidium bromide (EtBr) for 5 minutes and then destained in water for 5 minutes. Visualization of the bands was done using a UV transilluminator (UVP, Upland, CA, USA) set at a wavelength of 302 nm to visualize EtBr. The bands were excised from the gel and placed into 0.45 μm filtered Spin-X columns (Corning, Lowell, MA) with 0.5 mL of gel elution buffer (500 mM ammonium acetate, 10 mM magnesium acetate, and 2 mM EDTA•Na_2 pH 8.0). The filter trapped the gel pieces from eluting along with the DNA. The DNA was extracted from the gel matrix at room temperature using a shaker for 1-2 hours before samples were centrifuged at 8000 rpm for 6 minutes. The top of the Spin-X column containing the gel pieces was discarded and 1 mL of 1-butanol was added to the liquid remaining in the bottom of the column, which resulted in the formation of an aqueous layer at the bottom (containing the DNA, and an organic layer containing ethidium bromide and gel tracking dyes). Samples were centrifuged at 2000 rpm for one minute, and the upper organic layer containing ethidium bromide and loading dyes was discarded. 1 mL of 100% ethanol was added to the remaining DNA and placed in the freezer at -20°C for 2 hours, to precipitate the DNA. Samples were centrifuged at 13,000 rpm for 30 minutes at 4°C. The ethanol served as an additional precipitation step to ensure purity of the DNA. A white pellet was obtained and after removing the ethanol supernatant; another precipitation followed, consisting of 70% ethanol. The samples were centrifuged at 13,000 rpm for 10 minutes at 4°C, the ethanol supernatant was discarded and the pellet was allowed to dry in a vacuum centrifuge for 2 hours with the

temperature set to 30°C. After drying the DNA, 50 uL of nanopure water was added to each of the tubes and the pellet was resuspended. The ssDNA was quantified by measuring the absorbance at 260 nm.

4.2.4. Annealing of 20T Tetrahedron

The 20T DNA tetrahedron structure was assembled by annealing of 4 ssDNA strands. Equimolar concentrations of each strand were added to 45 mL of annealing buffer [1X TAE-Mg^{2+} (40 mM Tris base, 20 mM acetic acid, 2 mM sodium EDTA, 12.5 mM magnesium acetate)] in 50 mL Falcon tubes (BD, Franklin Lakes, NJ) to give a final concentration of approximately 50 nM of DNA per tube. Different annealing conditions were initially tested, using concentrations between 50 nM and 5 μM. The tubes were placed in a 90°C water bath and cooled to room temperature in 2 hours. Following the annealing step at low concentrations of DNA, the samples were concentrated in increments of 4 minutes at 4000 rpm at 4°C using 30,000 MWCO ultrafiltration devices (Millipore, Billerica, MA).

4.2.5. Purification of 20T Tetrahedron

The purification method used for the 20T tetrahedron was size-exclusion chromatography (SEC) using a high pressure liquid chromatography (HPLC) instrument. SEC provided a route for selectively isolating the monomeric tetrahedron from the aggregation products and low molecular weight DNA fragments. The DNA was concentrated to approximately 0.5 mL before loading

the sample onto a Superdex SD200 16/60 prep-grade size-exclusion column with a 120 mL volume (GE Healthcare, Piscataway, NJ). The tetrahedron was purified in 120 mL of 1X TAE-Mg^{2+} buffer pH 8.0 at room temperature. The tetrahedron eluted after approximately 65 minutes at a flow rate of 1 mL min^{-1}.

BUFFERS FOR PURIFICATION OF TETRAHEDRON USING SIZE-EXCLUSION CHROMATOGRAPHY

50X TAE (Tris-acetate EDTA) – 1000 mL
242.2 g Tris base (2 M)
57.1 mL glacial acetic acid (1 M)
37.2 g EDTA•Na_2•$12H_2O$ (0.1 M)
fill with diH_2O

10X TAE-Mg^{2+} - 1000 mL
200 mL 50X TAE (0.4 M)
26.8 magnesium acetate tetrahydrate (125 mM)
fill with diH_2O

1X TAE-Mg^{2+} - 1000 mL
100 mL 10X TAE-Mg^{2+}
900 mL diH_2O

1X TAE-Mg^{2+} was the buffer used for all of the column runs for the 20T tetrahedron. The 50X and 10X were stock solutions.

4.2.6. Concentrating the Tetrahedron

The samples were collected and concentrated to at least 1.5 mg DNA ml^{-1} or 12 μM for crystallization experiments. The concentration step was performed using 30 000 molecular weight cut-off (MWCO) filters (Millipore, Billerica, MA, USA) which also removed traces of contaminants formed in the annealing process. Typical concentrations ranged from 1-4 mg ml^{-1} or 10-40 μM for crystallization and other further experiments.

4.3 CHARACTERIZATION OF 20T TETRAHEDRON

4.3.1. Quantification using UV-Vis

Following purification using SEC, the tetrahedron was concentrated to approximately 1-4 mg ml^{-1} or 10-40 μM. The concentration was verified by measuring the absorbance at 260 nm using a Quartz 10mm cuvette. A dilution factor of 100 was used in preparing the samples for UV/Vis analysis. 1μL of 20T was mixed with 99 μL of 1X TAE-Mg^{2+}. The concentration of dsDNA was given in the range of 6-40 μg ml^{-1} and this was converted to mg ml^{-1} with the 100X dilution factor included.

Using the calculated extinction coefficient for the 20T: ε = 2,109,396 M^{-1} cm^{-1} (calculated using the online calculator from Integrated DNA Technologies, Coralville, IA) and the equation below, the molar concentration was calculated.

$A_{260} = \varepsilon * [c] * d$ (pathlength was 1 cm)

4.3.2. Native Gel Electrophoresis

Prior to crystallization experiments, native gel electrophoresis was used to analyze the homogeneity of the 20T tetrahedron. Samples were prepared for native gel electrophoresis by mixing the 20T tetrahedron at a concentration of 2 mg ml^{-1} with 10X native tracking dye [0.2% (*w/v*) bromophenol blue, 0.2% (*w/v*) xylene cyanol, and 50% glycerol in 1X TAE-Mg^{2+}]. Samples were run on a 5% polyacrylamide native gel for approximately 3 hours at 20°C. Unpurified and purified tetrahedron samples were both analyzed using native gel electrophoresis. Samples were prepared for native gel electrophoresis by mixing 20T at a concentration of 2 mg ml^{-1} with 10X native tracking dye.

BUFFERS USED FOR NATIVE GEL ELECTROPHORESIS OF TETRAHEDRON

50X TAE (Tris-acetate EDTA) – 1000 mL
242.2 g Tris base (2 M)
57.1 mL glacial acetic acid (1 M)
37.2 g EDTA•Na_2•$12H_2O$ (0.1 M)
fill with diH_2O

10X TAE-Mg^{2+} - 1000 mL
200 mL 50X TAE (0.4 M)
26.8 magnesium acetate tetrahydrate (125 mM)
fill with diH_2O

10X Native Tracking Dye – 100 mL
0.2 g bromophenol blue (0.2%)
0.2 g xylene cyanol FF (0.2%)
50 mL glycerol (50%)
10 mL 10X TAE-Mg^{2+} (1X)
40 mL diH_2O

4.3.3. Dynamic Light Scattering (DLS)

Prior to crystallization experiments, Dynamic Light Scattering (DLS) (Molecular Dimensions, Apopka, FL, USA) was also used to analyze the homogeneity of the 20T tetrahedron. Samples were prepared for DLS by placing 3 μL of 20T (concentration 2 mg ml^{-1}) in the center of a siliconized cover slide, inverting and placing on the top of a well containing 0.9 mL of the buffer solution (1X TAE-Mg^{2+} pH 8.0). A 60 mW 785 nm laser was aligned with the detection channel to the drop so that they interact, and data was collected at 20 second intervals 10 times. Parameters for the DLS instrument were adjusted for the 20T to account for its lower density compared to that of proteins, and the resulting hydrodynamic radius distribution was observed. The parameters used were the following: concentration 1, refractive index 1, shape factor 1, hydration shell 0.2, exponent 2.3 (a calculation which would provide the molecular weight given the size of the molecule), and molecular density 0.4. The fraction of single tetrahedrons vs aggregates were calculated by integration of the peaks and divided by scattering intensity increases by r^6. The amount of aggregates was calculated by dividing the peak integration area by $radius^6$.

4.4 CRYSTALLIZATION OF 20T TETRAHEDRON

4.4.1. Crystallization of Tetrahedron

Immediately following annealing and purification, crystallization experiments were conducted. Initial crystallization experiments of the 20T tetrahedron resulted in small crystals in different conditions of the Sigma Nucleic Acids screen. Initial screening indicated crystallites in the following conditions:

- 50 mM cacodylate pH 6.0, 20 mM argininamide, 1 mM barium chloride, 2 mM spermidine hydrochloride, 30% PEG 400
- 50 mM HEPES pH 7.0, 1 mM cobalthexamine chloride, 35% PEG 400
- 50 mM cacodylate pH 6.5, 20 mM lithium chloride, 5 mM cobalt (II) chloride, 35% PEG 600
- 50 mM HEPES pH 7.0, 20 mM ammonium chloride, 5 mM $MgCl_2$, 35% PEG 600
- 1 mM cobalthexamine chloride, 2 mM putrescin hydrochloride, 35% PEG 600
- 50 mM cacodylate pH 6.0, 20 mM argininamide, 1 mM cadmium chloride, 30% PEG 1000

The tetrahedron was concentrated to a range of concentrations (1.5 mg ml^{-1} – 4 mg ml^{-1}). 2.5 mg ml^{-1} was the average concentration used for both the crystallization and DLS experiments. Sparse matrix screens (Sigma, St. Louis, MO) were initially used in determining the initial condition for the crystallization of the tetrahedron. Crystallization was further optimized to 29-34% PEG-1000, 10-25 mM L-argininamide, and 50 mM sodium cacodylate pH 6.0. A 24-well plate hanging drop setup was used (Qiagen, Valencia, CA) for all crystallization optimization experiments. 1 μL of tetrahedron was mixed with 1 μL of screen solution and placed on the cap. 0.9 mL of screen solution was placed in the reservoir. Crystals were grown in an incubator at 23°C and formed in

approximately 2-3 days. Optimization experiments included varying several parameters including varying the concentration of the tetrahedron (1-4 mg ml^{-1}), salt concentration, precipitant concentration, additives, pH variation, and temperature to achieve better quality crystals. In an attempt to grow larger tetrahedron crystals, heterogeneous nucleation experiments were performed using human hair as the nucleation agent.

All Screen Solution materials and concentrations are found in the Appendix Section. 20T fine screens 1 and 2 were designed based on prior results obtained from the Sigma Nucleic Acid Screen which gave the best "hits" for crystals with the screen solution named "H11". Screens 1 and 2 ranged from 23-38% PEG-1000 and 10-25mM L-argininamide. 20T Fine Screen 4 was used as a fine-tuned version of 20T Fine Screens 1-3, after determining that the best crystals grew in the 28-34% PEG-1000 range.

4.5 CRYSTAL FREEZING AND CRYOPROTECTANT MATERIALS

Freshly grown tetrahedron crystals were incubated in a range of cryoprotectants before being frozen in liquid nitrogen. Several tests were conducted in order to establish the best cryoprotectant for the 20T tetrahedron crystals and thus eliminate the formation of ice rings in the x-ray diffraction experiments. The Nextal Cryos Suite screen kit was used (Qiagen, Valencia, CA) for the initial cryo-cooling experiments. Crystals were first transferred into the various cryoprotectants which contained potential cryo-preservatives such as 2-methyl-1,3-propanediol (MPD), isopropanol, glycerol, sucrose, various PEGs, and different buffers including Tris, HEPES, PIPES, and MES. The idea behind the screen is to quickly replace the water by the cryo-protectant. However, in all of those cryoprotectant screen solutions, the tetrahedron crystals dissolved immediately. Therefore, an optimized cryoprotectant was developed that contained 40% PEG-1000, 60 mM sodium cacodylate pH 6.0, and 18 mM L-argininamide (a variant of the screen solution in which the crystals grew). Other cryoprotectant solutions included 50% PEG-2000, 60 mM sodium cacodylate pH 6.0, and 18 mM L-argininamide, in which the crystals remained stable as well. Crystals were incubated for approximately 10 -30 minutes before being flash-frozen in liquid nitrogen, in order to prevent the formation of ice rings in diffraction patterns.

4.6 X-RAY DATA COLLECTION

X-ray diffraction experiments were conducted at Lawrence Berkeley National Laboratory at the Advanced Light Source Beamline 4.2.2 and 8.2.2 and Argonne National Laboratory at the Advanced Photon Source at beamline ID-19. The wavelength of the x-ray beam was 1 Å, photon flux was 10^{12} photons sec $^{-1}$ and the beam size was 150 x 200 μm and exposure time was an average of 3 seconds. The crystals were rotated 200° and the oscillation range was 1° per image. The crystals were aligned in a cryostream of liquid nitrogen at a distance of 500 mm from the detector, and the detector size was 3072 x 3072 pixels.

4.7. IMPROVING CRYSTAL QUALITY AND ANALYSIS OF TETRAHEDRON STABILITY

4.7.1. Improving crystal quality by varying pH in screen solutions

In order to improve crystal quality and diffraction quality, tetrahedron crystals were successfully produced in screen solutions that contained different buffer systems such as Tris, Tris + cacodylate, and MES. Six screen solutions were developed with pH varying between 6.0-9.0, but containing the same salt (argininamide) and precipitant (PEG-1000) as the original screening conditions 20T Fine Screens 1-4. However, the PEG-1000 concentration was lowered in order to grow larger crystals at a slower rate.

4.7.2. Changing counterions in screen solutions and omitting argininamide

Another set of screens was designed in order to improve crystal diffraction quality and overall DNA stability. The screen solutions used additives of magnesium acetate in order to introduce more divalent cations into the crystallization conditions to stabilize the DNA phosphate backbone during the crystallization process. Different buffers were used as well, instead of only sodium cacodylate pH 6.0. Crystallization experiments were set up as previously described for original screening conditions.

4.7.3. Changing the magnesium counter-anions

Another set of screens was designed in order to test the influence of the concentrations of magnesium sulfate on the crystal formation and overall DNA stability. The screen solutions used counter-anions of magnesium (magnesium sulfate) in the crystallization conditions, as designed in Screens 8-10 except in some cases argininamide was omitted, and magnesium acetate was omitted and replaced with magnesium sulfate. Crystallization experiments were set up as previously described for original screening conditions. All crystallization screen charts are shown in the Appendix.

4.7.4. 20T tetrahedron crystal dehydration

20T crystals were dehydrated as another attempt to improve their diffraction quality. 20T tetrahedron crystals grown in 32% PEG-1000, 10mM argininamide, and 50mM sodium cacodylate pH 6.0 were transferred to the post

of a sitting drop tray with 10 µL of the screen solution containing 35% PEG-1000, 10mM argininamide, and 50mM sodium cacodylate pH 6.0., and 1000 µL of 50% PEG-1000, 10mM argininamide, and 50mM sodium cacodylate was added to the reservoir. The setup is described in Figure 5.11 in the Results section.

4.7.5. Analysis of tetrahedron stability following x-ray exposure

To test the stability of the DNA following exposure to synchrotron radiation, freshly dissolved 20T crystals used for data collection were immediately dissolved directly from the cryoloop in 1 µL 10X native tracking dye containing bromophenol blue and xylene cyanol before they were loaded onto an 5% native polyacrylamide gel. The samples were run for approximately two hours at 45 mA at 20° C.

4.8 NUCLEOTIDE-PEPTIDE CONJUGATION METHODS

4.8.1 PSII PEPTIDES – TOWARDS BUILDING THE aOEC

PSII peptide synthesis

According to the proposed design of the artificial oxygen-evolving complex (aOEC), three peptide sequences were developed based on the natural protein sequence of different subunits of the PSII reaction center that are responsible for coordinating the 4MnCa cluster. The first peptide sequence that has been synthesized is a modified mimic of the C terminus of D1 of PSII. The peptide is 35 aa in length. A 7-aa linker consisting of multiple glycines and tryptophans was included in the sequence to facilitate flexibility at the N-terminus (glycines) and to facilitate the use of fluorescence microscopy on conjugate crystals (tryptophan fluorescence). The peptide sequence is shown below and it was synthesized C to N terminus using a microwave peptide synthesizer (CEM, Matthews, NC) in the presence of β-maleimidipropionic acid and with 9-fluorenylmethyloxycarbonyl (F-moc) as the protecting group. The deprotection consisted of 20% piperidine in dimethylformamide (DMF), which provided the mild, basic conditions necessary for successful cleavage of the F-moc protecting group. Following cleavage from the resin (Wang resin), the peptide was N-terminal functionalized with a maleimide group for conjugation purposes. The functional groups (for the conjugation step) as well as the critical parts of the peptide are shown in Figure 5.21 in the results section. The highlighted portion of

the peptide sequence below indicates the linker designed to provide flexibility and tryptophan residues for use in tryptophan fluorescence experiments.

H_3N^+ - G W G G W G G A D I I N R A N L G M N E V M H E R N A H N F P L D L A - COO^-

The peptide was purified using reverse-phase chromatography in a gradient from 0-100% acetonitrile in water, and 0.1% trifluoroacetic acid (TFA) on a C4 reverse phase column (Waters, Milford, MA).

Secondary Structure Determination of PSII Peptide by Circular Dichroism

In order to test the presence of either alpha helices or beta sheets in the synthesized peptide, Circular Dichroism (CD) was used. To prepare samples for CD, 1 mg ml $^{-1}$ of peptide was placed in a Quartz cuvette and the samples were measured with a wavelength scan from 180 – 280 nm. No temperature gradient was used for these experiments – they were conducted at room temperature. Several wavelength scans were repeated in order to observe the secondary structure.

Manganese (II) titration of PSII Peptide

In a different set of tests, the peptide was titrated with concentrations of manganese (II) sulfate (manganese (II) chloride absorbs in the UV region and would interfere with measurements), even though binding would mainly be expected in the oxidation states of Mn(III) and Mn(IV). Different concentrations

ranging from 10-50 mM of manganese (II) sulfate were added to the peptide to detect if a conformational change in the peptide upon metal binding can be observed. Again, multiple wavelength scans from 180 – 280 nm were compiled and analyzed.

PSII peptide conjugation

The CT-D1 peptide was coupled to one specific site on the ssDNA (strand 4 of tetrahedron strand). One thymine was chemically modified with a thiol linker to facilitate coupling to the peptide via the N-terminal maleimide group. In the presence of *tris*(2-carboxyethyl)phosphine (TCEP), the ssDNA with the thiol linker was reduced to allow the free thiol to be exposed. The DNA sample was added to a spin column (Pierce, Rockford, IL, USA) in the presence of TCEP (to prevent the formation of disulfide bonds between thiolated DNA strands) and centrifuged for 2 minutes at 1500 x g with the 50-fold excess peptide (similar to the procedure described in [57]) solution in the bottom of the tube to allow the reaction to occur immediately between the peptide-DNA, reducing the possibility of accumulating ssDNA dimers. Figure 4.6 shows a schematic picture of the conjugation and is shown below. The sequences for the single peptide conjugation site construct of the tetrahedron are shown below.

S1 - AGGCAGTTGAGACGAACATTCCTAAGTCTGAAATTTATCACCCGCCATAGTAGACGTATCACC
S2 - CTTGCTACACGATTCAGACTTAGGAATGTTCGACATGCGAGGGTCCAATACCGACGATTACAG
S3 - GGTGATAAAACGTGTAGCAAGCTGTAATCGACGGGAAGAGCATGCCCATCCACTACTATGGCG
S4 – /5ThioMC6-D/ACCCTCGCATGACTCAACTGCCTGGTGATACGAGGATGGGCATGCTCTTCCCGACGGTATTGG

Figure 4.5. Sequences for the single conjugation site on the DNA strand 4 containing the thiolated thymine. Sequences and associated colors adapted from reference [29].

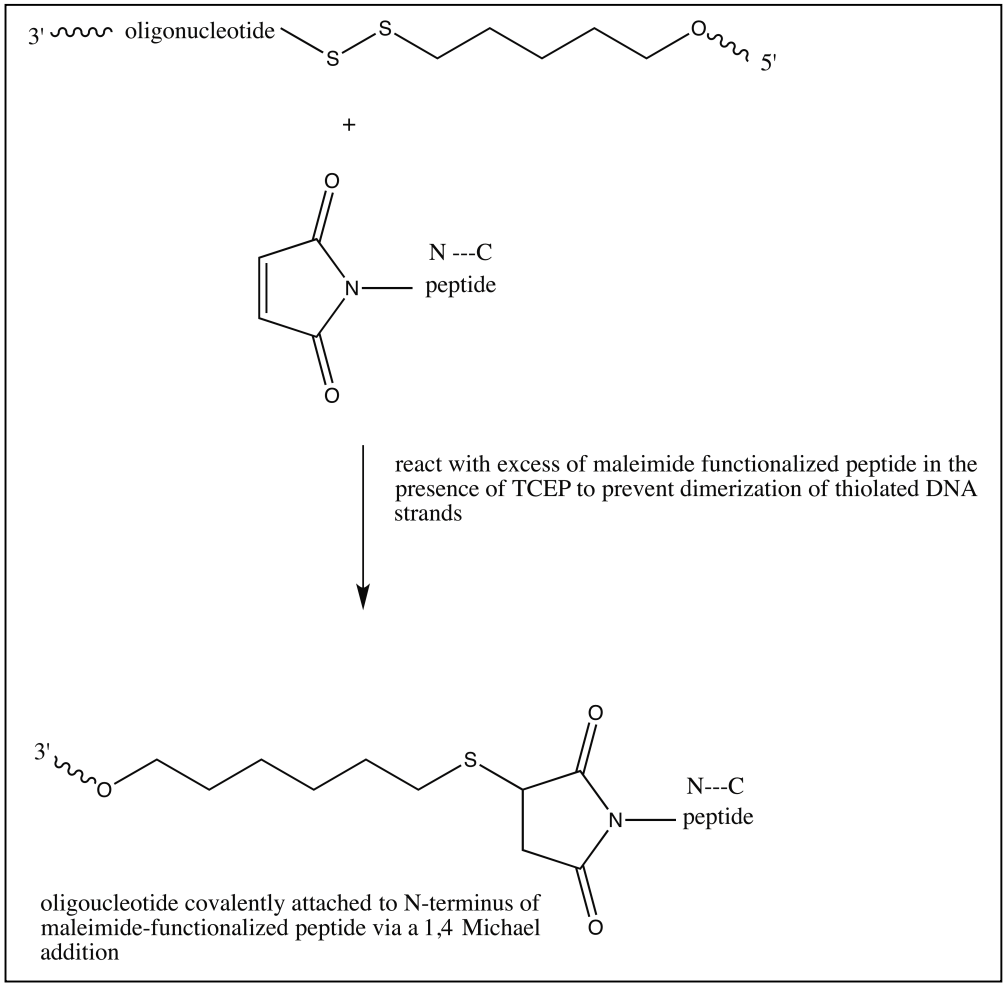

Figure 4.6. Conjuation scheme for the CT-D1 peptide and the 5'-thiol modified DNA strand 4.

PSII peptide annealing

Two strategies were employed regarding coupling of ssDNA to the peptide sequence. In one strategy, the peptide was coupled to the ssDNA first, in the scheme shown in Figure 4.6, and then the strands were annealed in equimolar concentrations at 90ºC to form the tetrahedron. In the second strategy, the tetrahedron with the thiol modified strand was annealed first, and the peptide was coupled later in the presence of the reducing agent in 1X TAE-Mg^{2+}. In both

cases, the construct was purified using size-exclusion chromatography, and the sample was concentrated to 2 mg ml^{-1} for further experiments.

4.8.2. INCORPORATION OF PEPTIDE-BOUND PORPHYRINS INSIDE OF THE TETRAHEDRON

Tetrahedron-Porphyrin-Binding Peptides Conjugation

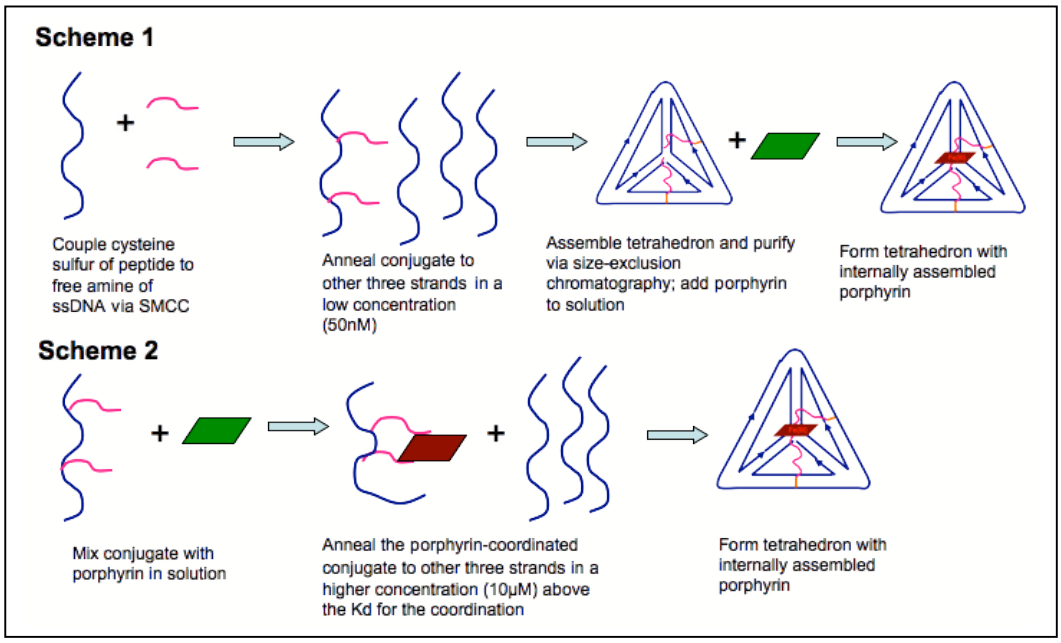

Figure 4.7. Schematic drawing of the experimental design for the porphyrin coordination inside of the tetrahedron - Scheme 1 indicates the method used to assemble the DNA framework first and later incorporate the porphyrin, while Scheme 2 requires porphyrin coupling first, and then annealing later.

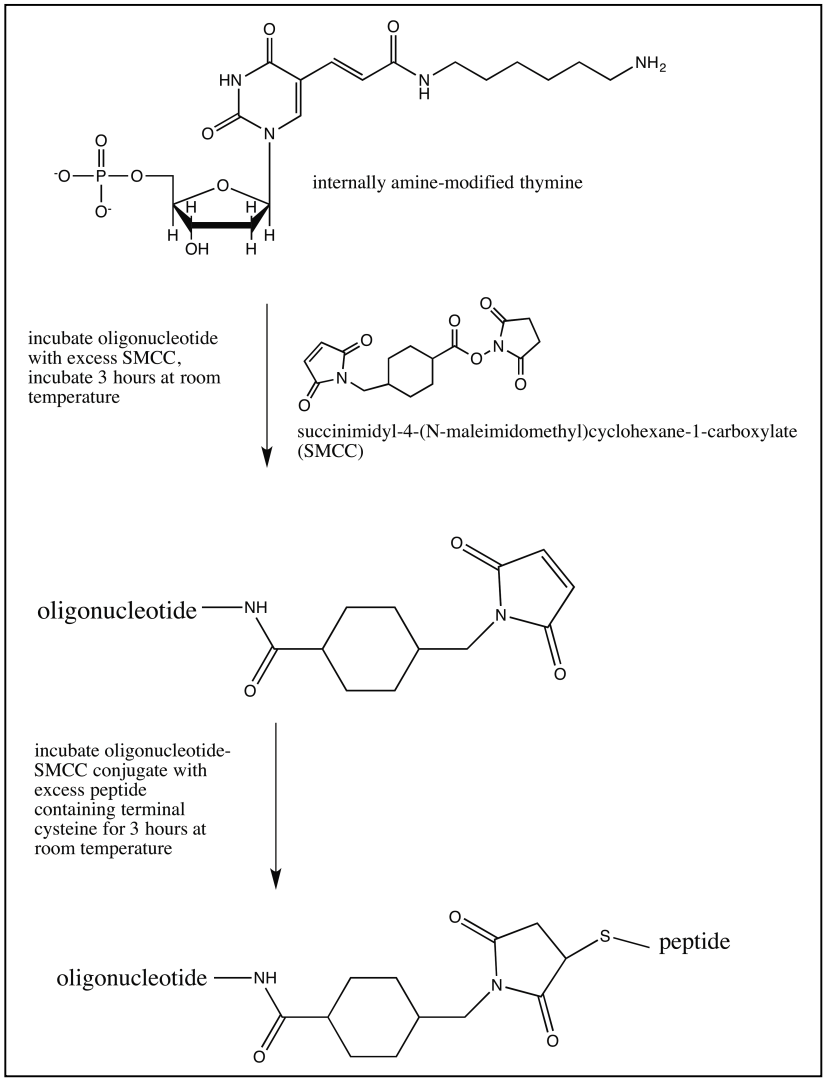

Figure 4.8. Schematic for oligonucleotide-peptide conjugation mediated by succinimidyl-4-(N-maleimidomethyl)cyclohexane-1-carboxylate (SMCC). Conjugation scheme adapted from reference [58]

As a proof of concept that metal-containing molecules can be incorporated inside of the tetrahedron, a water-soluble iron(III) porphyrin (Frontier Scientific, Logan, UT, USA) was introduced via two short peptide sequences containing terminal histidine residues that would axially coordinate to the iron(III) center of the porphyrin. The peptide sequence selected was *CAGAGSWH* (synthesis performed by Genscript, Piscataway, NJ, USA). The peptides were first

covalently attached to a ssDNA strand (strand 4) which had two amine-modified thymines that would be conjugated to the cysteine sulfur via heterobifunctional crosslinker SMCC. The nucleotide sites were selected based on how the tetrahedron folds to make sure that the peptides would reside inside the DNA tetrahedron. One of the conjugation sites had been successful for incorporating the CT-D1 peptide described earlier in this work. The other site was selected based on the folding of the tetrahedron (that site should be facing the inner cavity of the tetrahedron). There were two schemes for porphyrin incorporation shown in Figure 4.7 - one was to first assemble the tetrahedron with the peptides already attached and then add the porphyrin into the solution, and the other was to first couple the porphyrin to the ssDNA strand 4 with the peptides already covalently attached and then anneal all strands together.

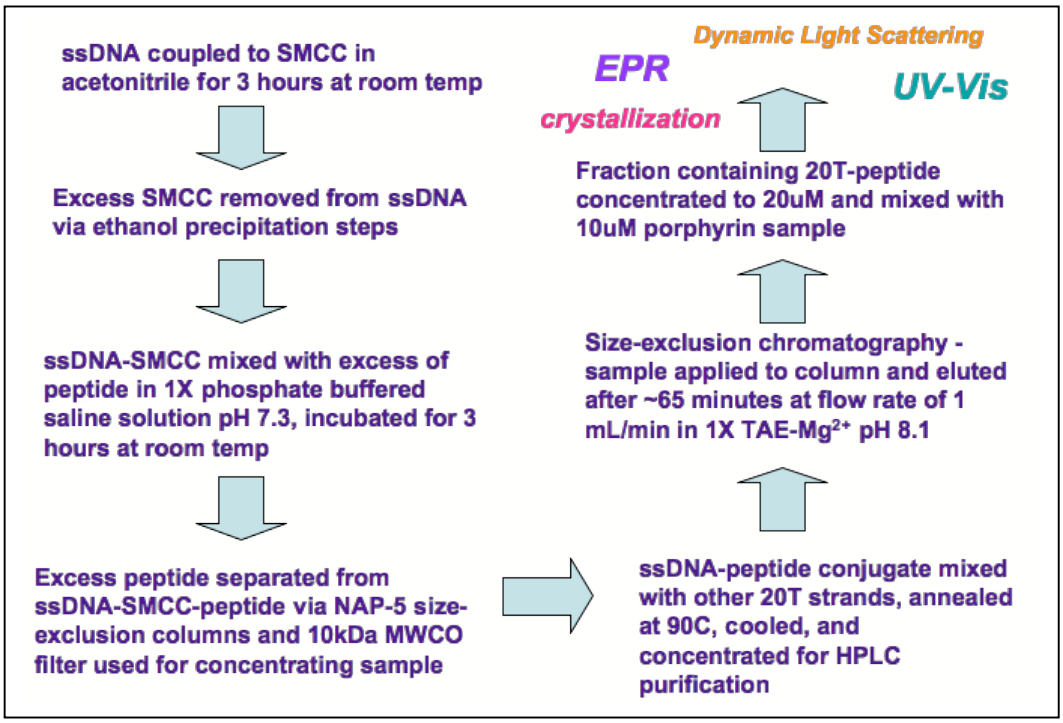

Figure 4.9. Flowchart describing experimental details of ssDNA-peptide conjugation leading to porphyrin assembly inside of the tetrahedron, using the procedure outlined in Figure 4.7 Scheme 1.

ssDNA-SMCC coupling

For DNA-SMCC conjugation, 84 μM of 20T amine-modified strand 4 was used. 50 μL of this sample was taken and added to 50 μL of 1X PBS (pH 7.3). The final concentration of ssDNA strand 4 was 42 μM. Next, a 2 mg ml^{-1} solution of (Succinimidyl-4-[N-maleimidomethyl]cyclohexane-1-carboxylate) (SMCC) (Sigma, St. Louis, MO) in acetonitrile was made by dissolving 2 mg of SMCC in 1 mL of acetonitrile at room temperature. The final concentration of SMCC was approximately 4 mM. It is necessary to have at least a 50-fold excess of SMCCfor the reaction to take place. 500 μL of 2 mg/ml (4 mM) SMCC was added to 100

μL of 42 μM S4 in 1X PBS pH 7.3. The reaction took place for 3 hours at room temperature. In order to precipitate the DNA and isolate it from the excess SMCC, 20μL of Elution Buffer (same buffer used for ssDNA extraction from gel matrix – see Buffer List), and 800 μL 100% ethanol were added to a 1.5 mL reaction vessel and placed in the -20°C freezer for at least 2 hours (overnight was preferable). The sample was centrifuged at 13,000 rpm for 30 min at 4°C. A white pellet was observed following centrifugation. The supernatant was discarded, and 800 μL 70% ethanol was added to the pellet. The sample was centrifuged at 13,000 rpm for 10 min at 4°C. The ethanol was discarded and the tube was placed in a vacuum centrifuge for 1.5 hours with the temperature set to 30°C. A dry pellet was obtained after the ethanol evaporated, and the pellet was stored at -20°C. The conjugate is stable at -20°C in pellet form for up to one month; however, the sample can also be immediately used for a reaction with short peptide sequences. In order to characterize the mass of the desired product, MALDI-TOF and denaturing-PAGE were used. Samples were prepared for MALDI-TOF by resuspending the pellet in 50 μL H_2O. A small amount of dried Dowex was added to the sample and mixed thoroughly to remove salt from the sample. The resin removes excess salts so they do not interfere with the measurements, which is a common problem when working with nucleic acids. [59]

ssDNA-SMCC-peptide conjugation and characterization by MALDI-TOF and PAGE

A stock solution of 4 mg/ml of peptide (3.2 mM) was prepared by weighing 4 mg of 8aa peptide *CAGAGSWH* (called "P8") and dissolving in 1 mL of 1X PBS pH 7.3. The concentration of the SMCC-conjugated 20T strand 4 was 84μM. A 50-fold excess was necessary for the coupling of peptide to ssDNA-SMCC. 250 μL of 20T S4 was mixed with 500 μL of peptide stock solution and incubated for at least 3 hours at RT. To remove excess peptide, NAP-5 gravity flow size-exclusion columns were used. (GE Healthcare, Piscataway, NJ) The NAP-5 column was equilibrated with 3 column volumes of 1X PBS pH 7.3 for a total volume of 9 mL. Following column equilibration, the sample containing the DNA-peptide conjugate was applied to the column and eluted with 3 column volumes of buffer. The fractions were collected, and the sample was applied to a 10 000 MWCO filter (Millipore, Billerica, MA, USA) and concentrated. A concentration of 80 μM and volume of approximately 200 μL was achieved following concentration. The sample was characterized using MALDI-TOF, which showed a clear peak representing the expected mass of the conjugate at 21.2 kDa. Samples for MALDI-TOF were prepared by mixing the purified conjugate with matrix (saturated 3-hydroxypiccolinic acid solution) in a 1:1 ratio, and then adding solid Dowex resin to the sample to remove salt. 1 μL spots were placed on the MALDI-TOF (Matrix-Assisted Laser Desorption/Ionization-Time of Flight) sample plate and dried before analysis. Additionally, the conjugate was characterized using 10% denaturing-PAGE gel shift assays, which showed an

approximate shift of 1.5 kDa between the purified 20T S4 and purified 20T S4-peptide conjugate at the same concentration. (See Figure 5.30 in the Results.) For the denaturing gel shift assay, 10 μL of sample (both the S4 and conjugated S4) was mixed with 10 μL 2X denaturing tracking dye containing bromophenol blue, vortexed for 10 seconds, centriguged at 2000 rpm for 30 seconds, and then heated for 5 minutes at 90°C. Then the samples were applied to the 10% denaturing-PAGE gel and ran for 1 hour 20 minutes at 35°C. The gels were stained using ethidium bromide, destained, and visualized on a UVP Biospectrum Imaging System at 302 nm.

Annealing of Strand 4-P8 Conjugate with 20T S1-S3

80 μM of purified S4 conjugate was mixed with the other strands 1-3 of the tetrahedron in equimolar ratios. The samples were annealed in 50 nM concentrations in 1X TAE-Mg^{2+} concentrated to approximately 1 mL, and subsequently purified using SEC. The samples were applied to a Superdex 200 prep-grade column (GE Healthcare, Piscataway, NJ) and a flow rate of 1 ml min^{-1} was used. The chromatogram verifies that the 20T-peptide complex (20TP8) eluted at approximately the same time as the 20T. Wavelengths of 260 and 280 nm were used to measure both DNA and peptide.

Peptide-porphyrin sample preparation : UV-Vis and EPR

As a preliminary test, just the P8 peptide and Fe(III)-TPPS4 porphyrin were mixed in varying concentrations in order to verify the spectroscopic properties of

free porphyrin and histidine-coordinated porphyrin. To do this, a 10 mM stock solution of peptide and 2 mM stock solution of porphyrin were made. The following dilutions were prepared:

0.5 mM porphyrin
0.5 mM porphyrin : 0.5 mM peptide
0.5 mM porphyrin : 1 mM peptide
0.5 mM porphyrin : 2.5 mM peptide
0.5 mM porphyrin : 5 mM peptide

These samples were prepared for EPR and UV-Vis experiments in 1X TAE· or -Mg^{2+} with 20% glycerol. A second set of samples with the same dilutions was also prepared in the same buffer but without EDTA. EPR tubes (Wilmad LabGlass, Vineland, NJ) were loaded with 180 μL of each dilution and frozen in liquid nitrogen. A small amount of sample was used for UV-Vis analysis and a wavelength scan was performed from 250-800 nm. Continuous wave X-band EPR analysis was performed at a temperature of 6 K with a frequency of 9.340 GHz and 2 mW power using a Continuous Wave (CW) X band (9-10GHz) Bruker ESP300E spectrometer with an Oxford ESR 900 cryostat (Bruker, Billerica, MA, USA).

20T-peptide-porphyrin sample preparation : UV-Vis and EPR

Following purification of the 20T-peptide construct via size-exclusion chromatography, the sample was concentrated to approximately 10 μM. A 1 mM stock solution of the porphyrin was made. The buffer condition was 1X TAE-Mg^{2+} with 20% glycerol. Another set of EPR samples were prepared – (1) 5 μM porphyrin, (2) 5 μM porphyrin + 10 μM peptide (as a control), and (3) 5 μM

porphyrin + 10 μM 20T-peptide, 100 μL total volume per sample. Continuous wave X-band EPR analysis was performed using a temperature of 6K, 9.340 GHz frequency, and 2 mW power. Samples were also analyzed using UV-Vis and were prepared by adding 20 μL of the samples to a Quartz 10mm cuvette and performing a wavelength scan from 250-800 nm.

Native gel electrophoresis

The 20T-peptide-porphyrin complex was analyzed for the presence of monomer and aggregates using the same dilutions as mentioned in the EPR experiments. 18 μL of 10 μM 20T-peptide was mixed with 2 μL of 10X native tracking dye containing bromophenol blue and xylene cyanol and loaded onto a 5% native polyacrylamide gel. 18 μL of 10 μM 20T-peptide : 5 μM porphyrin dilution was mixed with 2 μL of native tracking dye and also loaded onto the gel. Samples were run at 90 mA at 20 °C for approximately 4 hours. The gel was stained in ethidium bromide, destained in water, and illuminated at 302 nm and visualized using a camera (UVP, Upland, CA).

Dynamic Light Scattering Measurements

As another test to analyze if aggregates formed through the addition of porphyrin, DLS samples were prepared. A freshly prepared 60 μL aliquot of 10 μM 20T-peptide sample was placed in a cuvette and transferred into the light scattering instrument (Wyatt, Santa Barbara, CA, USA) and 20 measurements

were taken in increments of 10 seconds each. The software analyzed each measurement and a distribution plot was generated. The same procedure was repeated for the 20T-peptide-porphyrin sample. The same concentration was used (10 μM) but mixed with porphyrin to achieve a final concentration of 10 μM 20T-peptide and 5 μM porphyrin. Following DLS analysis, peak integration was performed using the accompanying software from Wyatt. A spherical protein was assumed as the overall shape for the calculations, since no 3D DNA parameter or manual entry of a parameter set was allowed.

Crystallization of 20T-Peptide and 20T-Peptide-Porphyrin

Solving the structure of the empty 20T tetrahedron has proven challenging, and it may be possible that internally assembling peptides and porphyrins stabilize the tetrahedron and improve the diffraction quality of the crystals. Therefore, crystallization trials for the 20T tetrahedron-porphyrin were set up. First, the 20T-peptide was used and the concentration was 20 μM or approximately 2 mg ml^{-1}. For the 20T-peptide-porphyrin, the final concentrations were 10 μM 20T-peptide and 5 μM porphyrin. The experiments were set up in trays (Qiagen, Valencia, CA) using the vapor diffusion method, using a hanging drop set up due to the limited amount of the 20T-peptide and the 20T-peptide-porphyrin samples. For the hanging drop setup, 1 μL of 20TP8 sample was mixed with 1 μL of the screen solution and placed in the center of a glass cover slide. This cover slide was placed over the well containing 500 μL of the screen solution in the reservoir. This same procedure was repeated when testing the

20TP8P samples. A modified 20T Fine Screen 4 was designed, with only 5 conditions selected from the 24-condition screen. Experiments were set up for both the 20T-peptide and the 20T-peptide-porphyrin in order to test whether the porphyrin hinders or aids in the crystallization process. The conditions used were the following:

20T Fine Screen 4, condition 3
31% PEG-1000
10 mM argininamide
50 mM sodium cacodylate pH 6.0

condition 9
31% PEG-1000
15 mM argnininamide
50 mM sodium cacodylate pH 6.0

condition 16
32% PEG-1000
20 mM argnininamide
50 mM sodium cacodylate pH 6.0

condition 20
30% PEG-1000
25 mM argnininamide
50 mM sodium cacodylate pH 6.0

condition 24
34% PEG-1000
25 mM argininamide
50 mM sodium cacodylate pH 6.0

5. RESULTS AND DISCUSSION

5.1. PSII RESULTS

5.1.1. Purification of PSII using AEC

Purification of PSII involved the use of AEC. The PSII dimer peak typically elutes around 100 minutes into the purification run, at a flow rate of 10 ml min^{-1}. The peak is shown in Figure 5.1 below.

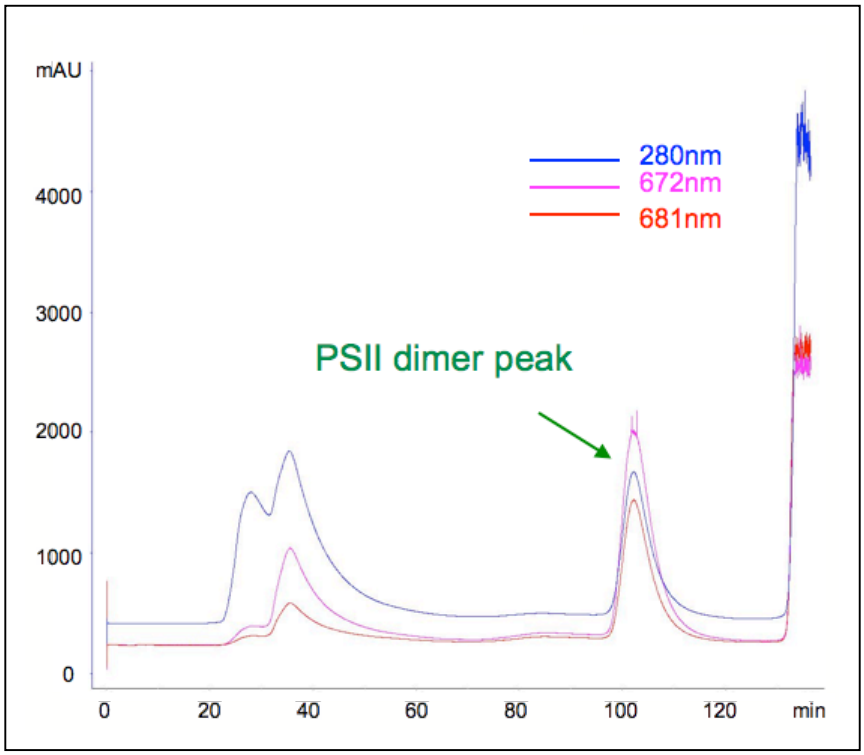

Figure 5.1. Purification of PSII using AEC. The PSII dimer peak elutes around 100 minutes. The peaks around 20-40 minutes are of PSI and other proteins isolated from PSII. Chromatogram modified from the original data obtained by Chris Kupitz.

The PSII crystals typically grew in 1-2 days and had a very solid green appearance, usually with a diamond or square shape. The best crystallization conditions for PSII were usually in the 2-4% PEG-2000 range, as shown in the crystal gallery in Figure 5.2. Many trials of crystallization conditions were attempted, including decreasing and increasing the PEG-2000 concentrations; however, the highest quality crystals still grew in 2-4% PEG-2000. Increasing the PEG-2000 concentration resulted in smaller crystals, as shown in Figure 5.2b.

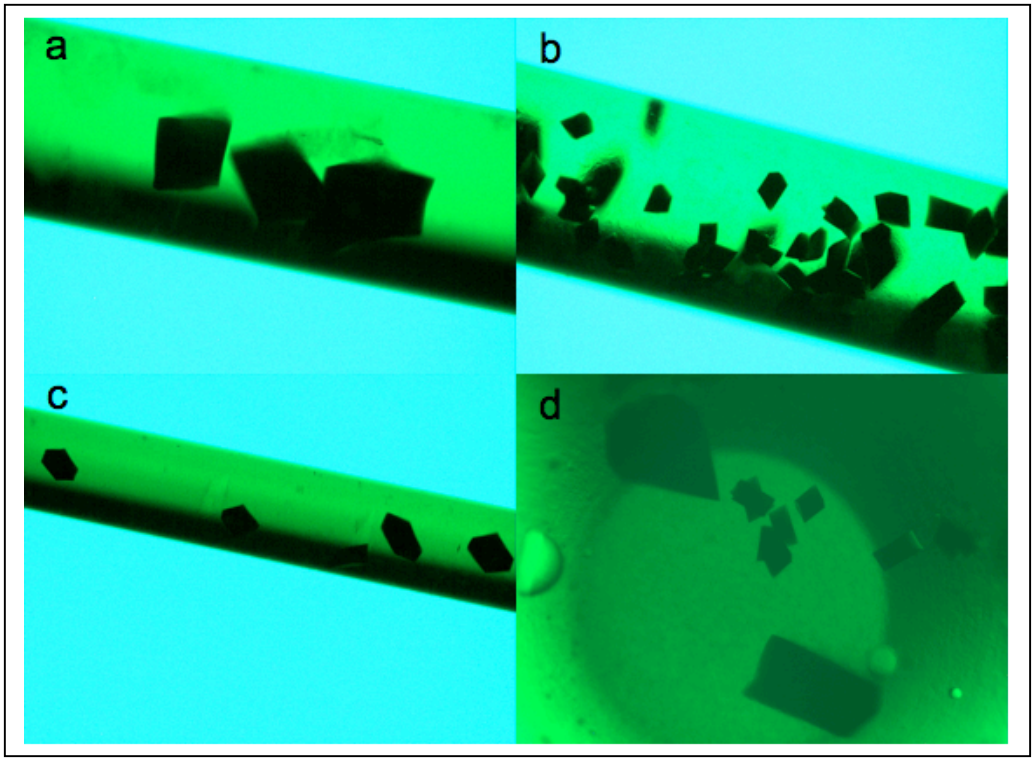

Figure 5.2. PSII crystal gallery. Figure a shows crystals grown in 4% PEG-2000 in Buffer C. B shows crystals grown in 4.5% PEG-2000 that are visibly smaller than those shown in a. C shows hexagonal shaped crystals grown in 2% PEG-2000. D shows crystals grown in 2% PEG-2000 in a batch crystallization experiment under paraffin oil. These crystals all formed in approximately 1-2 days.

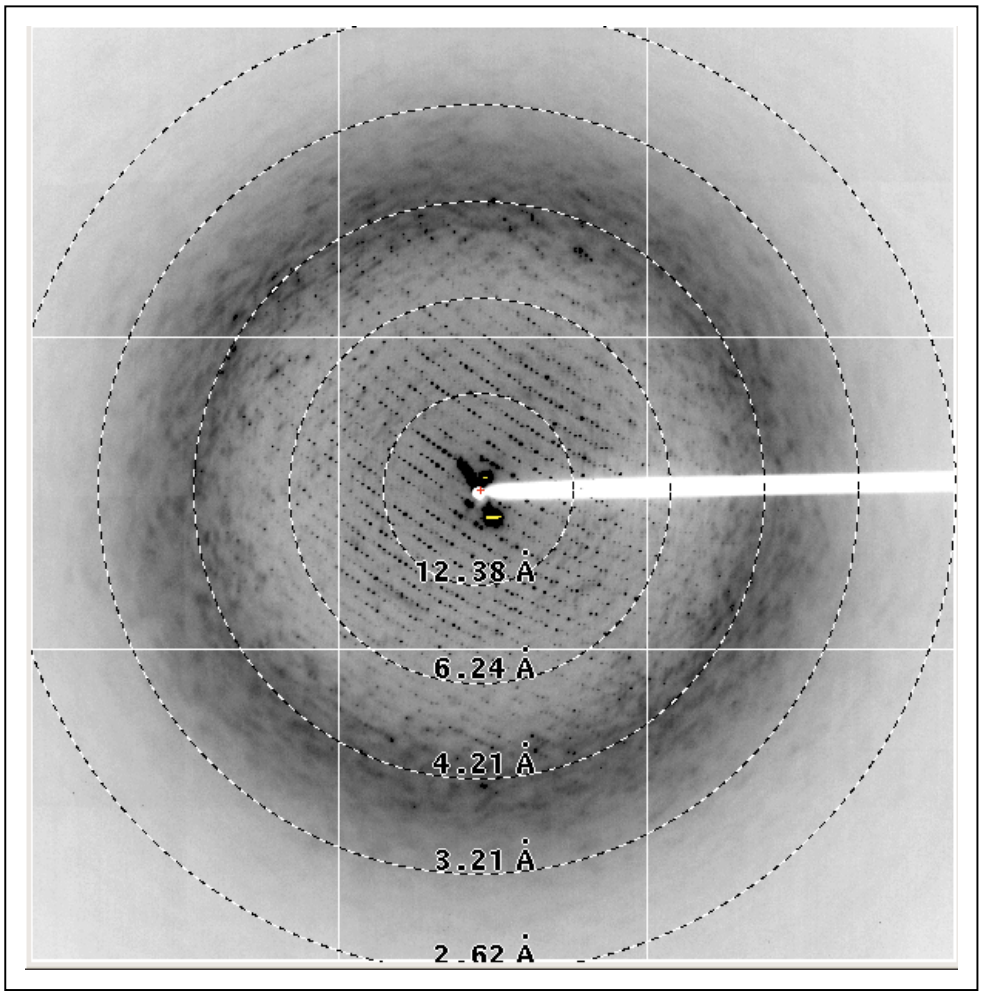

Figure 5.3. Diffraction pattern from a PSII crystal to a resolution limit of approximately 4 Å. This diffraction pattern was collected at the Advanced Light Source at Lawrence Berkeley National Laboratory. Figure courtesy of Dr. Raimund Fromme.

5.2. DNA TETRAHEDRON DESIGNS

A schematic view of the tetrahedron constructs investigated in this study is shown in Figure 5.4, which include a 20T (20 base pairs on each edge), [29] 20x30T (asymmetrical with 20 base pairs on each edge for one face and 30 bp on each edge for the other faces), [29] and a 30T (30 base pairs on each edge) tetrahedron. The size variations were designed to increase the cavity size which would in a later stage of the project allow for the incorporation of larger proteins and macromolecules inside the tetrahedrons. The sequences of all strands for each of the three constructs are described in Materials and Methods. While the 20T tetrahedron has an estimated inner volume of 32,364 $Å^3$, the inner volume is significantly increased to 58,955 $Å^3$ for the 20x 30 T construct and 125,064 $Å^3$ for the 30T tetrahedron. Assuming a sphere fitting inside of each symmetrical tetrahedron, it would have a diameter of 70 Å for the 20T and 100 Å for the 30T tetrahedron. The increased size of the larger tetrahedron constructs is confirmed by native gel electrophoresis as shown in Figure 5.7 c-d.

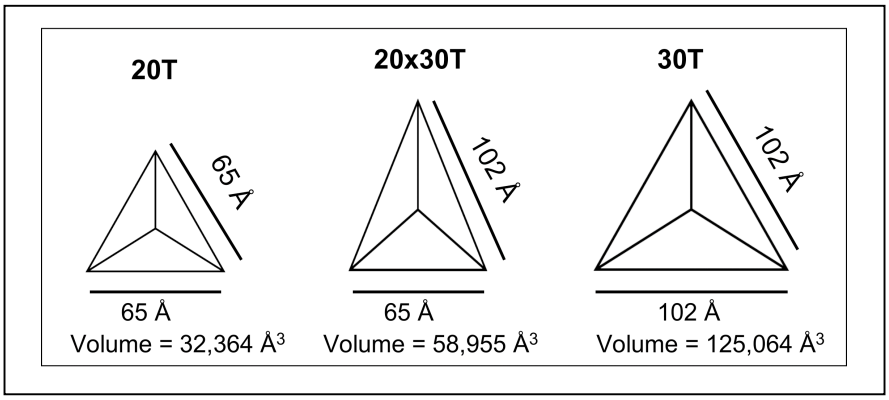

Figure 5.4. Dimensions of tetrahedra described in this work. Figure submitted to the journal *Acta Crystallographica F.* October 2012 and is currently under review.

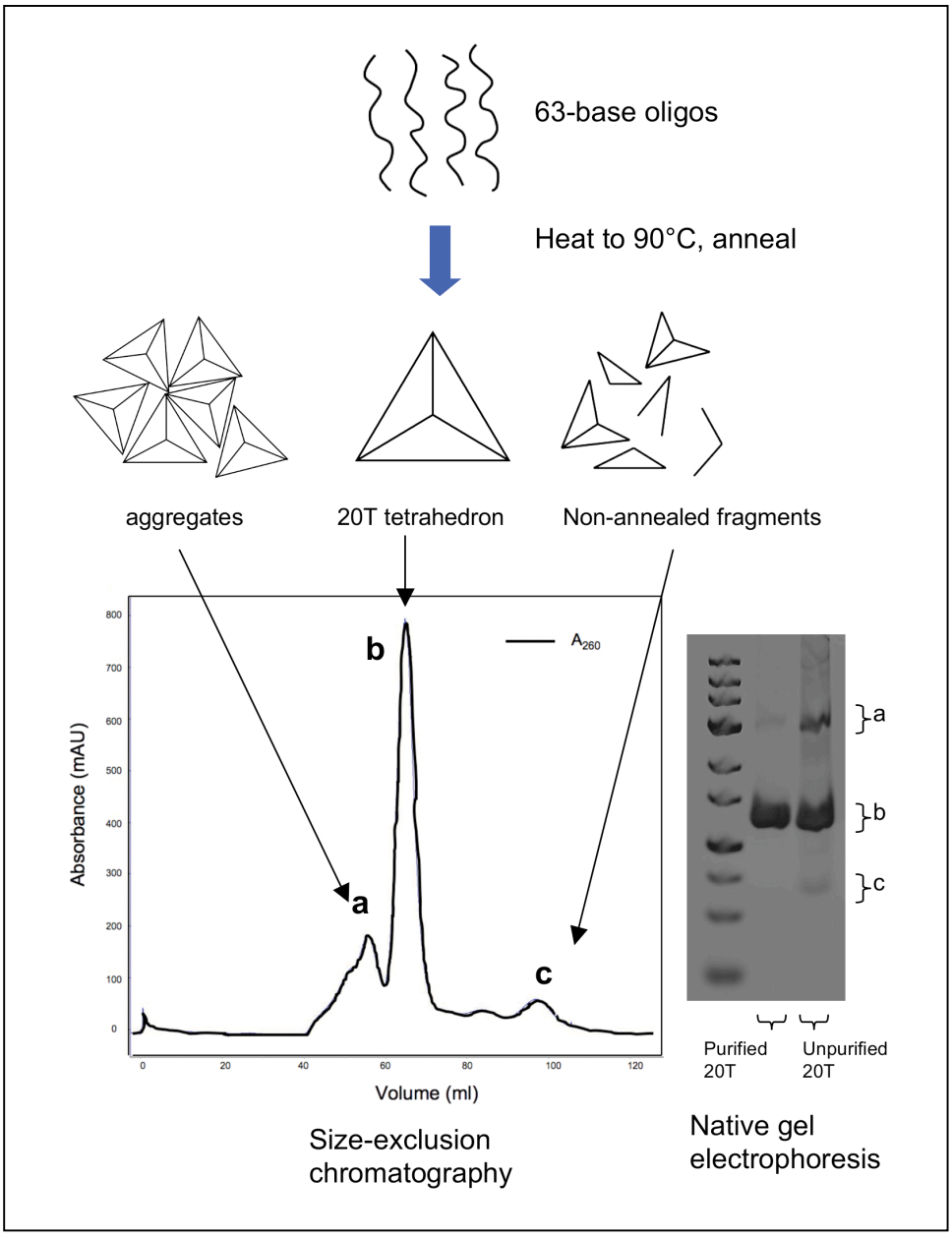

Figure 5.5. Purification scheme for 20T tetrahedron. The same purification procedure was used for other constructs. Both size-exclusion chromatography and native gel electrophoresis verified that the aggregates and fragments were isolated from the monomeric 20T. This same scheme was used for other constructs as well. Figure submitted to the journal *Acta Crystallographica F.* October 2012 and is currently under review.

5.3.1. Tetrahedron preparation results

The 20T tetrahedron was successfully purified using size-exclusion chromatography, as shown in Figure 5.5. The figure shows a schematic overview of the assembly and purification indicating the annealing of the four single-stranded DNA oligonucleotides, and the purification via size-exclusion chromatography. The purification procedure is verified by native gel electrophoresis of the sample before and after size exclusion chromatography (Fig 5.5 bottom right) which shows that the aggregates (band "a") and partially assembled structures (band "c") are successfully removed from the fully assembled tetrahedron monomer (band 'b') by the purification procedure. 80% of the DNA could be recovered as monomeric tetrahedron from the SEC column runs.

5.4 TETRAHEDRON CHARACTERIZATION

5.4.1. Analysis of homogeneity of the preparation

For each construct, the homogeneity of the sample was verified by analyzing the sample before and after purification on a 5% native polyacrylamide gel. Additionally, DLS was used to demonstrate homogeneity following purification, described below in more detail. Table 1 describes the calculations used to quantify the amount of aggregation in the sample.

5.4.2. Quantification through UV-Vis

The concentration of the tetrahedron was verified through UV-visible spectroscopy by measuring the absorbance of dsDNA at 260 nm using a molar extinction coefficient of 2,109,396 M^{-1} cm^{-1} (calculated using the online calculator from Integrated DNA Technologies, Coralville, IA) Typically, the concentration of the obtained sample ranged from 10-40 μM at a volume of 100-200 μL.

5.4.3. Optimization of the annealing step – concentration dependence

In prior research [29] annealing concentrations of 5 μM or more were used to form DNA tetrahedron structures from for the single-stranded DNA oligonucleotides. However, at these concentrations, large qualities of aggregates are detected by size-exclusion chromatography and native gel electrophoresis. As aggregation is a concentration dependent process, we tested if we can eliminate or reduce the formation of aggregates by varying the annealing concentration. During the annealing step, different concentrations of oligonucleotides were tested—ranging from 50 nM to 5 μM, and we also explored different cooling times. With the variation of the cooling time we wanted to explore if aggregate formation can be reduced by slower cooling rates that provides more time for the tetrahedron structures to form. The results are shown in Figure 5.6 for cooling times of 30 seconds and 90 minutes and DNA concentrations of 50nM, 0,2 μM and 0.5μM. The higher concentration during annealing of the 20T and 20x30T tetrahedra resulted in a significant amount of aggregation, as shown in Figure 5.6, lanes 1 and 3, while significantly lower

amounts of aggregates are observed at the 0.2 μM concentration shown in Figure 5.6a, lanes 2 and 4. Figure 5.6b compares the results for the 50 nM and 0.2μM concentrations of DNA. The results shows that aggregates could be further reduced for the 20T and 20x30T construct by decrease of the annealing DNA concentration to 50nM (compare lanes 3/4 and 7/8 (50nM) to lanes 1/2 and 4/5 (0.2 μM). In contrast to the clear concentration dependence, the annealing time had no detectable influence on the formation of aggregates as shown in Fig 5.6b where very similar ratios of monomers and aggregates are detected at annealing times of 30 seconds (odd numbered lines) and 90 minutes (even-numbered lines in Fig 5.6b).

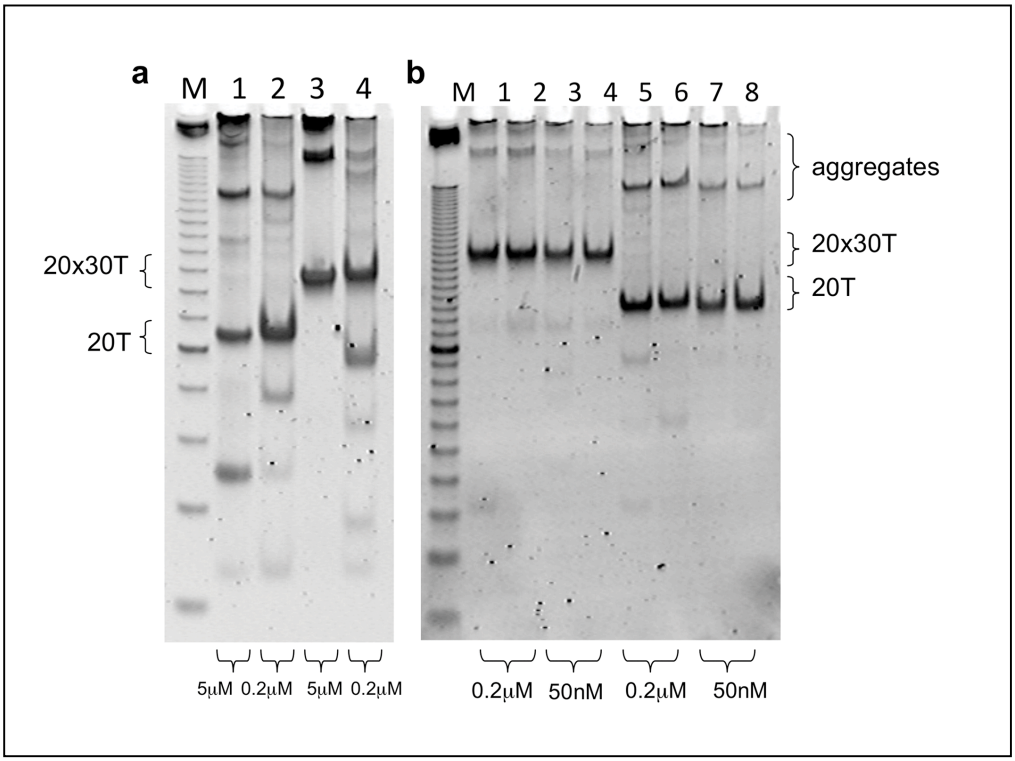

Figure 5.6. Concentration and time dependence studies during the annealing step of 20T and 20x30T constructs. The samples shown in (a) in Lanes 1 and 3 were annealed at a concentration of 5 μM which resulted in more aggregation than in Lanes 2 and 4 which were annealed in 0.2 μM. The gel in (b) shows even lower

annealing concentration comparisons. Lanes 1-2 and 5-6 were annealed at 0.2 μM and had more aggregation. Lanes 3-4 and 7-8 were annealed at a concentration of 50 nM and resulted in the least amount of aggregates. In (b), Lanes 1,3,5,7 samples were annealed in 30 seconds, while in Lanes 2,4,6,8 samples were annealed in 90 minutes. The time did not have much effect on the aggregation of the sample. Figure submitted to the journal *Acta Crystallographica F.* October 2012 and is currently under review.

As the lower concentration of oligonucleotides at the time of annealing reduced the amount of aggregates formed, all samples used for characterization and crystallization experiments were annealed at a concentration of 50 nM and further purified by size exclusion chromatography.

5.4.4. Other constructs - 20T, 20x30T, and 30T Design, Isolation, and Characterization

In addition to the 20T tetrahedron, two other constructs were designed to increase the cavity size. The 20x30T tetrahedron and a 30T tetrahedron (see Fig 5.7a-b) were annealed and purified. Figure 5.7 shows the purification of the 20x30T and 30T by size exclusion chromatography and verification of the purification procedure by native gel-electrophoresis (see Fig 5.7 c and d).

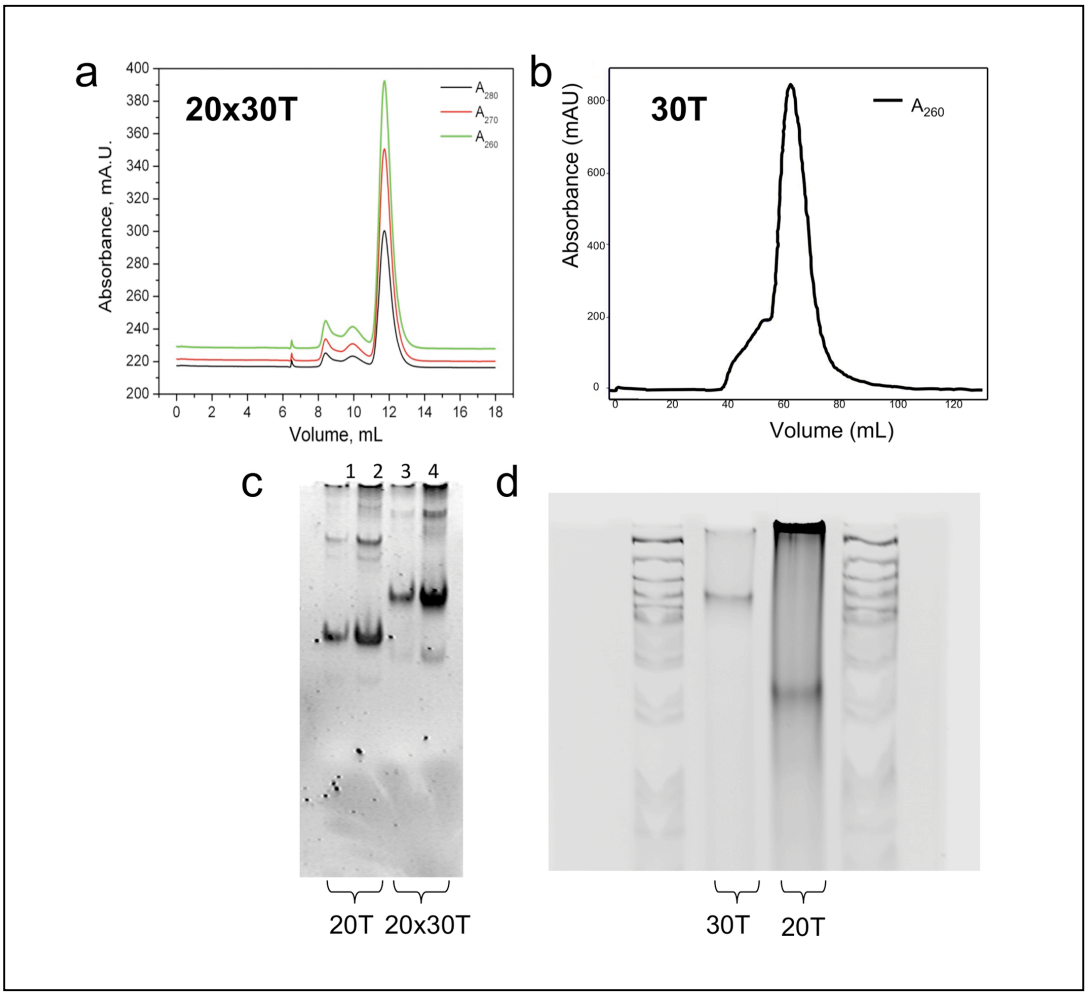

Figure 5.7. Chromatograms of 20x30T (a) and 30T (b) during the purification, and the resulting native gel mobility assays of the 20x30T (c) and 30T (d) in relation to the 20T, with noticeable mass differences. The samples described here were purified using SEC, but in (a) a different column was used with a lower volume compared to the column used in (b). Figure submitted to the journal *Acta Crystallographica F.* October 2012 and is currently under review.

5.4.5. Dynamic Light Scattering (DLS) Characterization of 20T Tetrahedron

X-ray structure determination requires crystals, and monodisperse samples are highly desired prior to crystallization. Traces of oligomers formed during the annealing step at low DNA concentrations are qualitatively removed by size

exclusion chromatography, but concentrating of the DNA tetrahedrons prior to crystallization could lead to reformation of aggregates. Dynamic Light Scattering (DLS) was used as a method to quantify the amount of aggregation present in the purified, concentrated DNA tetrahedron sample prior to crystallization. The DLS experiments revealed a hydrodynamic radius of approximately 4 nm (diameter 8 nm) for the monomeric 20T Tetrahedron, which confirms the expected size of our construct and these results are also consistent with the dimensions determined by cryo-EM. [31] The DLS results show a bi-modal size distribution of the DNA before size exclusion purification, with a monomer peak featuring a hydrodynamic radius of approx 35 ± 5 nm and an aggregate peak at radius of approximately 370nm. DLS data are shown in most publications in form of "radius-corrected" scattering intensities (scattering intensity is increased with r^6), which leads to suppression of aggregate peaks. However, we aimed for the detection of even small traces of aggregates and therefore we present the raw DLS data without "radius corrections" in Figure 5.8. Figure 5.8a shows the unpurified 20T tetrahedron at a concentration of 2.5 mg ml $^{-1}$ in 1X TAE-Mg^{2+} buffer before SEC purification. Two main peaks indicating a hydrodynamic radius of 3.4 nm and 37 nm with a large shoulder towards higher molecular weight aggregates appear. 5.8b shows the purified sample at a concentration of 2.5 mg ml $^{-1}$, indicating a monomer peak of ~4 nm and smaller aggregate peak at a size of 143 nm.

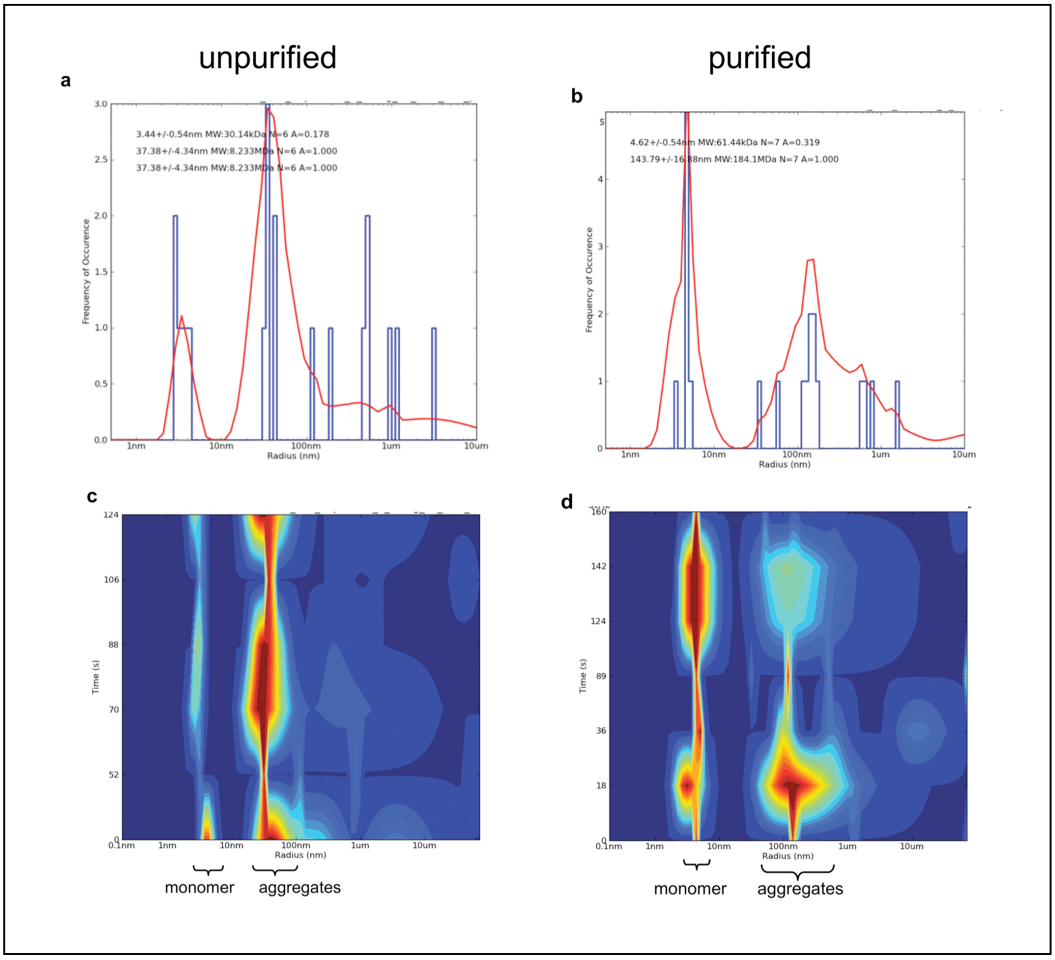

Figure 5.8. Dynamic Light Scattering measurements comparing unpurified and purified 20T tetrahedron. Figure submitted to the journal *Acta Crystallographica F*. October 2012 and is currently under review.

Figures 5.8c and 5.8d show the distribution plot of unpurified 20T (5.8c) showing more aggregates than the purified sample in 5.8d. The quantification of aggregates is summarized in Table 1. The evaluation of the data is based on peak integration, size of the aggregates and number of tetrahedrons per aggregate. The evaluation shows that the ratio of proteins that are present in from of aggregates versus monomers decreased from 3 10^{-4} before purification to 3.2 10^{-6} after

purification and ultrafiltration of the samples prior to crystallization. DLS can also be used to further study the crystallization process of

	before SEC purification	purified, concentr. sample
∫ aggregate peak (au)	0.5	0.28
∫ of monomer peak (au)	0.09	0.22
radius of aggregate peak (nm)	38	143
radius monomer peak(nm)	3.5± 0.5	4.6± 0.5
$\int / r^6$ aggregate	$1.8\ 10^{-10}$	$3.17\ 10^{-14}$
$\int / r^6$ monomer	$5.4\ 10^{-5}$	$2.26\ 10^{-5}$
$\int / r^6$ aggregate/$\int / r^6$ monomer	$3.3\ 10^{-6}$	$1.4\ 10^{-9}$
MW of aggregate	$8\ 10^6$	$1.84\ 10^8$
MW of monomer (Da)	$8\ 10^4$	$80\ 10^4$
no of monomers per aggregate	100	2300
$\int / r^6$ aggregate/$\int / r^6$ monomer x no of monomers per aggregate = ratio of number of DNA molecules present in aggregates/ no of DNA molecules in monomers	$3.3\ 10^{-4}$	$3.22\ 10^{-6}$

Table 1. Data evaluation of Dynamic Light scattering results.

the tetrahedron – from initial set up of the hanging drop, to nucleation, and the growth of the crystals [45].

5.5 TETRAHEDRON CRYSTALLIZATION

5.5.1. Crystallization results

In the first step in the crystallization process, we screened a large amount of conditions using sparse matrix screens (Sigma, St. Louis, MO). Initial screening indicated crystallites in the following conditions:

- 50 mM cacodylate pH 6.0, 20 mM argininamide, 1 mM barium chloride, 2 mM spermidine hydrochloride, 30% PEG 400
- 50 mM HEPES pH 7.0, 1 mM cobalthexamine chloride, 35% PEG 400
- 50 mM cacodylate pH 6.5, 20 mM lithium chloride, 5 mM cobalt (II) chloride, 35% PEG 600
- 50 mM HEPES pH 7.0, 20 mM ammonium chloride, 5 mM $MgCl_2$, 35% PEG 600
- 1 mM cobalthexamine chloride, 2 mM putrescin hydrochloride, 35% PEG 600
- 50 mM cacodylate pH 6.0, 20 mM argininamide, 1 mM cadmium chloride, 30% PEG 1000

Comparing the conditions, we noticed that all crystallization conditions that produced initial hits had a pH between 6.0-7.0. Most of the crystals were very small and showed visible defects, such as being hollow or clustered. Crystals grown using PEG-1000 as the precipitant analyzed for their diffraction at synchrotron sources and a resolution of ~10Å was observed. We screened multiple additives including argininamide, which gave the initial hit to improve crystal quality. Most of these additives contained the positively charged amine groups that may aid in stabilizing the structure of the DNA via electrostatic interactions by minimizing charge repulsion of the phosphate backbone [60,61]. After several round of optimization, optimized conditions were established in 29-34% PEG-1000, 10-25 mM L-argininamide, and 50 mM sodium cacodylate pH

6.0 using the hanging-drop vapor diffusion technique. Crystal sizes in the sitting drop setup ranged from approximately 50-100 μm in conditions with higher PEG 1000 concentrations to 100-500 μm at the largest with lower PEG 1000 concentrations ranging from 28-32%. Under optimized conditions, tetrahedron crystals grew in approximately 2-3 days at 23°C. The crystal shape was consistently rectangular, colorless, and transparent, but even after optimization, many crystals showed visible defects. Figure 5.9a shows a large crystal grown in 50 mM sodium cacodylate pH 6.0, 10 mM L-argininamide, and 29% PEG-1000. The large crystal was 400 μm long and 40 μm thick. Figure 5.9b shows crystals grown in an experiment under similar conditions with the use of human hair as a seed. These crystals were grown in 50 mM sodium cacodylate pH 6.0, 15 mM argininamide, and 32% PEG-1000. Most of the crystals grew on the surface of the hair and their average size was 50 μm in length and 10 μm in diameter. They also displayed a more solid and stable appearance during crystal handling, mounting and freezing. These smaller crystals showed less defects than the larger ones.

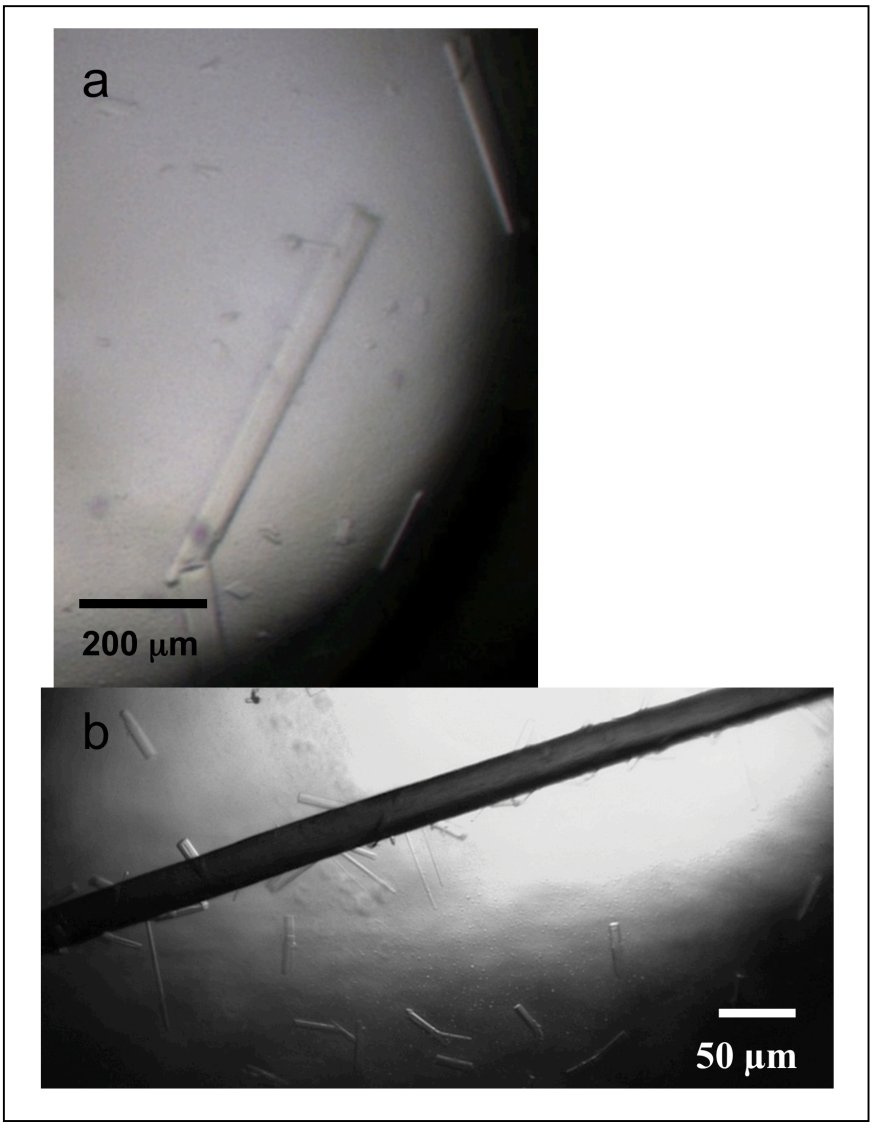

Figure 5.9. Crystal size comparison of largest crystals observed. DNA tetrahedron crystals grown in varying conditions. In 5.9a, crystals were grown in 50 mM sodium cacodylate pH 6.0, 10 mM L-argininamide, and 29% PEG-1000. In 5.9b, crystals were grown in 50 mM sodium cacodylate pH 6.0, 15 mM argininamide, and 32% PEG-1000 in the presence of human hair. Figure submitted to the journal *Acta Crystallographica F*. October 2012 and is currently under review.

We tested a large range of cryo-protectants and best freezing conditions were established by use of a cryo-solution that contained 1.2-2 times higher concentration of precipitant, buffer, and salt than the reservoir solution. Upon incubation in cryoprotectant solutions for 30 minutes, the crystals were mounted in 0.05-0.2 mm loops and were flash-frozen in liquid nitrogen. Crystallization of the 20x30T and 30T was also attempted. However, crystallization trials so far did not yield crystals. We speculate that the increase of the tetrahedron size may allow for higher structural flexibility, which might be problematic for crystal formation.

5.5.2. Optimization of results to grow higher quality crystals

Seeding

Seeding experiments were attempted with the goal of growing higher quality crystals through heterogeneous nucleation using human hair. The crystals produced using heterogeneous nucleation are shown in Figure 5.9b, and there is an observable solidity in these crystals compared to crystals produced in traditional vapor diffusion methods without seeding. The crystals were significantly smaller, and some grew directly on the surface of the hair. In examining the crystals closely, there was no obvious splits or jagged edges like what was frequently seen in other crystals. See further text in this chapter for an analysis of x-ray diffraction quality of these crystals.

5.5.3. Role of magnesium and different magnesium salts

The use of divalent cations in DNA preparations is very prevalent due to their interaction with the phosphate backbone. During the annealing step in preparing the tetrahedron, 12.5 mM magnesium acetate was present in the buffer, 1X TAE-Mg^{2+}. The tetrahedron was purified using different concentrations of the buffer, such as 2X and 5X TAE-Mg^{2+}. However, if the concentration of magnesium acetate was too high, more aggregates were present on the chromatogram during the purification. Therefore, different magnesium salts were tested such as magnesium chloride and magnesium sulfate in the crystallization screen solutions. In an attempt to further improve crystal quality, magnesium was used as an additive in the crystallization screens. However, this did not significantly change the crystal quality.

5.5.4. Importance of additives including argininamide

It is well understood that argininamide plays an important role in stabilizing the negatively-charged phosphate backbone of the DNA [61]. Through electrostatic interactions, the argininamide offers a bridge between dsDNA edges that would otherwise repel each other. Argininamide is also present in many DNA-protein aptamer crystal structures [60]. In the case of the crystallization trials of the 20T tetrahedron, the crystal screen solutions containing the argininamide produced the highest quality crystals in the entire suite. Other additives that were further explored include cobalt hexammine, spermidine, and spermine. All of these offer positively charged amine groups that aid in stabilizing

the negatively charged DNA backbone, and could aid in the formation of more crystal contacts, but the best results so far were obtained with argininamide.

5.5.5. Exploring pH and changing the buffer conditions in crystallization screens

As shown in the tables in the Materials and Methods and Appendices, crystallization screens were developed that contained different buffer systems that would alter the pH of the overall screen solution. The best conditions for the 20T crystals were 29-34% PEG-1000, 15 mM L-argininamide, and 50 mM sodium cacodylate pH 6.0. Screens were developed using Tris, Tris-sodium cacodylate, and MES. The results showed that crystals grew even in the conditions where the pH was 9.0. The best crystals grew in a pH of 9.0 and 7.0. The crystals appeared smaller and indicate less visual defects than crystals grown in a pH of 6.0. See Figures 5.10-5.11 for images of the crystals grown using the different pH conditions.

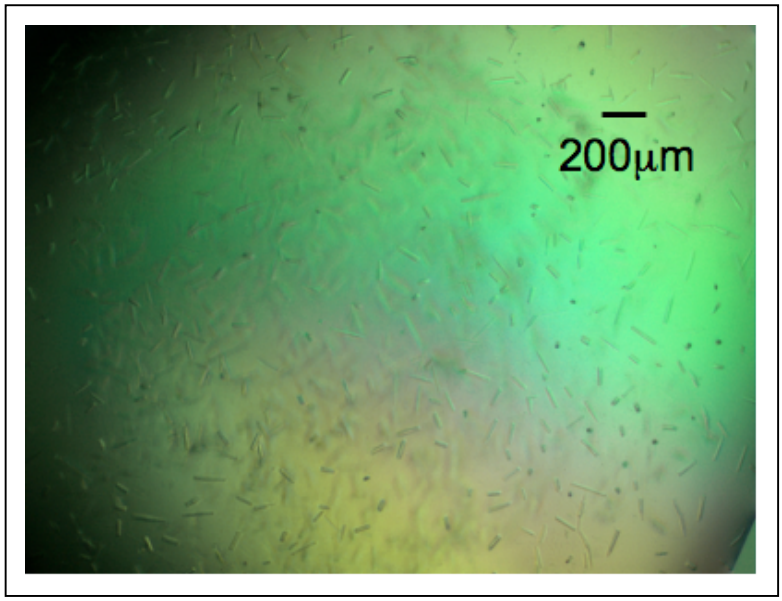

Figure 5.10. 20T tetrahedron crystals grown in 50mM MES pH 6.0, 15mM argininamide, and 30% PEG-1000.

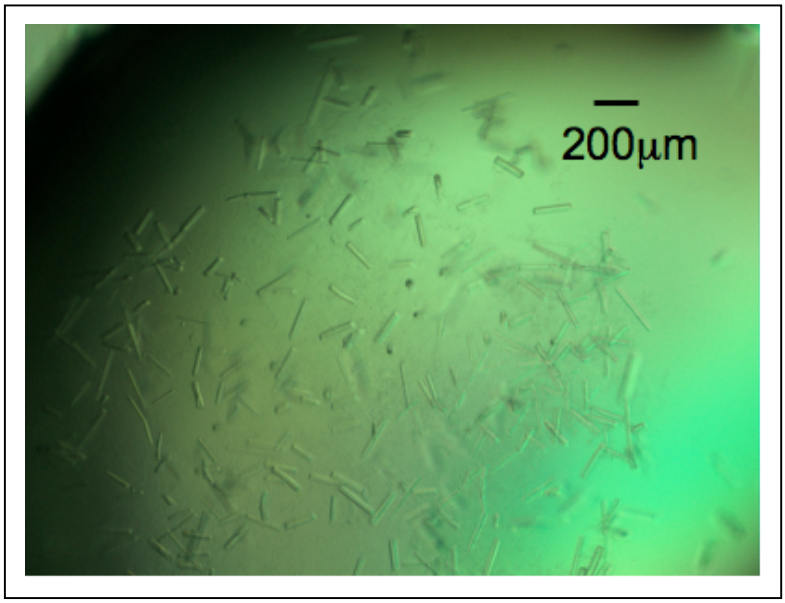

Figure 5.11. 20T tetrahedroncrystals grown in 50mM Tris pH 9.0, 15mM argininamide, and 30% PEG-1000.

5.5.6. Crystal dehydration experiments

In another attempt to improve the diffraction quality of the 20T tetrahedron crystals, the crystals were dehydrated prior to freezing and mounting for x-ray data collection. As shown in Figure 5.12 below, the setup involved transferring the crystals into 10 μL of a solution containing 35% PEG-1000, 10mM argininamide, and 50mM sodium cacodylate pH 6.0 on the post of a sitting drop tray. In the reservoir, 1000 μL of a screen solution containing 50% PEG-1000, 10mM argininamide, and 50mM sodium cacodylate pH 6.0 was added. The very high concentration of the precipitant "dehydrated" the crystal via vapor diffusion so as to produce a more densely-packed crystal. As shown in Figure 5.13 below, no degradation of the crystal occurred, even after incubating the crystals overnight.

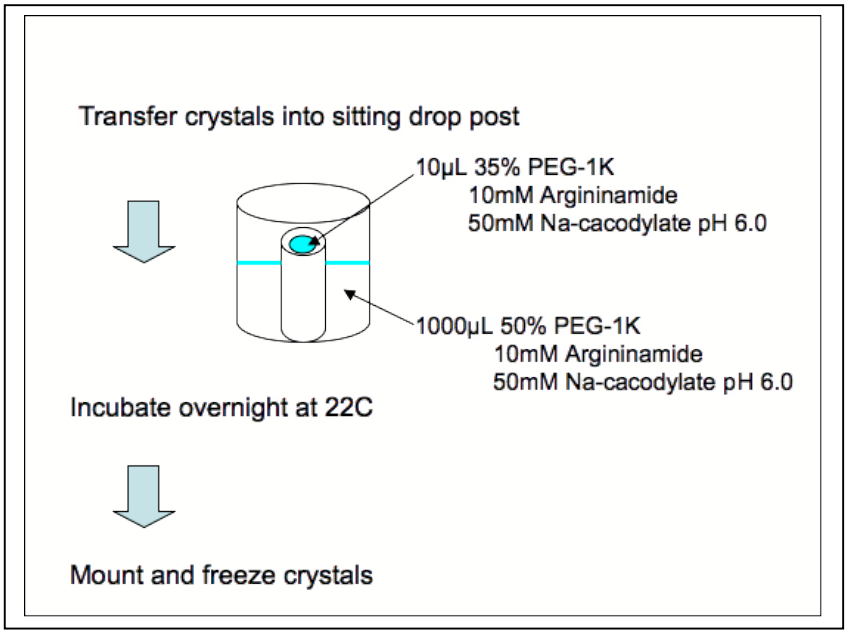

Figure 5.12. Schematic of 20T tetrahedron crystal dehydration.

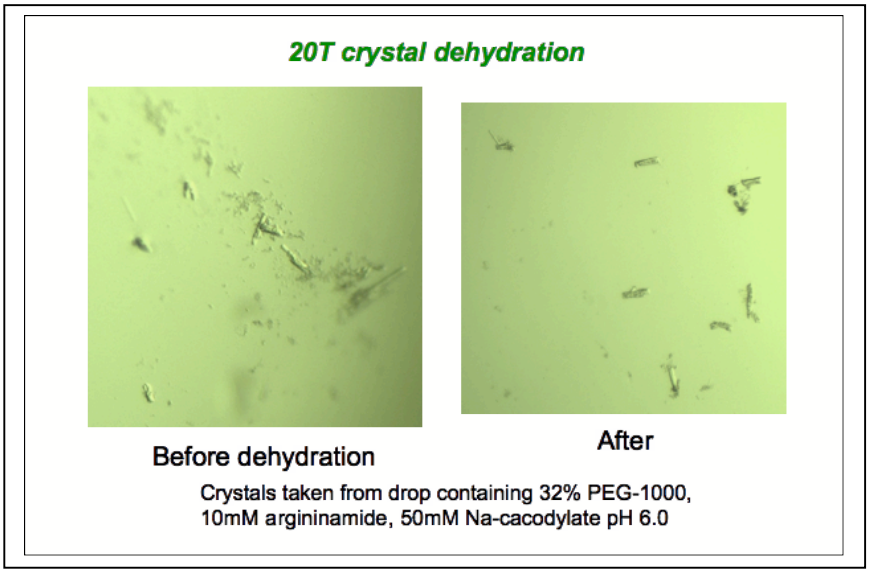

Figure 5.13. Images of the 20T tetrahedron crystals taken before and after dehydration. Crystals were incubated in the higher PEG-1000 solution overnight and still remained intact.

5.6. X-RAY DIFFRACTION DATA ANALYSIS

5.6.1. Conventional x-ray crystallographic data analysis of 20T tetrahedron crystals

X-ray diffraction experiments were conducted at the Advanced Light Source at Lawrence Berkeley National Laboratory at Beamline 8.2.1 and the Advanced Photon Source at Argonne National Laboratory at Beamline ID-19. The

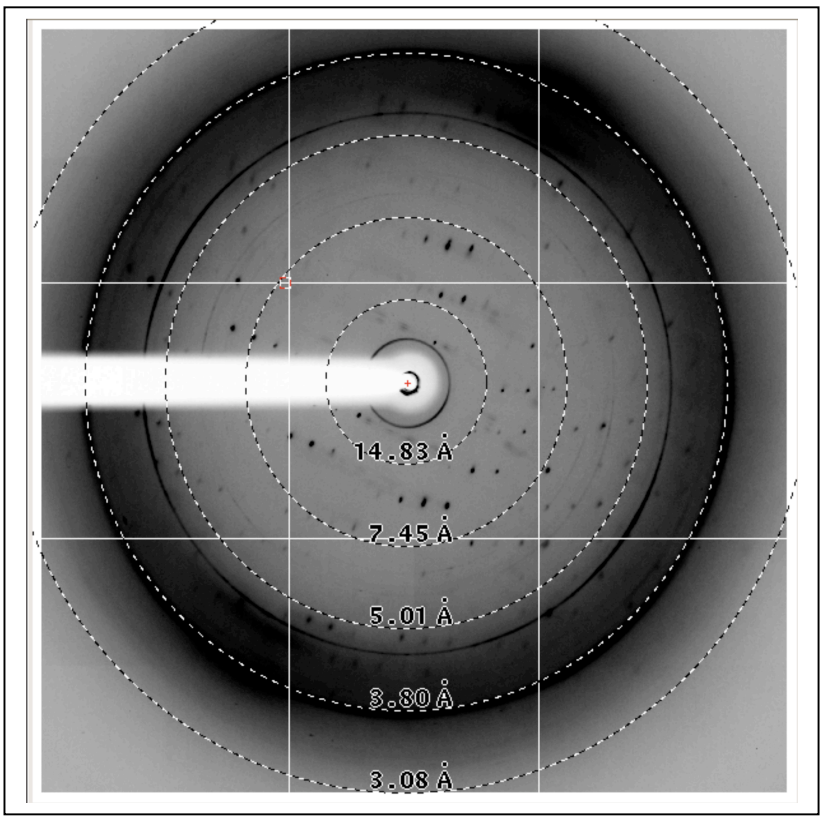

Figure 5.14. Single x-ray diffraction pattern of 20T crystals to a resolution limit of approximately 3.4Å. Figure submitted to the journal *Acta Crystallographica F.* October 2012 and is currently under review.

wavelength of the x-ray beam was 1 Å, photon flux was 10^{12} photons sec $^{-1}$, and the oscillation range was in most cases 1° per image, and the average exposure time was 3 seconds. The crystals were aligned in a cryo-stream of liquid nitrogen at a distance of 500 mm from the detector, and the detector size at APS was 3072 x 3072 pixels. Initial x-ray data analysis indicated poor diffraction to 10-20 Å. The use of argininamide lead to the improvement in the resolution to 6-7 Å. Further optimization lead to even greater improvement to a resolution limit of 3.4 Å. One of the 3.4 Å diffraction patterns is shown in Figure 5.14. We collected a data set of ~200 images on the crystals which show that they are highly anisotropic. Furthermore, the small crystals are very prone to x-ray damage so only 1-3 images could be collected. Subsequent images showed a degradation of the crystals, as shown in Figure 5.15. Figure 5.15a shows the very first image captured and 5.15f shows the crystal towards the end of the data collection. In the beginning of the data collection, spots are visible which represent a pattern

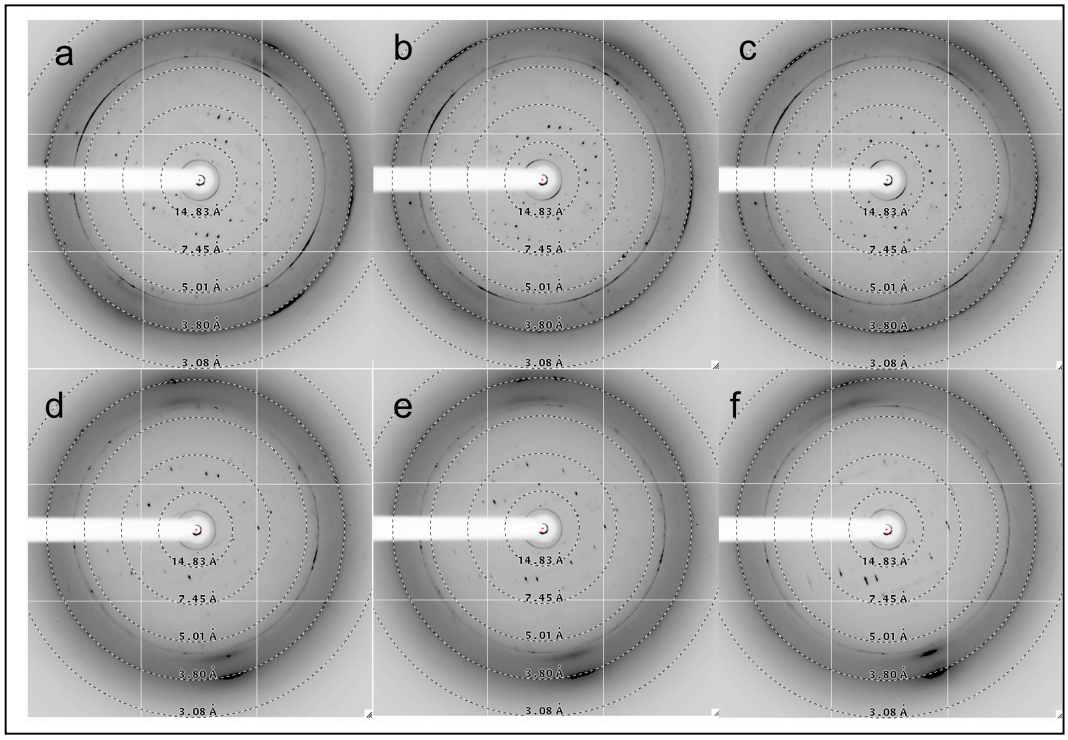

Figure 5.15. X-ray diffraction on a single 20T tetrahedron crystal over time. Figure submitted to the journal *Acta Crystallographica F.* October 2012 and is currently under review.

more characteristic of diffraction-quality crystals; whereas in 5.15f the spots not only diminish, but become very broad and faint. We also attempted data collection on the small crystals (~50 μm in size). However these small crystals were even more sensitive to x-ray exposure, and only about 3-20 images could be collected before the peaks diminished, with the smallest crystals decaying faster than larger ones.

5.6.2. Crystallographic Data Analysis

Although limited data were collected due to radiation damage and anisotropy of the crystals, a first approximation of the unit cell constants could be determined. The 20T tetrahedron crystallizes in unit cell C2 with unit cell dimensions of a=105, b=171, c= 59.4 Å, $\alpha = 90$, $\beta = 92.7$, and $\gamma = 90$. The unit cell dimensions are consistent with 2 tetrahedron molecules per asymmetric unit assuming a solvent content of 50%.

5.6.3. X-Ray Damage Investigations

In order to test if the tetrahedron was stable following exposure to synchrotron radiation, 20T crystals which had been used for data collection were dissolved in loading buffer containing bromophenol blue and xylene cyanol FF and applied onto a 5% native gel. Lanes 2-4 in Figure 5.16 contain 20T crystals from conditions in a screen ranging from 28-38% PEG-1000, 10-25 mM L-argininamide, and 50 mM sodium cacodylate pH 6.0. The results of the native gel electrophoresis (see Fig. 5.16) shows that the DNA tetrahedron monomer remains intact during exposure to synchrotron radiation, but this does not exclude damage to individual bases or destruction of crystal contacts. The radiation damage problem is the most detrimental obstacle for the x-ray structure determination of the tetrahedron. Radiation damage poses serious complications for nucleotide crystallography. Upon reaction with singlet oxygen or hydroxyl radicals, guanine is converted into 7,8-dihydro-8-oxoguanine (G_O). The G_O can still form a base-

pair with cytosine, but also incorrectly pairs with adenine. [62] This phenomenon would distort the structure of the tetrahedron. *In vivo*, DNA is also one of the most radiation sensitive biomolecules in the cell and sophisticated damage checkpoints and repair mechanisms exist, including the base excision repair mechanism, started by DNA glycosylases which recognize the damaged bases and excise them. [63,64] Additionally, the large tetrahedron crystals were not well-ordered in all dimensions,

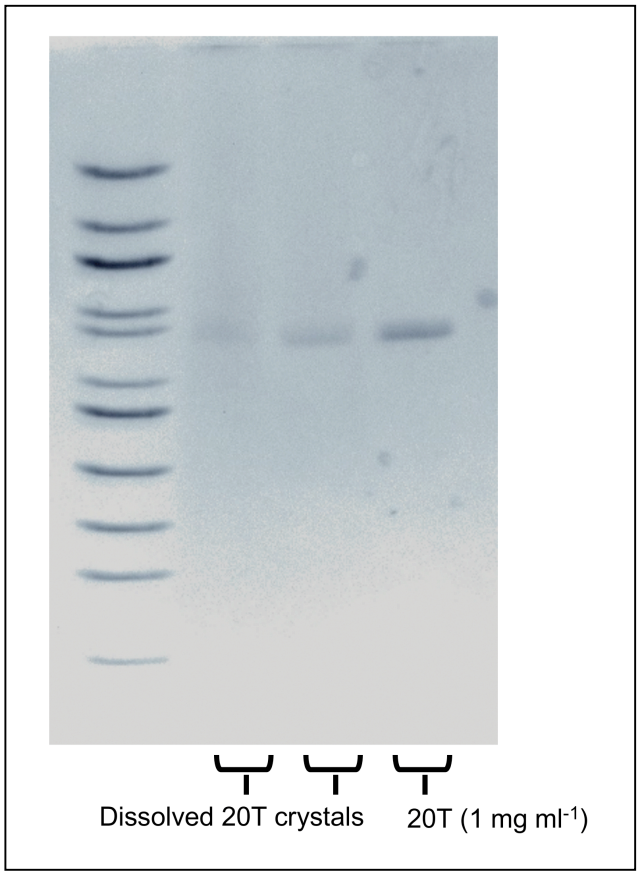

Figure 5.16. 5% native-PAGE of dissolved 20T crystals after exposure to synchrotron radiation. The first two lanes of the gel indicate only one or two crystals that were dissolved in tracking dye directly from the cryoloop, and the third lane indicates purified tetrahedron as a control. The bands match, indicating that no degradation of the DNA tetrahedron occurred.

resulting in anisotropy. The anisotropy of the crystal and the decay due to x-ray damage over time and space in the presence of the x-ray exposure shown in Figure 5.15 may be caused by a combination of radiation damage effects and effects of crystal anisotropy. It would be interesting to study in the future if the crystals could be improved by incorporation of a protein or peptide sequence inside of the tetrahedron to stabilize the tetrahedron within the crystal and reduce the anisotropy.

5.6.4. Microfocus beamline results

In order to examine multiple points along the same crystal to test for crystal defects, and to collect data on microcrystals, microfocused beams possessing diameters ≤10 μm were used. This also allowed for "scanning" of the crystal for both strong and weak diffracting points. As expected, certain regions of the crystals showed a higher degree of disorder compared to others. The microfocusing capability of the Advanced Photon Source Beamline ID-19 provided a straightforward strategy toward examining the apparent anisotropy of the tetrahedron crystals.

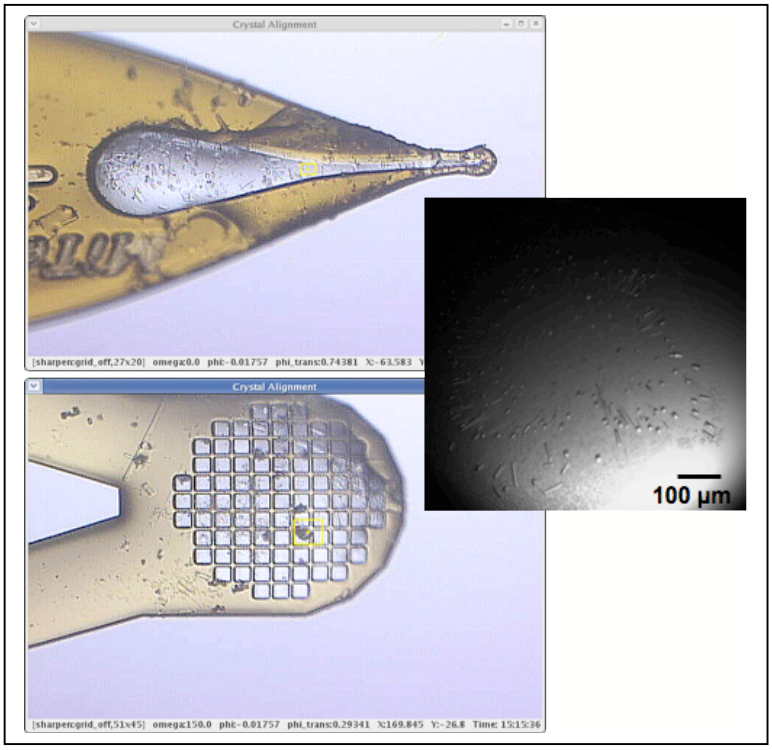

Figure 5.17. Microcrystals of 20T tetrahedron grown in higher PEG-1000 concentrations, and the loops used in x-ray diffraction experiments. The microcrystals were approximately 50 µm long and 10 µm wide.

5.7 TOWARDS NANOCRYSTALLOGRAPHY

In X-ray crystallography, freezing and X-ray structure analysis of the crystals under cryogenic conditions (77-100K) reduces the secondary radiation damage of the sample [65] , but even under cryogenic conditions 85% of the X-rays are absorbed leading to X-ray damage while only 5% are scattered [66].

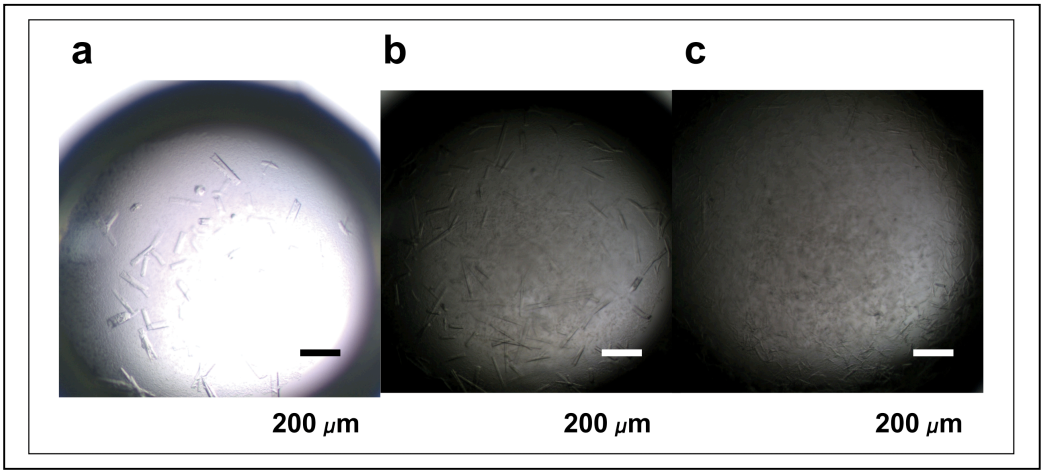

Figure 5.18. 20T tetrahedron crystals grown in varying PEG concentrations with the goal to grow micro/nanocrystals. Figure submitted to the journal *Acta Crystallographica F.* October 2012 and is currently under review.

Therefore a method is highly desired which would bypass the x-ray damage process altogether like data collection on hundreds of microcrystals using microfocused beamlines, and eventually analyzing nanocrystals by femtosecond nanocrystallography. Figure 5.18a-c shows the development towards the production of small crystals of the tetrahedron. Figure 5.18a shows crystals grown in 50 mM sodium cacodylate pH 6.0, 10 mM L-argininamide, and 30% PEG-1000, 5.17b shows crystals grown in 50 mM sodium cacodylate pH 6.0, 10 mM L-argininin amide, and 31% PEG-1000, and 5.17c shows crystals grown in 50 mM sodium cacodylate pH 6.0, 10 mM L-argininamide, and 32% PEG-1000. The crystal size visibly decreased with the higher PEG concentration. In 5.18a, the crystals were approximately 200-300 μm long, 100 μm long in 5.18b, and approximately 50 μm long in 5.18c. The ideal method to solve the x-ray structure

of the tetrahedron would avoid radiation damage using the diffract before destroy principle established in the new method of ther, such as testing microcrystals at a microfocused beamline, or using femtosecond nanocrystallography, [67,68] where millions of diffraction snapshots are collected from a stream of nanocrystals at room temperature by the use of femtosecond free-electron lasers.

5.7.1. Femtosecond Nanocrystallography Results

20T tetrahedron crystals were produced for analysis using the free-electron laser at the Linac Coherent Light Source beamline at Stanford. In order to successfully pass through the lines of the injector, the crystals could not be larger than 20 μm at their largest dimension. Crystals of the tetrahedron were produced during initial LCLS attempts; however, the size was no smaller than 30 μm and the crystals did not pass through the filter. During the next set of LCLS experiments, purified tetrahedron was crystallized on-site but due to material quantity limitations, the volume of the nanocrystal suspension was too small (100 μL) to be used for data collection. Future plans at the LCLS include an experimental scale-up of the tetrahedron preparation to provide enough crystals for one full data set to be collected. Beamtime (5 12-hour shifts) have been awarded at LCLS for the DNA crystals which will be scheduled in Spring 2013.

5.8 PEPTIDE CONJUGATION TO DNA

5.8.1. SYNTHESIS OF PEPTIDE SEQUENCES FOR THE DEVELOPMENT OF AN ARTIFICIAL OXYGEN EVOLVING COMPLEX

Conjugation strategy and designing a chemical linker

In order to design the aOEC, the peptides needed specific conjugation sites within the tetrahedron. A close-up view of the peptide sequences that are used in this work is shown in Figure 5.19. In natural PSII, these sequences provide the necessary amino acids that are MnCa cluster ligands. Therefore, synthetic sequences are used in this work also with the goal of ligating the MnCa cluster. In order to facilitate the encapsulation of the peptide sequences, a three-dimensional DNA tetrahedron is necessary as the stable framework. A schematic picture of this framework and the encapsulated synthetic aOEC is based on the natural protein environment in PSII and is shown in Figures 2.2-2.3. Based on that design, five proposed conjugation points as needed inside of the tetrahedron – two for the yellow sequence shown in Figure 5.20 (156-195-D1), two for the red peptide (347-360-CP43), and only one for the green peptide (CT-D1). Therefore, multiple covalent linker chemistries were devised. The first one

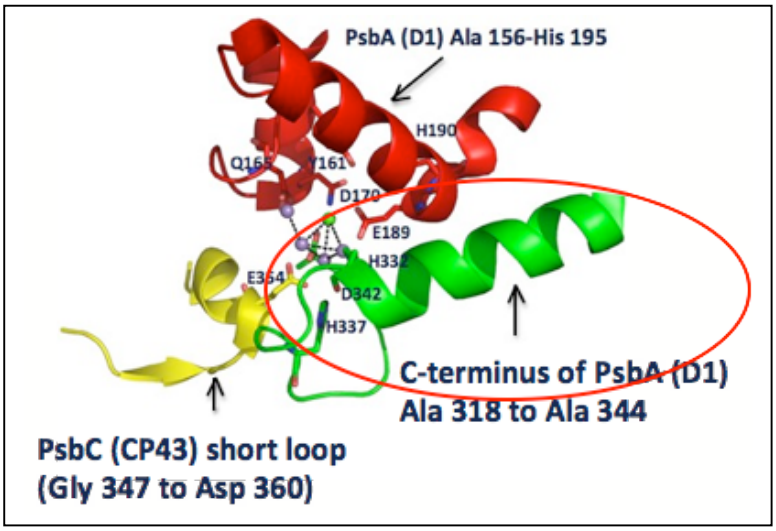

Figure 5.19. A closer view of the peptide environment surrounding the Mn cluster, emphasizing the CT-D1 peptide (shown in green). Adapted from pdb file 2AXT.

successfully conjugated was the CT-D1 peptide, the C-terminal peptide providing four ligands to the Mn cluster. The peptide was synthesized with a maleimide functional group at the N-terminus for coupling to a thiol-modified DNA base. The thiol sulfur reacted with the maleimide group to form a covalent bond in the presence of reducing agent, TCEP, to prevent undesirable side reactions. See Figure 4.6 for the reaction scheme.

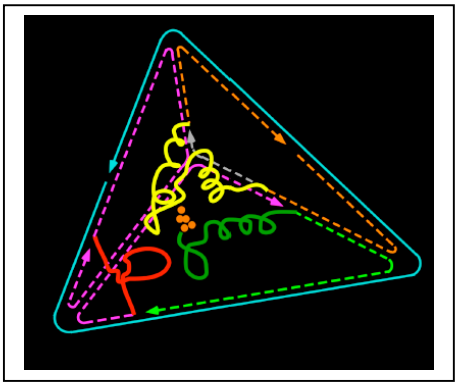

Figure 5.20. Schematic of artificial Oxygen-Evolving Complex organized in a 3D DNA tetrahedron. Figure courtesy of Chenxiang Lin.

Synthesis results and analysis of sequence

The "green" peptide sequence, named CT-D1 for C-terminal D1 subunit, was synthesized as described in Materials and Methods and purified using a C4 reverse-phase column. Tryptophan residues were added near the N-terminal end to allow for detection of fluorescence. The peptide sequence is shown in Figure 5.21. Additionally, glycine residues were also added to allow for flexibility near the conjugation site. Providing a connection site that was too rigid would possibly cause conformational changes in the tetrahedron. In order to verify that the large-scale purification of the peptide via reverse-phase chromatography was successful, the peptide was analyzed on a denaturing SDS gel, which showed a single-band product. See Figure 5.22.

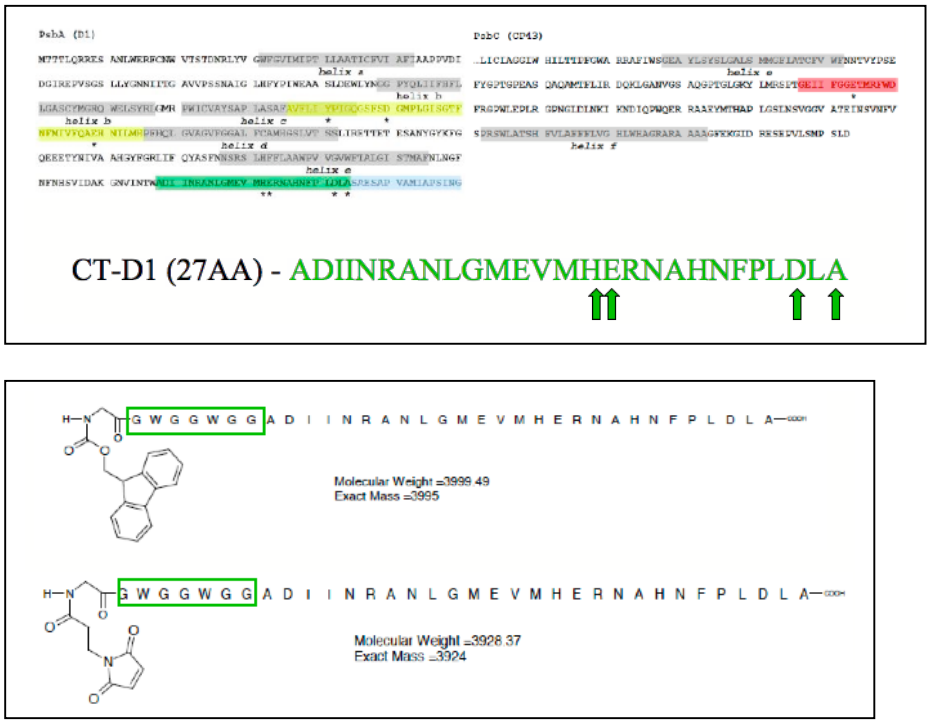

Figure 5.21. Proposed peptide sequences for aOEC design (top), emphasizing the CT-D1 sequence that has been synthesized and characterized so far. The green arrows indicate ligands to the MnCa cluster. The peptide synthesis was completed

by incorporating maleimidopropionic acid (top portion of bottom image), and GWGGWGG as the linker and later this maleimidopropionic acid group was chemically modified to obtain maleimide group (bottom portion of bottom image).

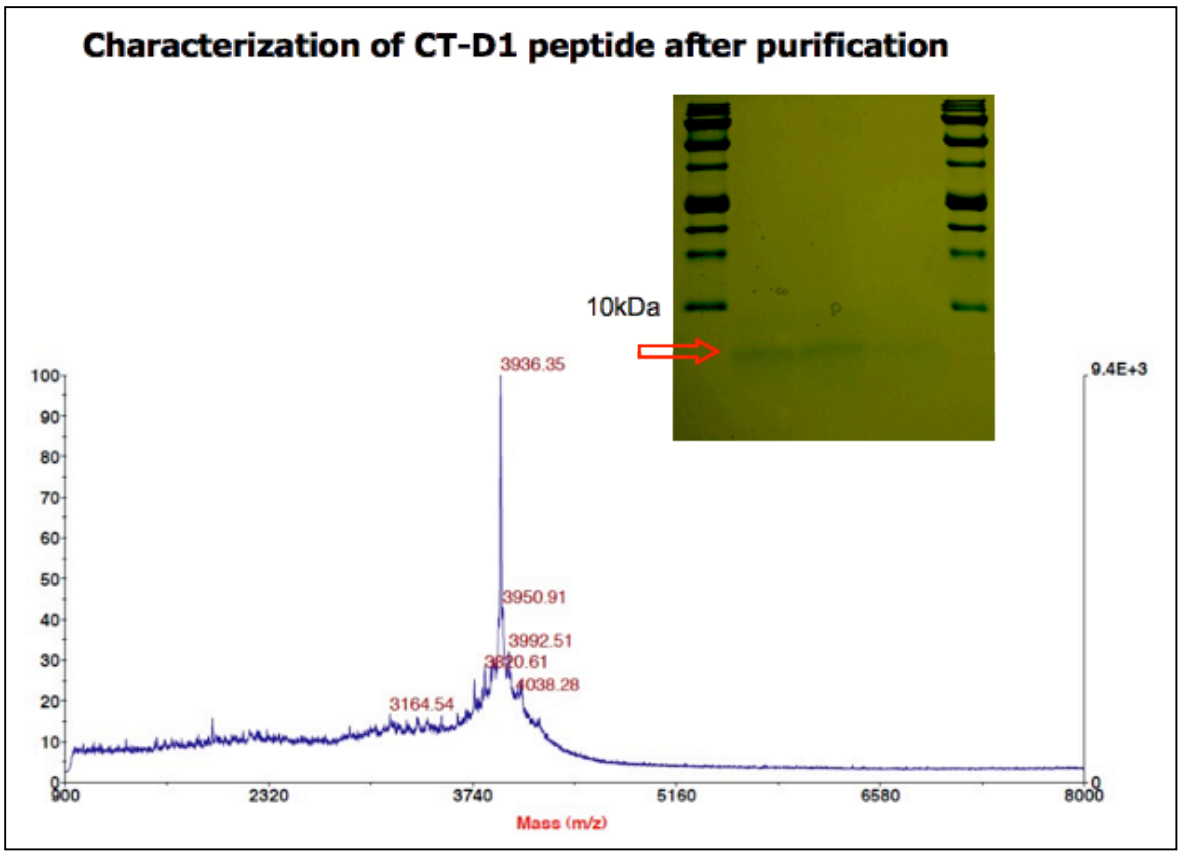

Figure 5.22. MALDI-TOF of the CT-D1 peptide sequence. The sample was mixed with a cinnaminic acid resin before drying. The inset shows the ~4 kDa single-band product after analyzing on a 20% Tricine-SDS-PAGE gel.

Secondary structure assignment

The CT-D1 peptide was characterized using circular dichroism (CD). Circular dichroism is used extensively to characterize a protein or a peptide's secondary structure. Biophysical characterization in this case is critical because the synthetic peptide described in these experiments must be as close as possible to its native counterpart for proper functionality. CD wavelength scans from 180-280 nm showed a minimum at 202 nm and a peak at 225 nm, indicating that the peptide was in a random coil conformation. The results show (See Figure 32) that the CT-D1 peptide did not fold on its own into the same conformation as the native peptide in PSII, as in the PSII complex the C-terminal region of the D1 subunit is approximately 50% alpha helical and 50% random coil. See Figure 5.23 for the image depicting the secondary structure of the CT-D1 peptide in its natural environment. The synthetic peptide in this case was in the random coil conformation and did not display any alpha helical content in 1X TA-Mg2+ buffer. (EDTA was eliminated from the sample buffer due to its UV absorbance properties). Typically, alpha helical proteins display minima at 208 and 220 nm. [69]

Manganese titrations

In nature, the manganese cluster is directly coordinated by the amino acids of the three peptide sequences. However, the cluster is deeply embedded into the lumenal side of PSII so that we cannot exclude that a larger second "coordination" sphere may be required for stabilization and assembly of the

cluster. The conformation of the peptide environment surrounding the manganese cluster depends on the presence of all of the amino acids. Manganese (II) sulfate was titrated into the CT-D1 sample at increments of 10mM in order to test if the conformational change may be induced upon metal binding. Mn(II) was not expected to significantly change the conformation of the peptide, considering that in nature the manganese cluster is composed of high valent Mn species (Mn(III) and Mn(IV)), and the cluster disassembles upon reduction of Mn(III) or Mn(IV) to Mn(II). Results shown in Figure 5.25 show that the addition of Mn(II) did not affect the secondary structure of the peptide, even at higher concentrations. There are two explanations why the peptide does not fold or bind Mn(II). First, the Mn may be required to be in the (III) or (IV) oxidation state to bind the peptide. Also, it is possible that all three peptides and the Ca2+ are required for the folding and assembly. Future experiments will aim at stabilizing the Mn(IV) in aqueous solution which would be a pre-requisite to repeating the titration experiments with Mn(III) or Mn(IV).

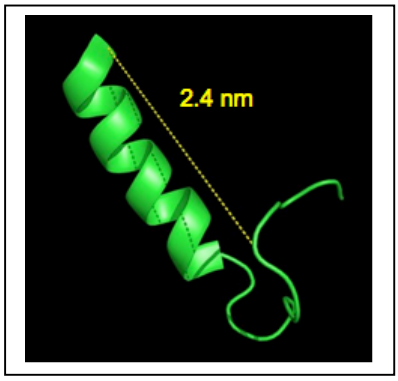

Figure 5.23. Secondary structure of the CT-D1 peptide sequence indicating approximately 50% alpha helical and 50% random coil in its natural environment. The C-terminal region is located at the random coil side. (pdb file 2AXT).

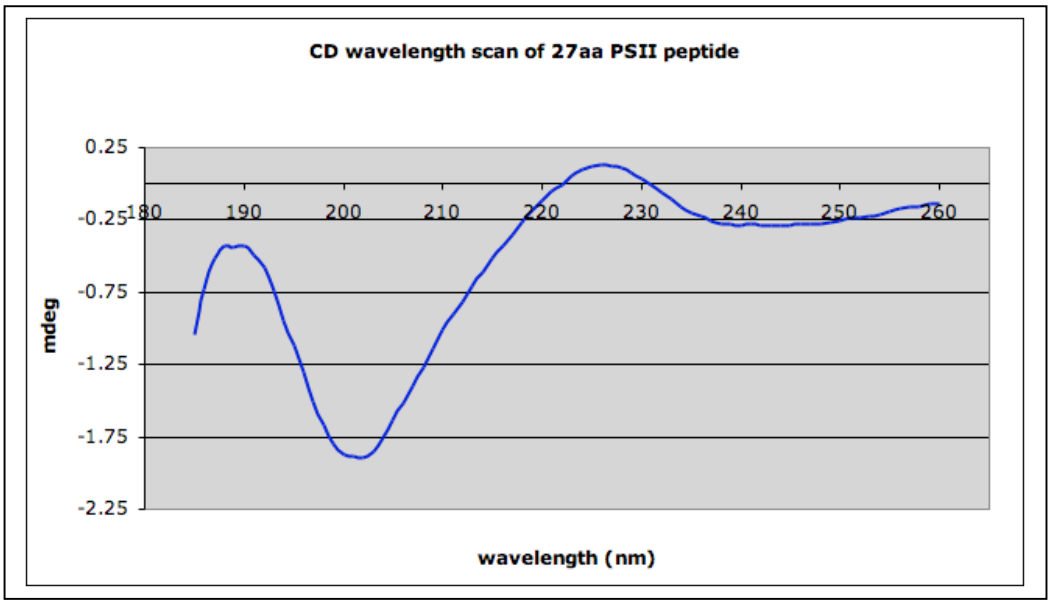

Figure 5.24. CD wavelength scan of 35aa peptide in 1X TA-Mg2+ buffer (40mM Tris base, 20mM acetic acid, 12.5mM magnesium acetate). EDTA was left out of this buffer solution due to its interference with the scan.

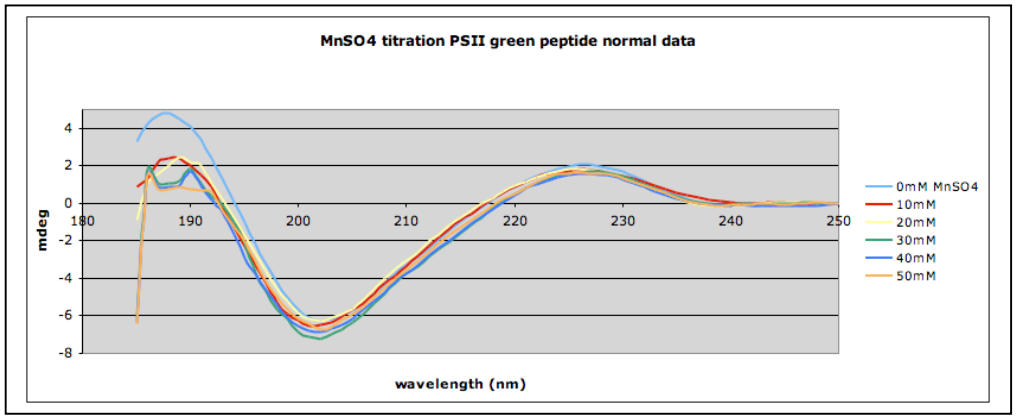

Figure 5.25. Manganese (II) titrations with the 35aa peptide. No obvious secondary structure changes were observed upon the addition of metals. The Mn would likely need to be in the Mn(III) or Mn(IV) state in order to induce a conformational change.

Results of covalently coupling to DNA

In the first step of building the aOEC, the CT-D1 peptide was coupled to the ssDNA strand 4 of the tetrahedron, and the details of the conjugation are outlined in the Materials and Methods. The coupling of the ssDNA to the CT-D1 peptide was done as described in Materials and Methods. A thiolated DNA base was reacted with a maleimide-functionalized peptide. The coupling of the CT-D1 peptide was confirmed through a denaturing PAGE gel mobility assay, as shown in Figure 5.26. This revealed that when the peptide was bound, as expected, the conjugate ran at a slightly higher molecular weight. This was due to the fact that the peptide added ~3.4 kDa of mass to the DNA.

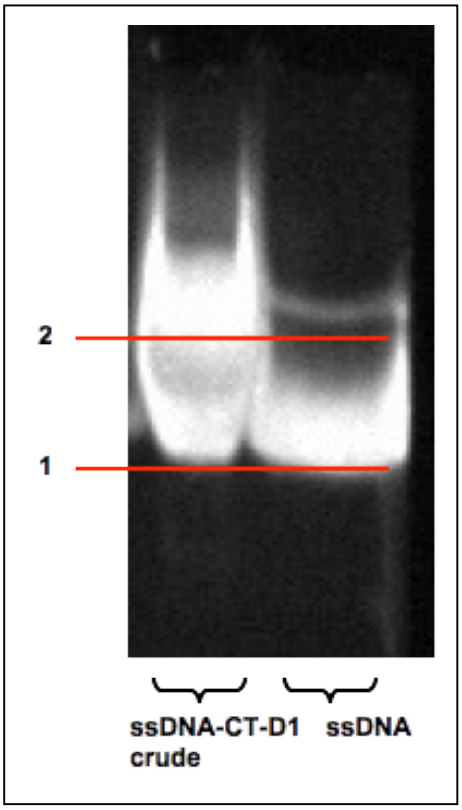

Figure 5.26. 10% denaturing PAGE gel-mobility assay comparing the molecular weight change of the thiolated ssDNA strand 4 before the peptide coupling (right lane on the gel) and strand 4-peptide conjugate crude product (left lane on gel). A mass change of approximately 3.4 kDa resulted after the peptide conjugation The line at 2 indicates the conjugate band, while the line at 1 indicates the thiolated DNA strand 4 band.

Crystallization experiments

After annealing and purifying the 20T-CT-D1 peptide conjugate, the sample was concentrated to 2 mg ml-1 and crystallized using PEG-1000, argininamide, and sodium cacodylate pH 6.0. Crystals formed in approximately one week and were grown at 18°C. The DNA-peptide conjugate crystallized in 29% PEG-1000, 10mM L-argininamide, and 50 mM sodium cacodylate pH 6.0.

See Figure 5.27 for crystal images. The crystallization results served as a confirmation that one of the PSII peptide sequences was successfully synthesized, purified, conjugated, assembled, and crystallized. See Figure 5.27 below.

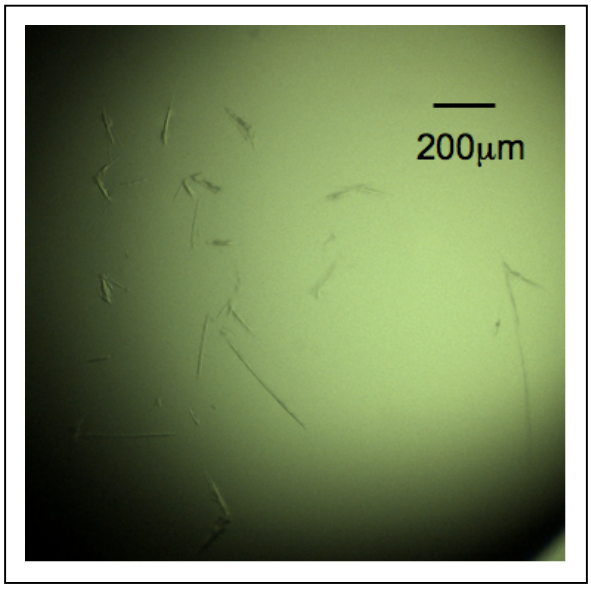

Figure 5.27. Crystals of the tetrahedron-peptide grown in 29% PEG-1000, 50 mM sodium cacodylate pH 6.0, and 10 mM L-argininamide.

Fluorescence microscopy of DNA-peptide crystals

We had introduced four Trp residues at the N-terminus of the peptide to allow for detection of the CT-D1 peptide by tryptophan fluorescence. Therefore, fluorescence microscopy was used to detect the peptide inside of the DNA-peptide crystals. The Trp fluorescence signal of the crystals was clear, as shown in Figure 5.28. The fact that we can detect the crystals by Trp fluorescence likely confirms that the peptide crystals indeed contain the tetrahedron conjugate and that the two were crystallized together. Future peptide constructs may also include Trp residues for use in fluorescence microscopy on crystals. The fact that the

tetrahedron-peptide conjugate crystallized under similar conditions as the empty DNA tetrahedron indicated that most likely the peptide is located inside of the cage after annealing. This result is very encouraging as it shows that the first milestone in the assembly of the PSII aOEC was reached.

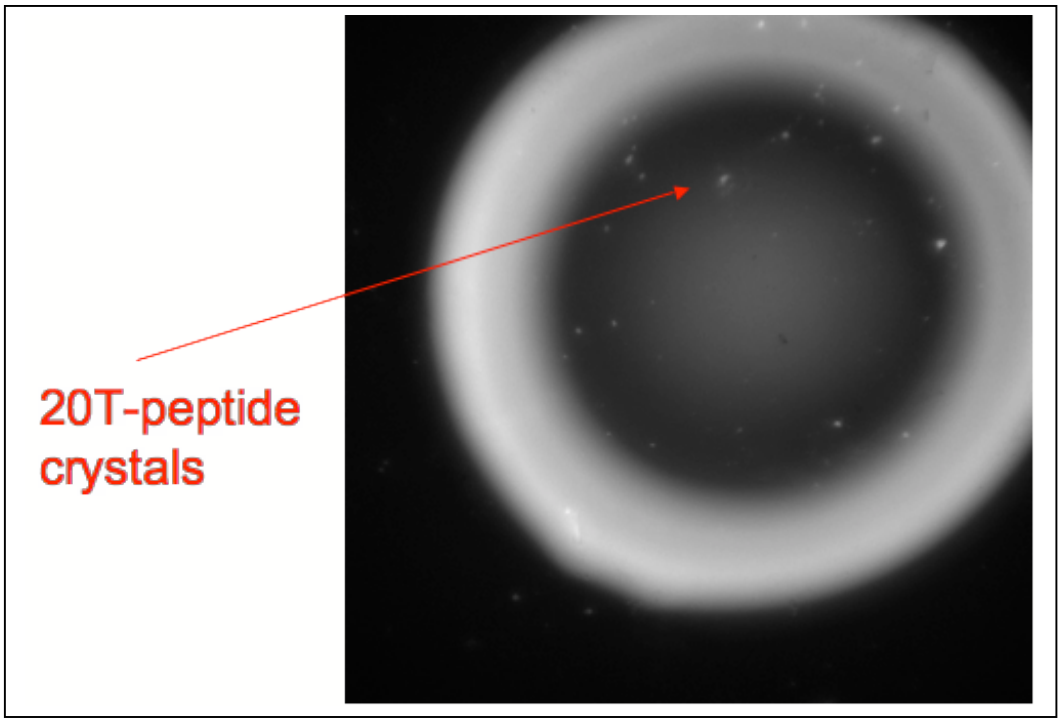

Figure 5.28. Fluorescence microscopy of tetrahedron-peptide crystals. The image is of a crystallization drop of approximately 2 μL.

5.8.2. PORPHYRINS AS “TEST” METAL CLUSTERS – ASSEMBLY AND CHARACTERIZATION

One of the key experiments in our work in redesigning the OEC resides in the characterization of assembled metal clusters. In this work, porphyrins are used as "test" metal cofactors, as they can be modified with several different macrocycle constituents, central metals, and axial ligands, and can be rendered soluble in aqueous solution. A large variety of porphyrins have been synthesized and characterized using UV-Vis spectroscopy and EPR. A central metal can be inserted into the porphyrin macrocycle that is paramagnetic and can be thus characterizable by EPR. The aforementioned spectroscopic techniques are important to the characterization of metal complexes, especially in the final aOEC construct which will contain high-valent manganese which is EPR active. As a proof of concept, metal-containing porphyrins, specifically Fe(III) meso-Tetra(4-sulfonatophenyl) porphyrin chloride, have been implemented for testing of the encapsulation of a metal-containing molecule inside of the DNA cage. Upon coordination of two orthogonally oriented peptides covalently attached to the DNA tetrahedron which contain terminal histidine residues, iron (III) switches from its EPR-active state (high-spin) to its hexacoordinated low-spin state (a total of six nitrogen ligands – two axial and four planar), as depicted in Figure 5.29, and the assembly can be analyzed using EPR and UV-Vis spectroscopy.

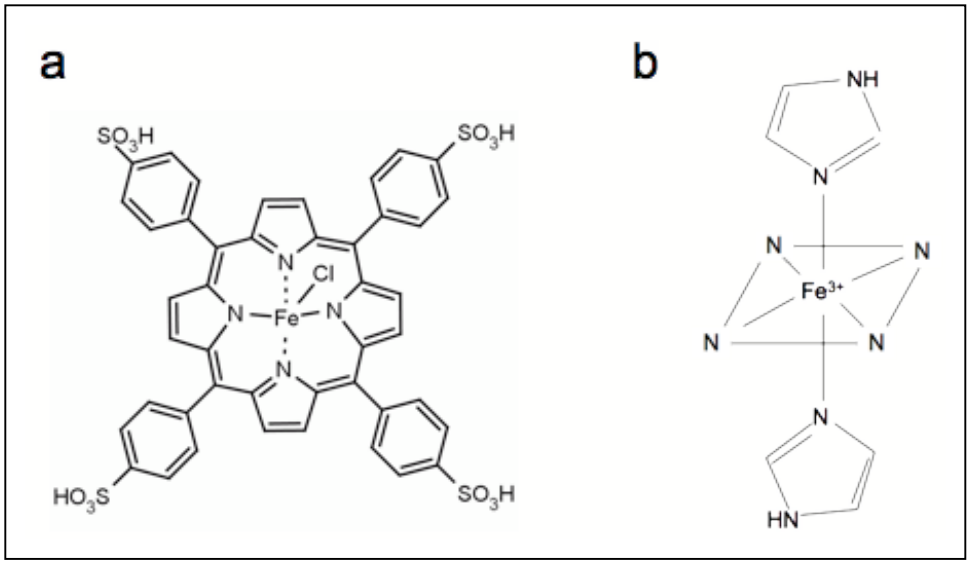

Figure 5.29. The porphyrin used in this work, Fe(III)-meso-Tetra(4-sulfonatophenyl) porphyrin chloride (Fe(III)-TPPS4), shown in (a). The coordination of Fe(III) via two more nitrogens is shown in (b). This is the proposed coordination used to assemble the peptides inside of the tetrahedron.

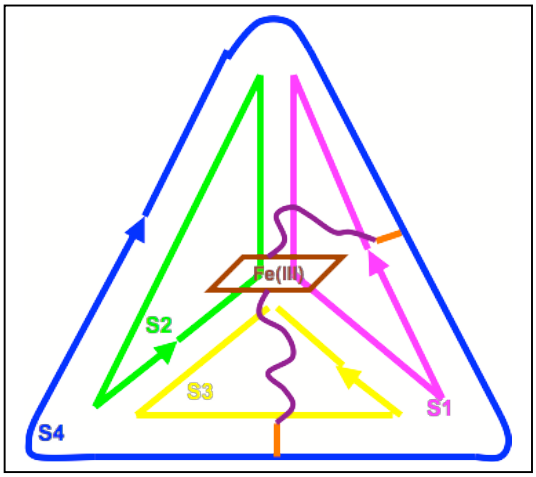

Figure 5.30. Schematic picture of the self-assembling porphyrin to the terminal histidine residues of the two P8 peptides (CAGAGSWH) covalently attached to DNA bases on strand 4 of the tetrahedron.

Peptide conjugation techniques and results

Figure 5.30 shows a schematic picture of the self-assembling properties of the peptides and porphyrin inside of the 20T tetrahedron. Two thymines with amine modifications were introduced into strand 4 of the tetrahedron which served as the conjugation sites for the peptides. See Figure 4.8 in Materials and Methods for the reaction scheme. The peptide sequence designed for the coordination of the porphyrin inside the cage was CAGAGSWH and is referred to as P8. This short 8aa sequence is approximately 2.4 nm in length if assuming that it does not fold into a secondary structure. The sequence contains a cysteine so the sulfur group could react with the maleimide of the heterobifunctional crosslinker SMCC to form a covalent bond between the DNA and the peptide. (Figure 4.8 in Materials and Methods). The amine-modified DNA strand was reacted for 3 hours at room temperature with a 100-fold excess of SMCC in acetonitrile. The reactive NHS ester group of the SMCC reacted with the primary amine on the amine-modified thymines of the DNA strand. The excess SMCC was successfully removed via two ethanol precipitation steps.. The ssDNA was coupled to the peptide via the maleimide group of the SMCC which reacted with the cysteine sulfur, as described in Materials and Methods. Thus, the heterobifunctional crosslinker served to conjugate ssDNA to the peptides in a highly reproducible manner.

Using SMCC as a heterobifunctional crosslinker

The use of SMCC as a crosslinker between nucleotides and peptides is well-established in the literature [58,70]. The reactive NHS ester interacts with the free amine group of the chemically modified DNA base (in this work, Thymine). See Figure 4.8 for the reaction scheme. Upon reaction in buffer free of primary amines (i.e., no Tris), the excess SMCC is readily separated from the DNA through ethanol precipitation steps. After removing excess SMCC, it was possible to conjugate a peptide containing a cysteine sulfur via the maleimide moeity of the SMCC. 100-fold excess peptide was added to the reaction mixture, which ensured that all DNA was conjugated. Following reaction at room temperature also in the presence of buffer free of primary amines, excess peptide was removed via size-exclusion gravity flow NAP-5 columns, and conjugates are easily quantified by measuring A260 for the DNA strand. In the NAP-5 columns, small molecules (peptides for example) are left on the column, effectively removing the excess peptide from the sample.

MALDI-TOF and gel mobility assay to confirm conjugation

Before we tried to assemble the ssDNA-peptide conjugates into a tetrahedron, the DNA-peptide conjugates were analyzed by electrophoresis. A 10% denaturing-PAGE gel shift asssay (See Figure 5.31) shows the small size difference between uncoupled purified ssDNA and peptide-coupled ssDNA. The size difference was approximately 1.5 kDa and was also verified by MALDI-TOF, shown in Figure 5.32. The expected molecular weight was 21,933 Da and

the observed mass was 21,467 Da. MALDI-TOF is notoriously difficult on long DNA sequences [59] (we have conjugated a 63-mer), and for this work a low concentration of 8 μM DNA-peptide was used. Therefore, the MALDI-TOF spectrum is noisy due to the low concentration and also possibly from residual salt remaining from the DNA sample preparation. In order to overcome the salt problem with the long DNA sequences [59], the DNA-peptide conjugate was first mixed with a DOWEX resin to remove excess salt, and then it was mixed with an excess of a saturated solution of 3-hydroxypiccolinic acid as the matrix.

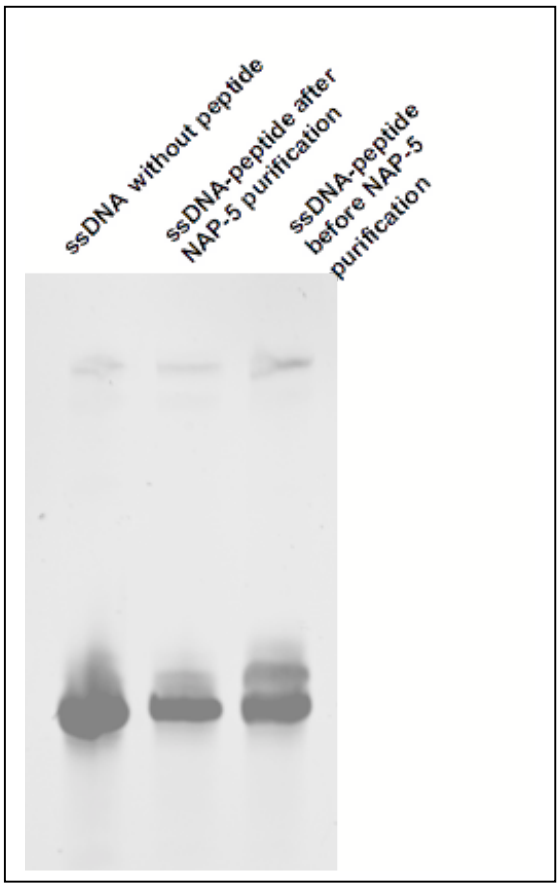

Figure 5.31. Results of denaturing-PAGE gel shift, indicating a slight mass change in the DNA-peptide conjugate.

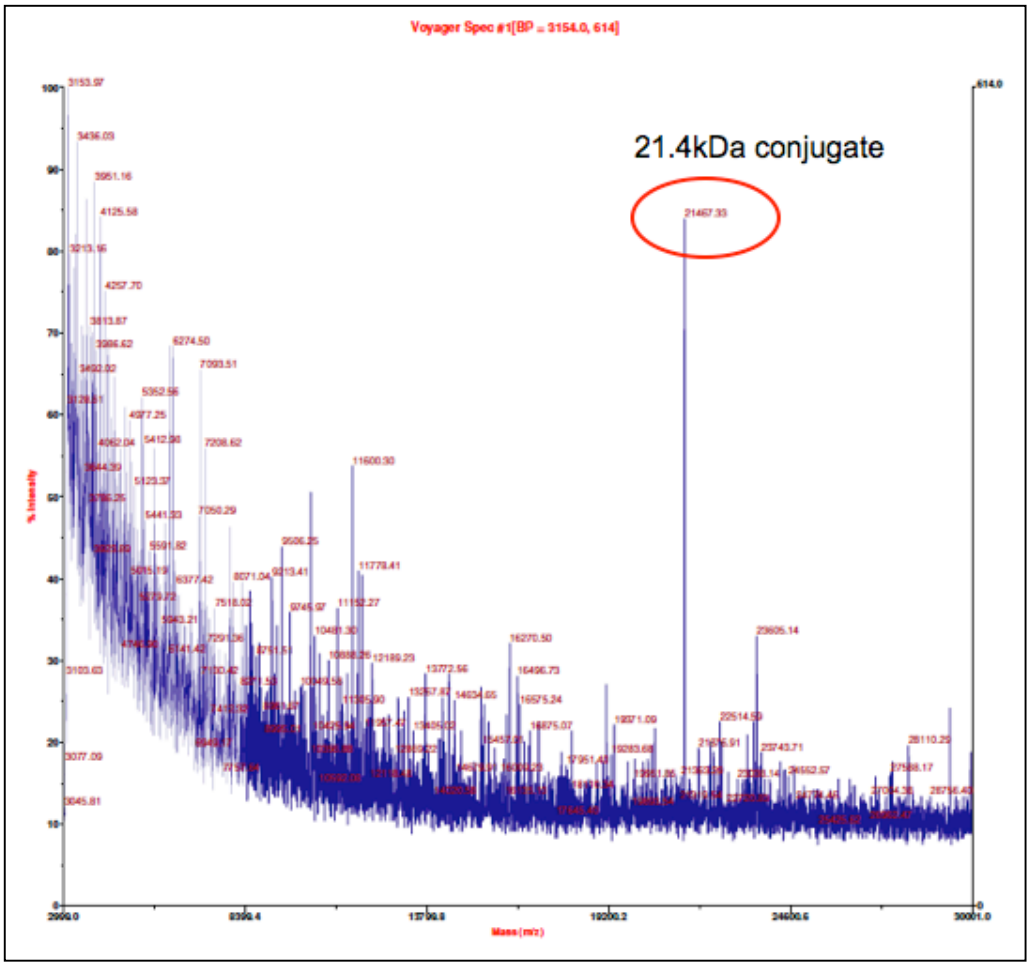

Figure 5.32. MALDI-TOF confirming conjugation of two peptides to the ssDNA, adding ~1.5 kDa of mass to the DNA strand.

Strategies for assembling tetrahedron-peptide-porphyrin complex (20TP8P)

Two strategies were employed for assembling the complete DNA cage with the peptides and porphyrin assembled inside, as indicated in Figure 4.7. One strategy, Scheme 1 (See Figure 4.7), required assembling the strand 4-peptide conjugate to the other three strands followed by the purification of this complex using SEC. The porphyrin was then introduced into solution, assuming it would

migrate into the center of the tetrahedron given that our calculations indicated that there would be enough space on each face of the tetrahedron for the porphyrin to enter into the cage. An alternative method, Scheme 2, involved mixing the strand 4-peptide conjugate with the porphyrin first, and then annealing the other 3 strands together but at a higher concentration of at least 5 μM porphyrin and 5 μM of the tetrahedron strands due to the fairly high dissociation constant of 2 μM that was calculated for the peptide-porphyrin binding. Calculations for the peptide-porphyrin Kd were performed by titrating the porphyrin with peptide.

Assembly of the 20TP8P Complex - Scheme 1

Following conjugation of the peptide to the ssDNA, annealing of the entire construct was performed by mixing the strands in equimolar concentration (50 nM) in 1X TAE-Mg2+ pH 8.0, heating to 90°C, and allowing the sample tubes to cool to room temperature over the course of 90 minutes. After concentrating the sample from approximately 450 mL to 500 μL, it was loaded onto a Superdex 200 size-exclusion column. As shown in Figure 5.33, the chromatogram indicates that the monomeric construct elutes around 65 minutes, which is similar to the elution time of the empty 20T tetrahedron, which elutes between 60-65 minutes. This result would be consistent with the assumption that the peptides are located in the center of the 20T tetrahedron. If the peptides were oriented outside of the cage, the elution time of the 20T peptide conjugate would decrease because the hydrodynamic radius of the structure would increase. The chromatogram shows

that few aggregates were formed during the annealing step. Following HPLC SEC purification, the monomeric tetrahedron-peptide complex was concentrated to 10 μM for porphyrin assembly.

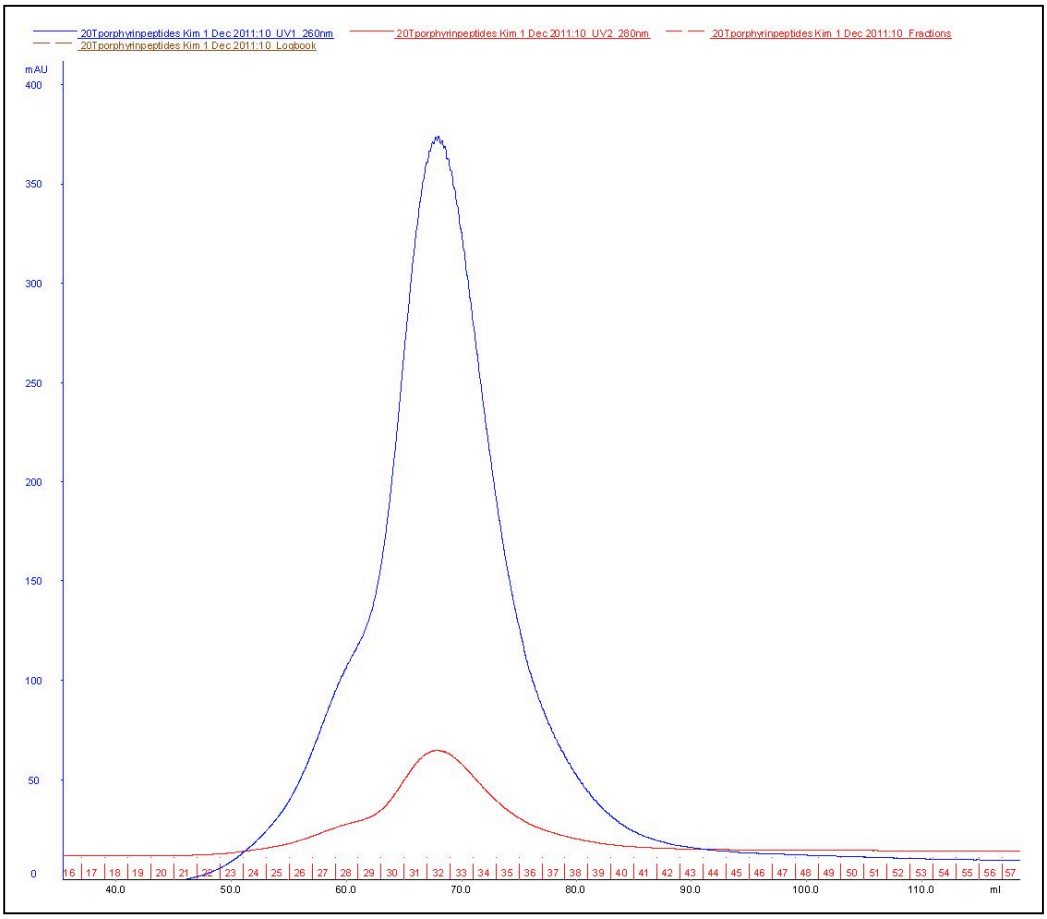

Figure 5.33 Size-exclusion chromatogram of 20T-peptide conjugate purification before the addition of porphyrin. A260 is shown in blue, and A280 is shown in red.

UV-Vis Spectroscopy of Peptide-Bound and Unbound Porphyrin and Binding Affinity of Bis-Histidine Coordinated Porphyrin

Tests were conducted to ensure that the terminal histidine residue of the peptide bound to the porphyrin's Fe(III) center. Bis-histidine coordination of Fe(III)-containing porphyrins is investigated in the literature [71,72,73]. A ~8 nm hyperchromic red shift in the Soret region occurs upon bis-histidine coordination of the porphyrin. A similar Soret shift in was observed when our P8 peptide was mixed with our Fe(III)-TPPS4 porphyrin in solution. Additionally, our spectra showed two Q bands in the 500-600 nm region in its unbound form. Upon binding to His residues of the peptides, only one slightly blue-shifted Q band is observed. Titrations revealed that a maximum binding occurred when 3 equivalents of peptide were added to the porphyrin. Calculations for the dissociation constant for the complexation of the bis-His-Fe(III) resulted in Kd1 = 2 μM, and Kd2 = 40 μM. The first dissociation constant refers to the first complexation event in which one histidine is bound to the Fe(III). These Kd values were obtained by plotting A416 (approximate Soret maximum for all bis-His-Fe(III) species) against the concentration of the ligand (peptide), and using a log plot to obtain the values, as described in [74]. More detailed calculations are currently in preparation.

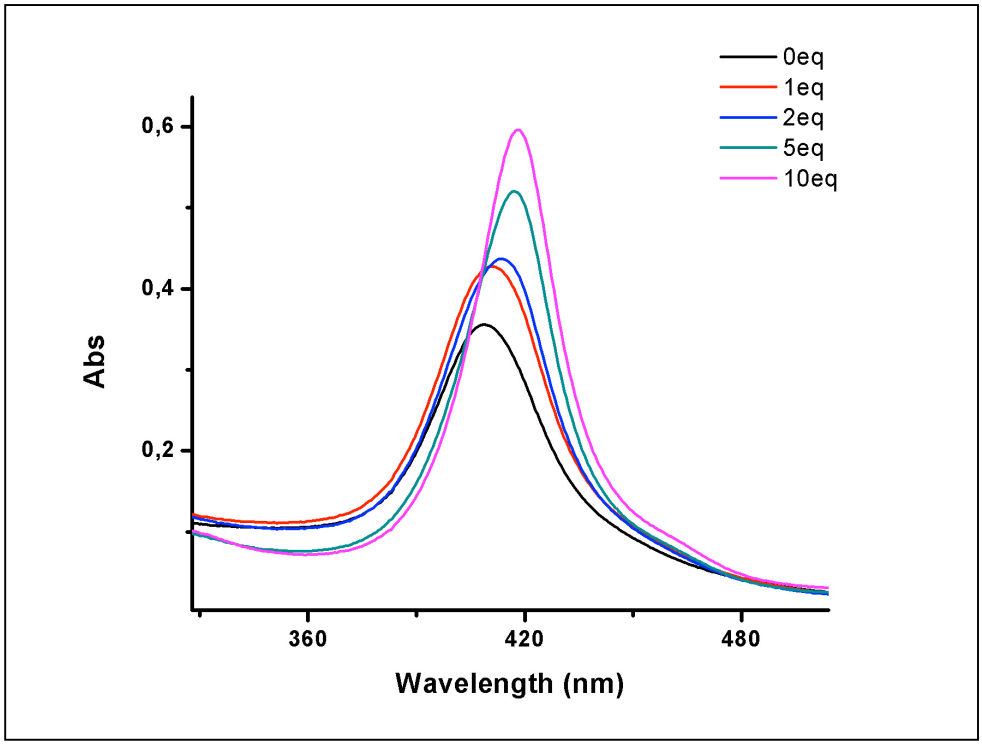

Figure 5.34. Hyperchromic red shifts associated with increasing concentrations of peptide (ligand) for the porphyrin. Unbound Fe(III) porphyrin exhibits a Soret peak at 408 nm while bis-histidine coordinated Fe(III) exhibits a 416 nm peak. The legend indicates the molar ratio at which ligand (peptide) was added. 1eq means 1 molar equivalent of peptide compared to the porphyrin (in these spectra, 5 μM was always the concentration of porphyrin).

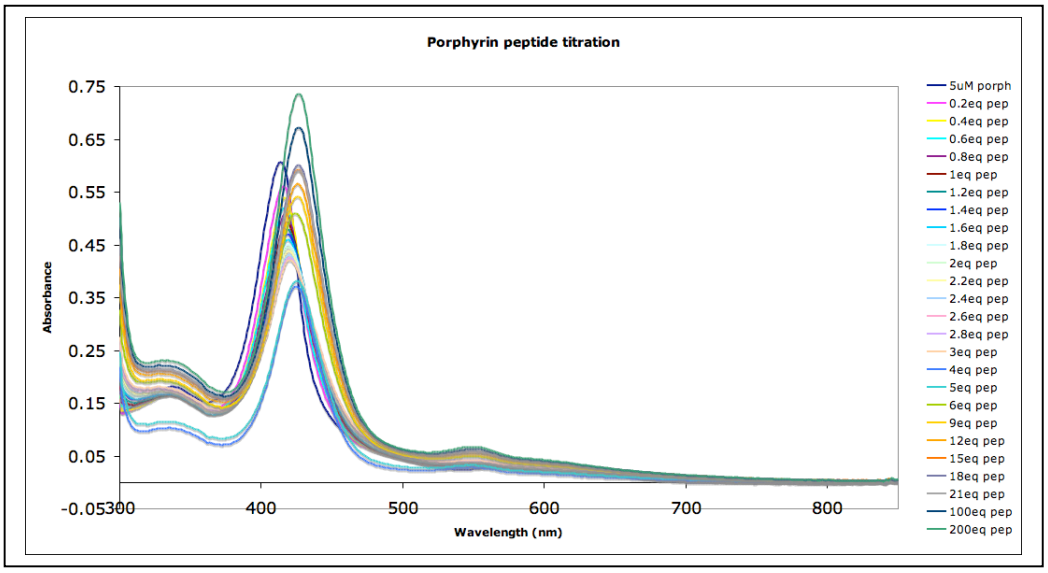

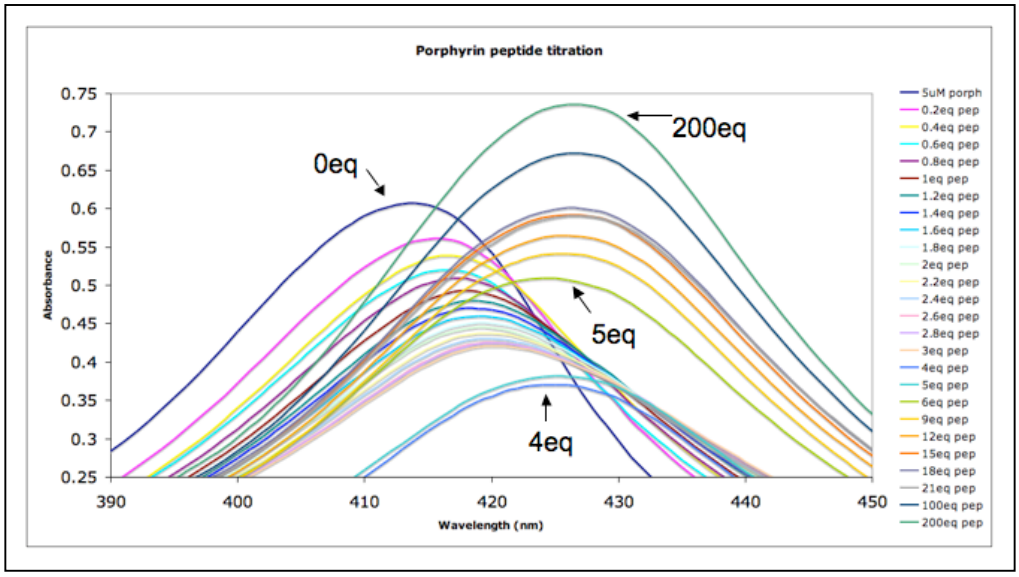

Figure 5.35. Titration of porphyrin with different equivalents of peptide—an observable decrease in absorption is accompanied by a shift, indicative of pentacoordinated species, until approximately 6 equivalents of peptide, at which the shift again becomes hyperchromic, likely indicating the formation of hexacoordinated species. These absorbance values at 416 nm were used for the plot to calculate the dissociation constant for this reaction.

EPR to investigate spin state of iron

EPR has been used extensively to study metalloproteins, or proteins containing cofactors with central metals. Hemes or porphyrins are cofactors in many biological systems. Most of the work done on iron-containing porphyrins revolves around heme cofactors in both hemoglobin/myoglobin and cytochromes [75]. EPR is a very powerful technique when working with coordination of transition metals. In this work, iron is the transition metal studied. The high-spin ferric iron is EPR active, possessing unpaired electrons, and low-spin iron can be observed upon bis-histidine coordination [76]. The nature of the iron coordination and the spin state of ferric heme complexes was examined earlier in de novo-designed heme proteins. [73] The transition of the free porphyrin to the porphyrin with bis-histidine coordinated iron(III) can be detected by EPR. Both high-spin and low-spin iron(III) possess specific g values as described in [75]. High-spin iron(III) has a value of g = 6.2, whereas low-spin bis-histidine-coordinated iron(III) has g values of approximately 3.03, 2.23, and 1.43. The reason for this is that the axially coordinated ligands cause the iron(III) to become low-spin.

EPR of peptide-bound porphyrin and unbound porphyrin

Given that the spin state of the Fe(III) species changes upon this coordination, we measured EPR spectra of the unbound porphyrin and collected EPR spectra of the bound porphyrin with different concentrations of peptide. Many tests were conducted with different concentrations of ligand, which in these experiments, is the peptide. In Figure 5.36, CW EPR spectra of free porphyrin and

3 titrations of porphyrin and peptide are shown. The black line represents unbound porphyrin at a concentration of 1 mM, red line is 1 mM porphyrin : 1 mM peptide, green line is 0.5 mM porphyrin : 1 mM peptide, blue line is 1 mM porphyrin : 0.5 mM peptide. The ideal range for binding was found to be a stoichoimetric ratio of 1 porphyrin : 2 peptides, as expected for this coordination of the Fe(III) of the porphyrin. The results revealed the optimal peptide:porphyrin stoichiometric ratio that induced the low-spin species to form. High-spin Fe(III) is easily detectable in the EPR measurements by the characteristic line at g = 6.2, while low-spin Fe(III) formation is detected by its lines at g = 2.93, 2.2, and 1.57. The addition of the peptide immediately resulted in a presence of low-spin species, indicating that the Fe(III) adopted its octahedral conformation upon binding of the two histidine nitrogens. The best yield for the low-spin Fe(III) resulted at a 1:2 stoichoimetric ratio of porphyrin to peptide. (See Figure 5.36) The transition to the low-spin Fe(III) clearly indicates that two histidines are coordinate to the iron. We hypothesize that the black line represents 100% unbound porphyrin, the blue line is 75% unbound and 25% bound, the red line is 50% unbound and 50% bound, and the green line is 100% bound. The green line showing the 1:2 stoichiometric ratio of porphyrin to peptide is proof that this species is entirely hexacoordinated (two axial histidines are coordinated to the Fe(III) of the porphyrin).

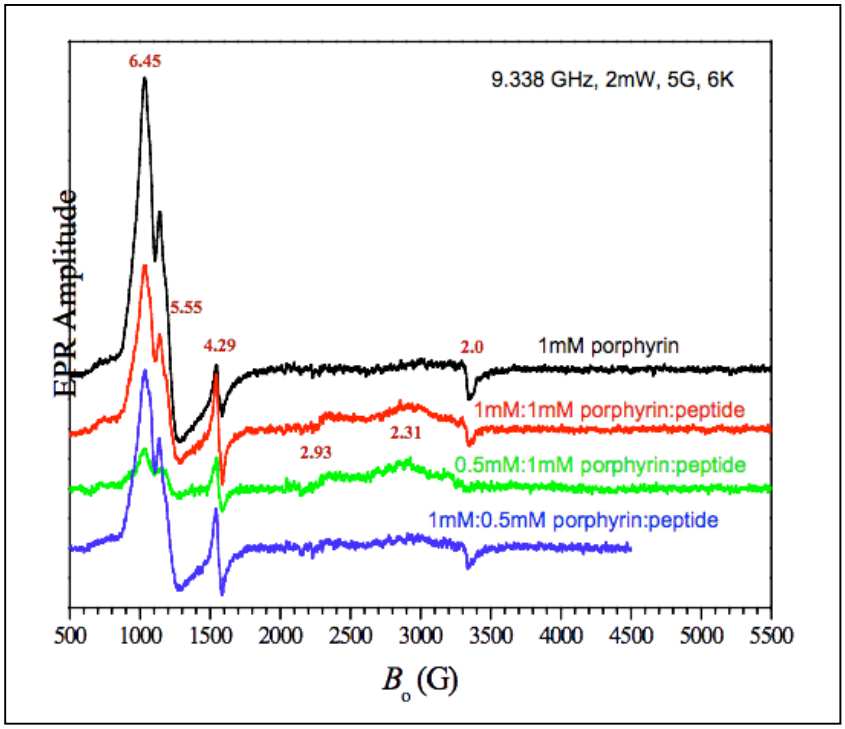

Figure 5.36. Porphyrin-peptide titrations and associated EPR spectra. A noticeable change from high-spin to low-spin occurs upon a 1:2 stoichiometric ratio of porphyrin:peptide.

The influence of EDTA in Fe(III) porphyrin EPR and UV-Vis measurements

We speculated that in the EPR measurements shown in Figure 5.36, an iron chloride contaminant in the sample was causing a line to appear in all of the spectra at g = 4.5 that was undesirable. It is likely that the EDTA chelated trace amounts of free iron contaminants, causing the line to appear. Therefore, in another experiment, the influence of EDTA in the buffer system on the EPR spectra was investigated. In Figure 5.37, CW EPR spectra of unbound porphyrin and 4 titrations of porphyrin and peptide, with EDTA in the buffer, are shown.

The black line represents unbound porphyrin at a concentration of 0.5 mM, red line is 0.5 mM porphyrin : 0.5 mM peptide, green line is 0.5 mM porphyrin : 1 mM peptide, blue line is 0.5 mM porphyrin : 2.5 mM peptide, and light blue line is 0.5 mM porphyrin : 5 mM peptide. The ideal range for binding was found to be a stoichoimetric ratio of 1 porphyrin : 2 peptides. In the EPR spectra of the peptide-porphyrin where EDTA was present, a strong line at g = 4.5 indicated a $FeCl_2$ contaminant. Once EDTA was eliminated from the sample, that contaminant disappeared. Thus, EDTA was not necessary to include in the sample as there was no need to chelate the excess magnesium acetate (source of divalent cations for when DNA is in the sample) in the buffer when working with the peptide and porphyrin only. UV-Vis measurements revealed no difference in the spectra when EDTA was present or absent in the buffer. The typical hyperchromic red shift is observed when the peptide is added to the sample. Additionally, two Q bands are present in the free porphyrin sample, and when the peptide is added, only one Q band is observed. No apparent difference in the UV-Vis spectra existed between the samples in buffer with EDTA and without EDTA, as shown in Figure 5.38.

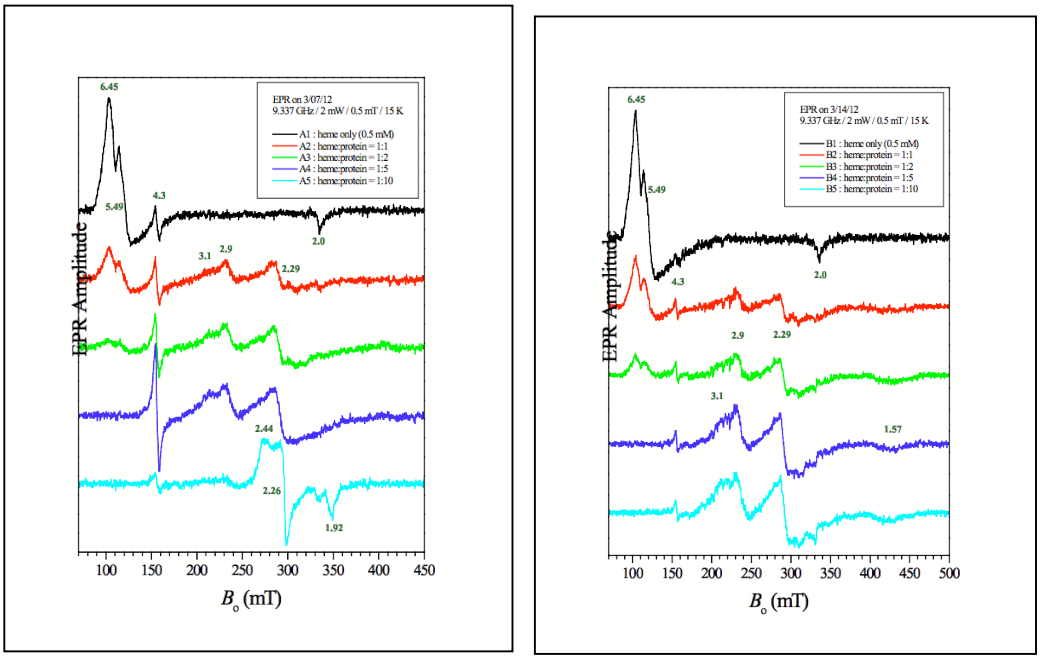

Figure 5.37. EPR of porphyrin and peptide with (left) and without EDTA (right). The iron contaminant at g = 4.5 is decreased when EDTA is not in the buffer (right).

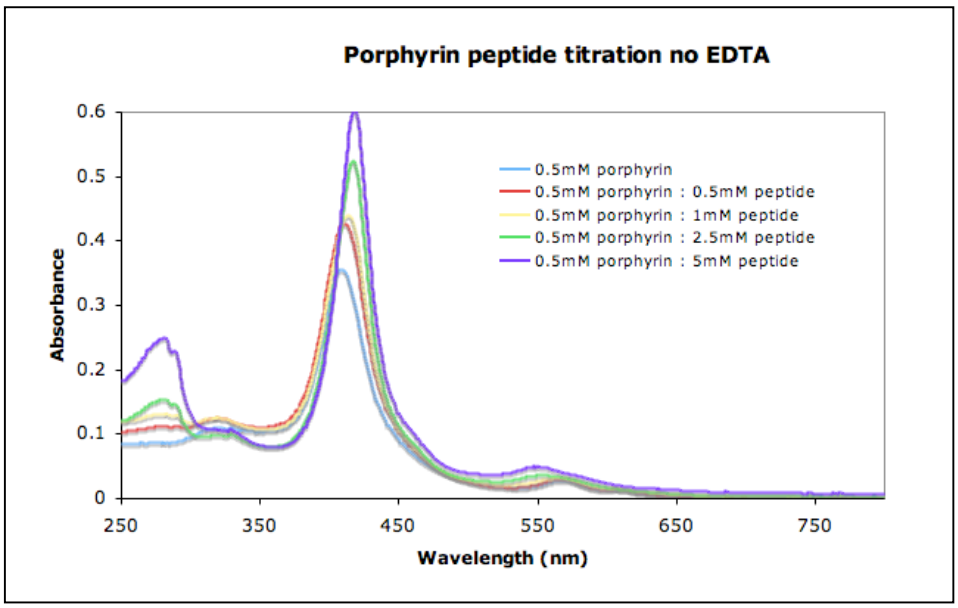

Figure 5.38. UV-Vis measurements of the porphyrin and peptide without EDTA in the buffer. These results look nearly identical to the results presented in Figure 5.33 earlier where EDTA was in the buffer. The presence or absence of EDTA does not affect the UV-Vis measurements.

Assembly of the 20TP8P complex using Scheme 1

The initial assembly strategy for the incorporation of the porphyrin involved using Scheme 1, in which the 20TP complex was assembled and purified first, and then porphyrin was added. This strategy seemed most promising as it effectively removed all of the higher molecular weight aggregates and other contaminants in the SEC step before the porphyrin was added.

Verification of Internal Assembly of the Porphyrin – DLS and native gel electrophoresis

We explored many different ways of validation that the porphyrin was internally assembled inside of the DNA cage, and to exclude the possibility that the Fe would be coordinated by inter-20T coordinating that would cause the formation of dimers. Native gel electrophoresis (gel mobility assay) and DLS are reliable methods to confirm assembly and detect dimers. If multimers of tetrahedra formed, they would appear on a gel. Figure 5.40 shows that binding of the porphyrin does not lead to the formation of dimers or higher molecular weight aggregates. The native gel in Figure 5.40 shows that the 20T-peptide construct was successfully purified through size-exclusion chromatography, and that only few aggregates are present in the sample. Upon addition of the porphyrin to the sample, no aggregation occurs, indicating that intercoordination of the two histidines with the Fe(III) is likely occurring inside the cage, rather than intercoordination to other tetrahedra. Additionally, in such a dilute sample, intercoordination would be unlikely. Since no size change of the 20T-peptide construct occurs when the porphyrin is added to solution, the peptides cooperatively assemble with the aid of the Fe(III) porphyrin inside of the cage. Additionally, DLS can be used to analyze polydispersity of a sample. In Figure 5.39, the DLS distribution revealed a mostly monomeric sample with little aggregation. It was important that in the two DLS distributions, the aggregation state did not change when the porphyrin was added (bottom part of the figure), also indicating that internal assembly occurred.

The sizes of the peptides and porphyrin used in this work are feasible with the cavity size of the tetrahedron (approximately 7 nm diameter). The peptides are each 2.4 nm in length assuming that they do not form secondary structure elements, and the porphyrin's diameter across the planar ring is approximately 1.5 nm. However, due to the nature of the axial bis-histidine coordination of the metal, the planar ring diameter of the porphyrin will likely be oriented perpendicular to the length of the peptide. Additionally, the iron(III)-TPPS4 porphyrin was used for these studies not only due to its water-soluble properties, but because of its negatively-charged sulfonato groups. The negative charges prevent electrostatic interactions from occurring between the negatively charged phosphate backbone of the DNA and the porphyrin side groups. The metal also aids in preventing undesired intercalation between the bases of the DNA because without histidine ligands, it can axially bind water molecules and thus avoid being planar enough to intercalate in the DNA. [77] Native gel electrophoresis and DLS experiments verified that no larger conformational changes of the 20T tetrahedron resulted following iron(III)-TPPS4 addition.

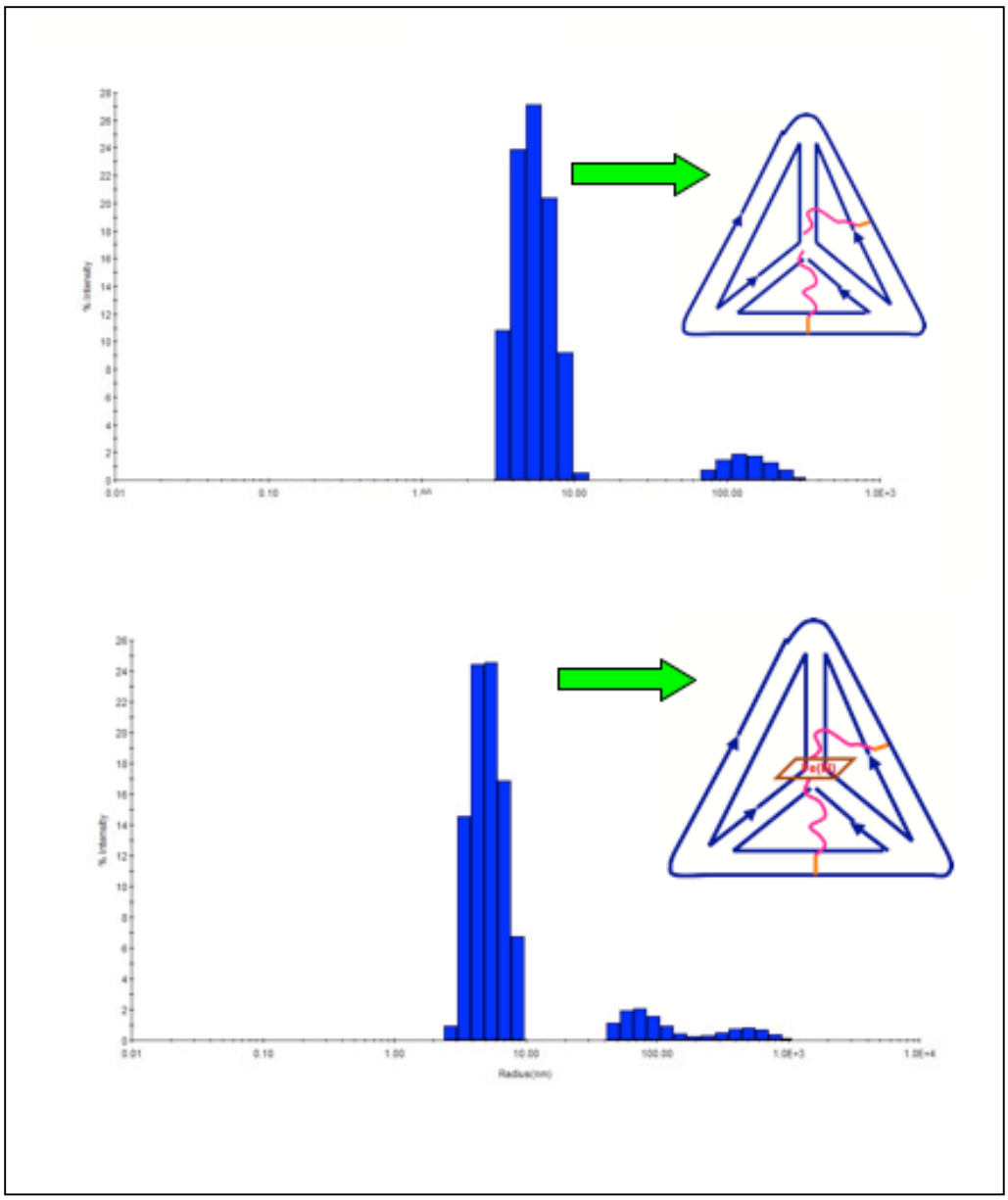

Figure 5.39. DLS measurements of the 20T-peptide and 20T-peptide-porphyrin complex each at a concentration of 10 μM of 20T-peptide and for the porphyrin sample, 5 μM porphyrin. The samples appear homogeneous, with very little aggregates.

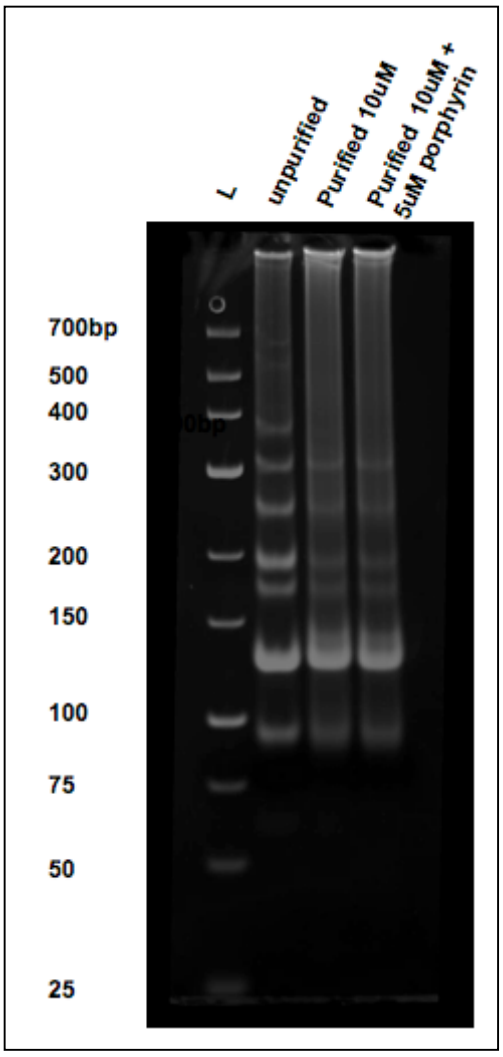

Figure 5.40. 5% native gel electrophoresis comparing unpurified tetrahedron, purified tetrahedron-peptide, and purified tetrahedron-peptide-porphyrin, in order to test for the formation of aggregates during the porphyrin assembly. Lane "L" is 10 µL of a low-molecular weight dsDNA ladder. For each of the other lanes, 18 µL of sample was mixed with 2 µL of 10X native tracking dye (outlined in more detail in Materials and Methods). The native gel verifies the successful assembly of a porphyrin inside of the 20T tetrahedron. Since no size change of the 20T-peptide construct occurs when the porphyrin is added to solution, the peptides cooperatively assemble with the aid of the Fe(III) porphyrin inside of the cage. The monomeric 20TP (20T-peptides) is shown in the band between 100-150bp on the lane labeled "Purified 10µM". The monomeric 20T8P (20T-peptide-porphyrin) is in the band between 100-150bp on the lane labeled "Purified 10µM+5µM porphyrin".

Challenges obtaining high concentration of sample

Due to the modifications of one of the DNA strands in the porphyrin experiments, the yield of the entire preparation is typically no higher than 50 μM at a volume of ~150 μL. It is quite difficult to work with a sample of this quantity due to the fact that most EPR measurements require a sample concentration at 100 μM or more and a volume of ~100 μL for X-band EPR. Scaling up the prep to anneal at a low concentration of 50 nM to minimize aggregates would not work with Scheme 2 (coupling porphyrin first), because this concentration is well below the experimental binding constant of 2 μM for the porphyrin-histidine coordination. Diluting the sample for annealing, as it is typically done for the 20T tetrahedron with no modifications, would cause the dissociation of the porphyrin from the ssDNA-peptide.

EPR spectra of the fully-assembled tetrahedron-peptide-porphyrin complex

In the EPR measurements with the peptide and porphyrin, a concentration in the 0.5-1 mM range was easily achievable (and clear EPR spectra are shown in Figures 5.36-5.37 with the concentration of unbound porphyrin remaining at 0.5 mM for all of the tests. This is because there is significantly more material produced in a porphyrin or peptide synthesis than in a DNA purification. Therefore, due to the limitation in the concentration of the tetrahedron preparation, it was not possible to prepare a concentration ≥ 0.5 mM as in the

peptide-porphyrin measurements. Therefore, in Figure 5.41, the EPR spectra shows samples that contained only 5 μM of porphyrin for all the tests. For the EPR spectra of the 20T-peptide porphyrin sample the concentration is thereby 100 times lower than the concentrations shown in the previous EPR spectra of porphyrin-peptide shown in Figures 5.36-5.37. It is very convincing that, despite the low concentration which lowers the signal-to-noise ratio, the CW EPR spectra shown in Figure 5.41 indicate g values at 6.4 matching those shown in the EPR spectra of the peptide and porphyrin. Therefore, the spectroscopic evidence suggests that the peptides are oriented inside of the tetrahedron and the terminal histidine residues are coordinating the Fe(III), causing the transition from high-spin to low-spin Fe(III). Additionally, it is very exciting that the transition from high-spin to low-spin is even more pronounced when the peptides are incorporated inside the cage (green line in Figure 5.41) than when the same concentration of free peptides was added to the porphyrin. This indicates that both peptides are inside of the cage thereby providing the optimal coordination environment for the porphyrin.

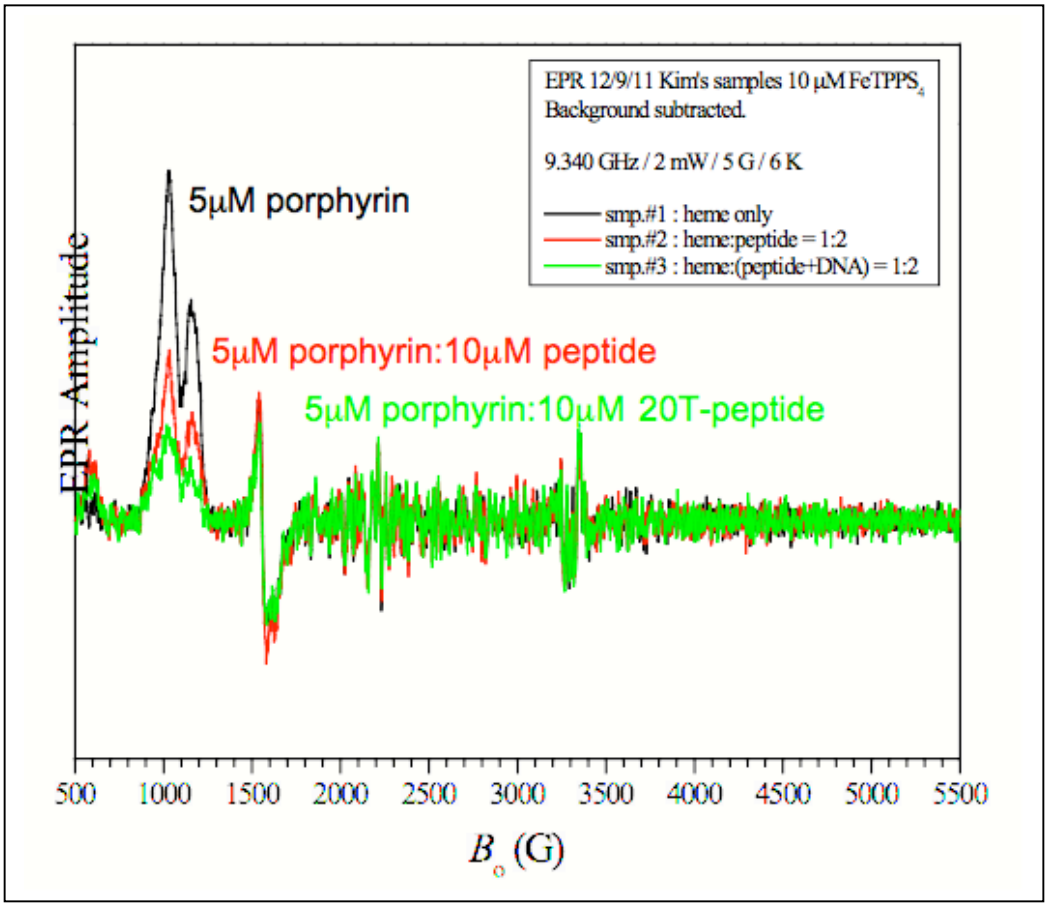

Figure 5.41. EPR measurements of the fully-assembled tetrahedron-porphyrin complex, at 100X lower concentration than the previous measurements of the porphyrin-peptide.

EPR measurements and optimization for low concentration of tetrahedron-peptide-porphyrin complex

Because of the obstacles associated with obtaining a high concentration of sample of the tetrahedron, the experimental parameters included varying the power applied to see if clearer spectra could be observed. The concentration of

tetrahedron-peptide was 10 μM and the porphyrin was 5 μM for these experiments. Some of the lines at g = 3.03, 2.23, and 1.43 values were difficult to detect on the spectrum. Future experimental plans include scale-up of the preparation in order to improve the spectral resolution.

UV-Vis measurements of 20TP8P assembled using Scheme 1

As another proof of concept that the porphyrin was incorporated into the cage, the characteristic Soret shift was analyzed. As shown in Figure 5.42 below, the Soret shift was undetectable (only shifted ~1 nm) after assembling using Scheme 1, which involved assembling the 20TP first and then adding porphyrin. Although we initially thought that Scheme 1 would work, we realized that the optical spectroscopy was not detecting the incorporation properly.

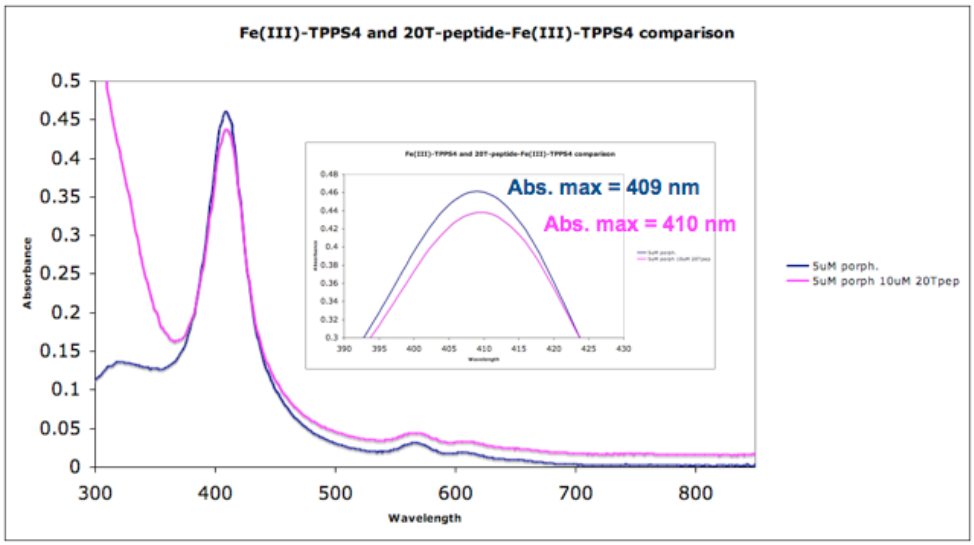

Figure 5.42. 20TP8P sample after annealing and assembling the complex according to Scheme 1 and then adding porphyrin. As seen, the Soret shift is barely visible as it is only red-shifted 1 nm.

Alternative strategy for porphyrin incorporation

What is interesting to note is that initially the strategy for incorporating the porphyrin into the center of the tetrahedron was to introduce porphyrin into solution with the tetrahedron. In the course of this work, after the tetrahedron-peptide complex was preassembled, it was discovered that the negatively-charged sulfonato groups are repulsed by the negatively-charged phosphate backbone of the DNA so that no porphyrin binding to the pre-assembled 20T tetrahedron can be observed. In this respect, the sulfonato groups help with preventing electrostatic interactions but they hindered the incorporation process after assembly of the 20TP complex. Therefore, a different technique was employed which involved coupling the porphyrin to the ssDNA-peptide conjugate first, and then annealing the other three strands of DNA to form the tetrahedron. This yielded not only a strong 8 nm Soret shift, as shown in Figure 5.42, but native gel electrophoresis also confirmed that the tetrahedron structure was formed. The annealing step consisted of 5-10 μM (rather than 50 nM as in the empty tetrahedron) and a small volume of ~50 μL (contrary to the ~450 mL annealing volume for the empty tetrahedron). These small volumes and higher concentrations were used to avoid overly diluting the sample and working below the Kd value for the reaction. Initially, the heating temperature of 70ºC was used to avoid damaging the porphyrin metal coordination. As shown in the native gel ,because of the lower annealing temperature and higher concentration, larger amounts of aggregates of tetrahedra occurred, as expected. Later, the experiment was performed using the same conditions except 90°C annealing took place and

we discovered that no damage to the coordination occurred. In this case, native gel electrophoresis verified that less aggregates formed than with the 70°C annealing. The experiments shown with both the 70°C annealing and the 90°C annealing are shown below.

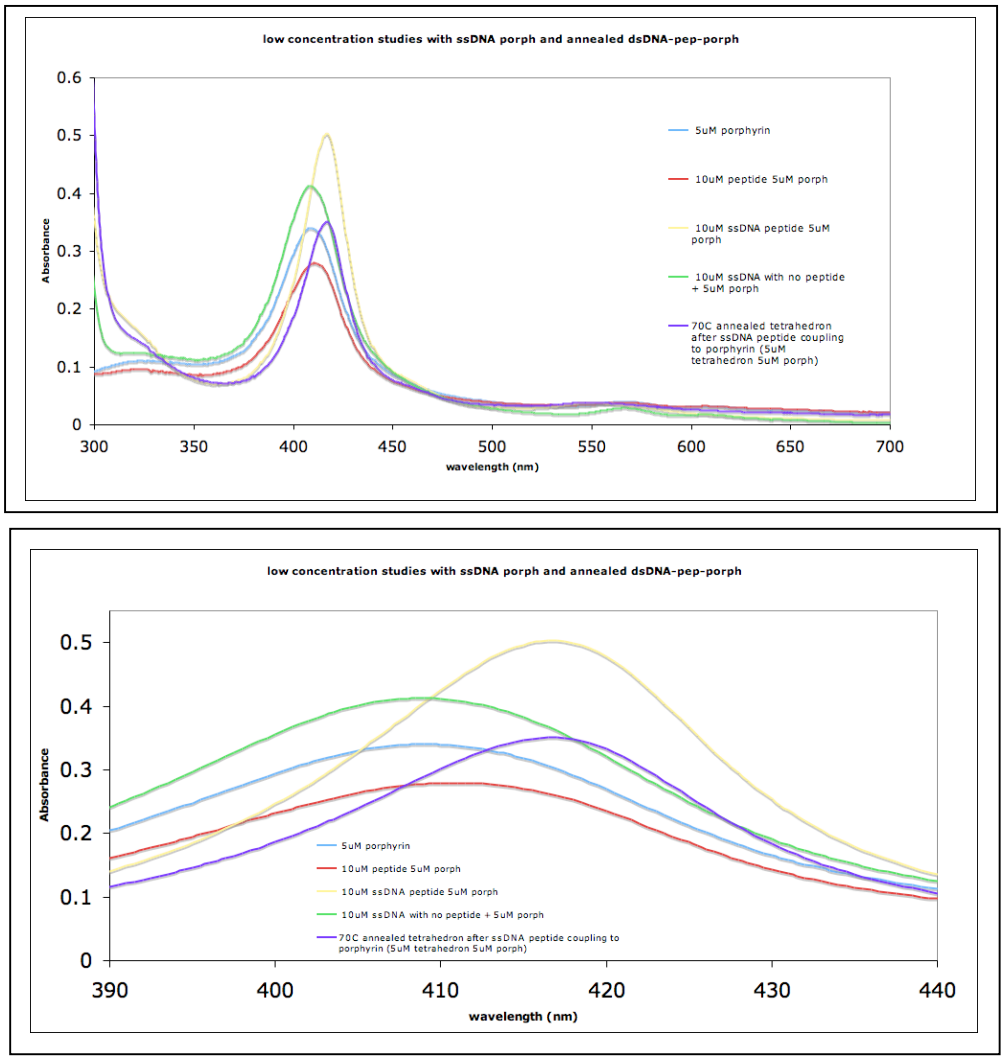

Figure 5.43. UV-Vis results after implementing Scheme 2 for the assembly of the 20TP8P complex. The initial concern was that annealing temperatures of 90°C may damage the porphyrin coordination. Therefore, the annealing temperature used in these experiments was 70°C. The blue line is 5μM unbound porphyrin, the red line is 5μM porphyrin + 10 μM peptide, the yellow line is 5 μM porphyrin + 10 μM ssDNA-peptide conjugate, and the green line is 5 μM porphyrin + 10 μM ssDNA with no peptides attached (as a control), and the purple line is 5 μM porphyrin + 10 μM of the 20TP8 complex after heating to 70°C for 10 minutes and cooling to room temperature. The results reveal that following annealing, Scheme 2 seems to provide the best route for assembling the 20TP8P complex, as the ssDNA-peptide is mixed with the porphyrin first, and the other strands are added. This procedure is done in a smaller volume but a higher concentration. The bottom spectra are a zoomed region showing the Soret shift.

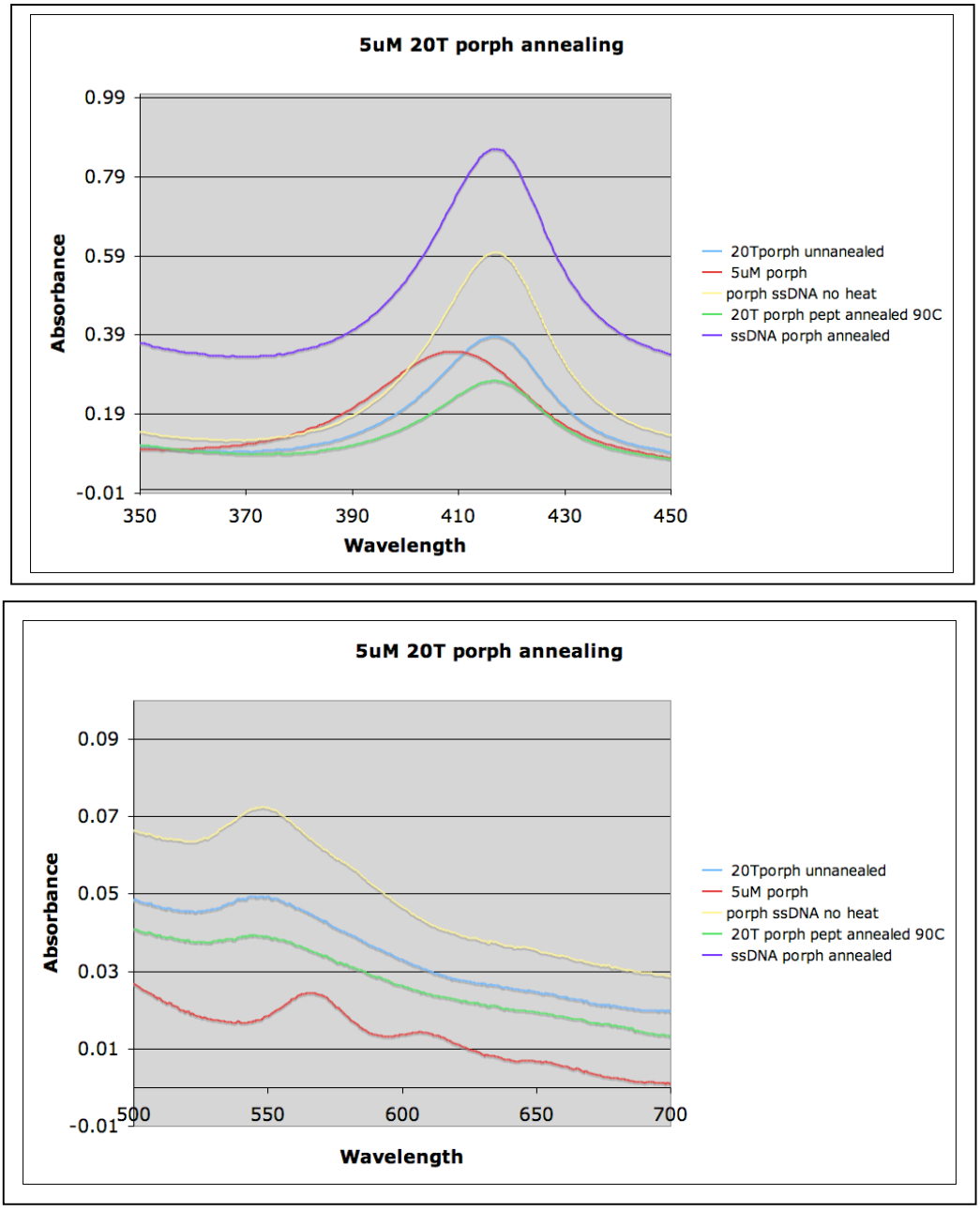

Figure 5.44. After coupling the ssDNA to the porphyrin and then annealing using Scheme 2, the shift is observed. Soret shift is shown at the top, and Q band transitions at bottom. The yellow line is the ssDNA-peptide conjugate + 5 μM porphyrin before being mixed with the other strands and annealed at 90C, the blue line represents the assembled 20TP8P complex before heating (5 μM porphyrin + 10 μM 20TP8), the red line is 5 μM of unbound porphyrin, the purple line is the ssDNA-peptide econjugate after annealing at 90°C (as a positive control), and the

green line is the entire 20TP8P complex after annealing at 90°C for 10 minutes and cooling to room temperature. These spectra indicate that the porphyrin coordination is not damaged by the 90°C temperature used for annealing.

Although the Soret peak was visible in these UV-Vis experiments shown above, there was not a proper method established to separate aggregation products from the monomeric sample. This was especially of concern because in Scheme 2, the sample was annealed at a higher concentration than in Scheme 1, which typically resulted in more aggregation. A filtration method was established to first pass the annealed crude sample through a 30 kDa MWCO filter by centrifuging for 30 minutes at 13,000 rpm. The sample that remained on the top was applied to a 100kDa filter and centrifuged for 30 minutes at 13,000 rpm. The filtrate was removed and analyzed for a Soret peak. The top of the 30kDa MWCO filter is shown in Figure 5.45 which clearly shows that the reddish color is more intense at the top of the filter compared to the bottom (which contains unbound porphyrin and fragments). Additionally, a strong Soret shift is shown in Figure 5.46. The native gel also shows the fractions used in the filtration experiments.

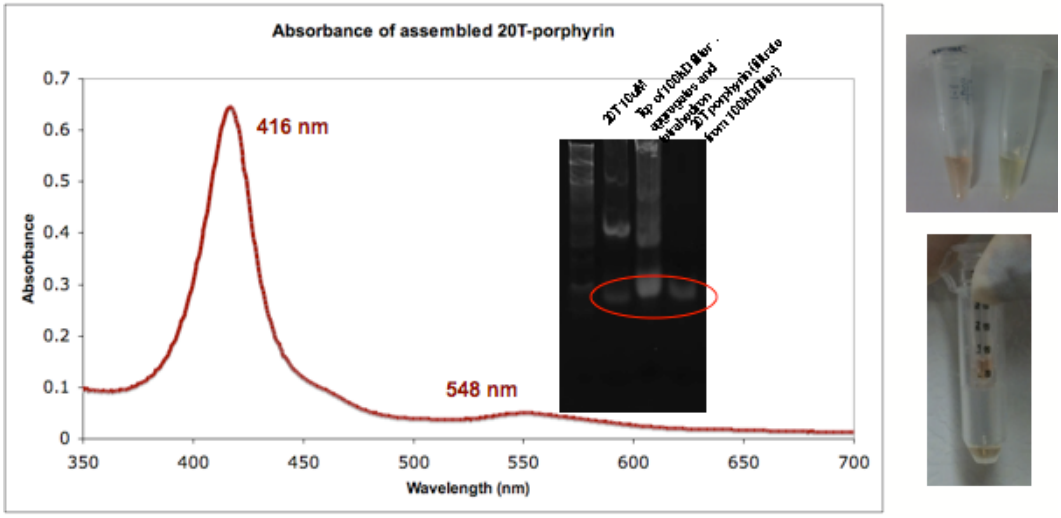

Figure 5.45. Soret and Q band peaks of the isolated monomeric 20TP8P sample. The red circle of the native gel shows the monomeric tetrahedron isolated from all aggregates (the band on the far right). Some monomeric tetrahedron still remains in the top of the 100kDa filter, as shown in the lane second from the right. The Soret peak shown in the graph is of the monomeric tetrahedron only (corresponds to the lane in the gel). The color change at the photo at the top right shows unbound porphyrin which appears greener in color than the 20TP8P sample on the left, which is visibly reddish. The filter on the bottom right is after centrifuging the sample in the 30kDa MWCO filter during the first filtration step. The sample remaining in the top of that filter was placed into the top of a 100kDa MWCO filter for the next step.

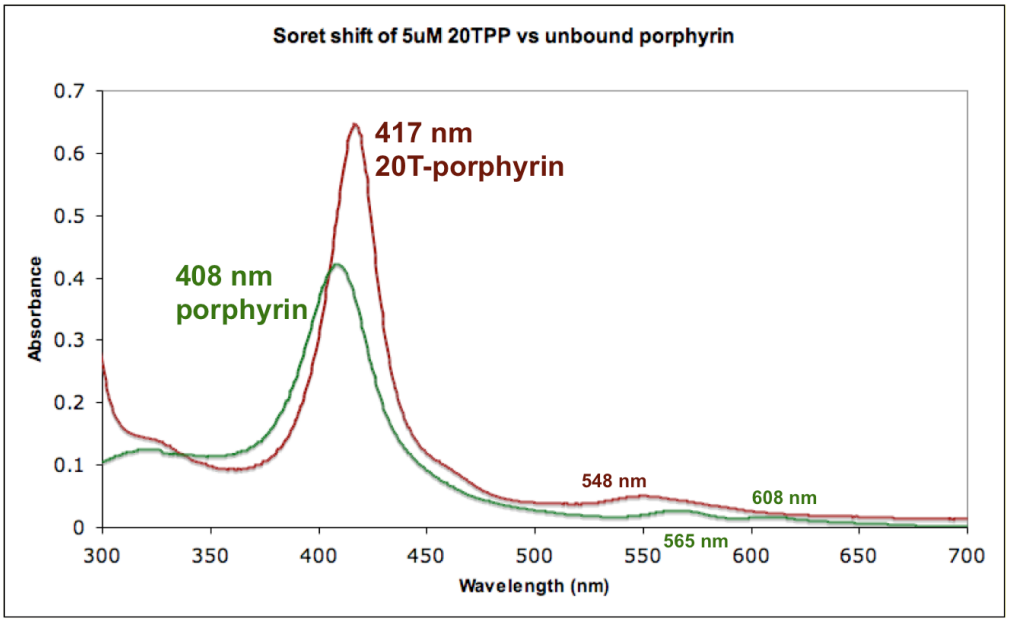

Figure 5.46. A comparison of unbound porphyrin at a concentration of 5 μM to the fully assembled, isolated monomeric 20TP8P at a concentration of 10 μM 20TP8 + 5 μM porphyrin. The Soret shift and the Q band transitions are clear in these spectra, which indicate that the internal coordination of the porphyrin is occurring.

UV-Vis results of fully-assembled 20TP8P complex and challenges observing Soret shift

As previously mentioned, the first method of porphyrin incorporation involved adding the porphyrin after the entire tetrahedron-peptide complex was annealed, purified, and concentrated. This resulted in no observable Soret shift, indicating that the porphyrin was not binding adequately inside of the cage. (See Figure 5.42). If any porphryin did successfully become incorporated inside of the cage, there was not enough incorporation to notice a Soret shift. (Other methods

had previously detected this incorporation such as EPR). An alternative strategy (Scheme 2) was used where the porphyrin was first coupled to the ssDNA-peptide and then annealed in a higher concentration and small volume. Under these conditions, a shift was observed, from 408 to 417 nm. This hyperchromic Soret shift detects the formation of the bis-histidine hexacoordinated species. (A pentacoordinated species would result in a red-shift but a decreased peak intensity.) Figures 5.45-5.46 above clearly illustrate the feasibility of Scheme 2 compared to Scheme 1.

Crystallization of fully-assembled complex

Crystallization trials of the fully-assembled tetrahedron-peptide-porphyrin complex were conducted. The conditions used were the same as for the 20T tetrahedron – 20T Fine Screen 4 was used. Crystals grew in approximately 2 days. Figure 5.47 shows some images of the crystals.

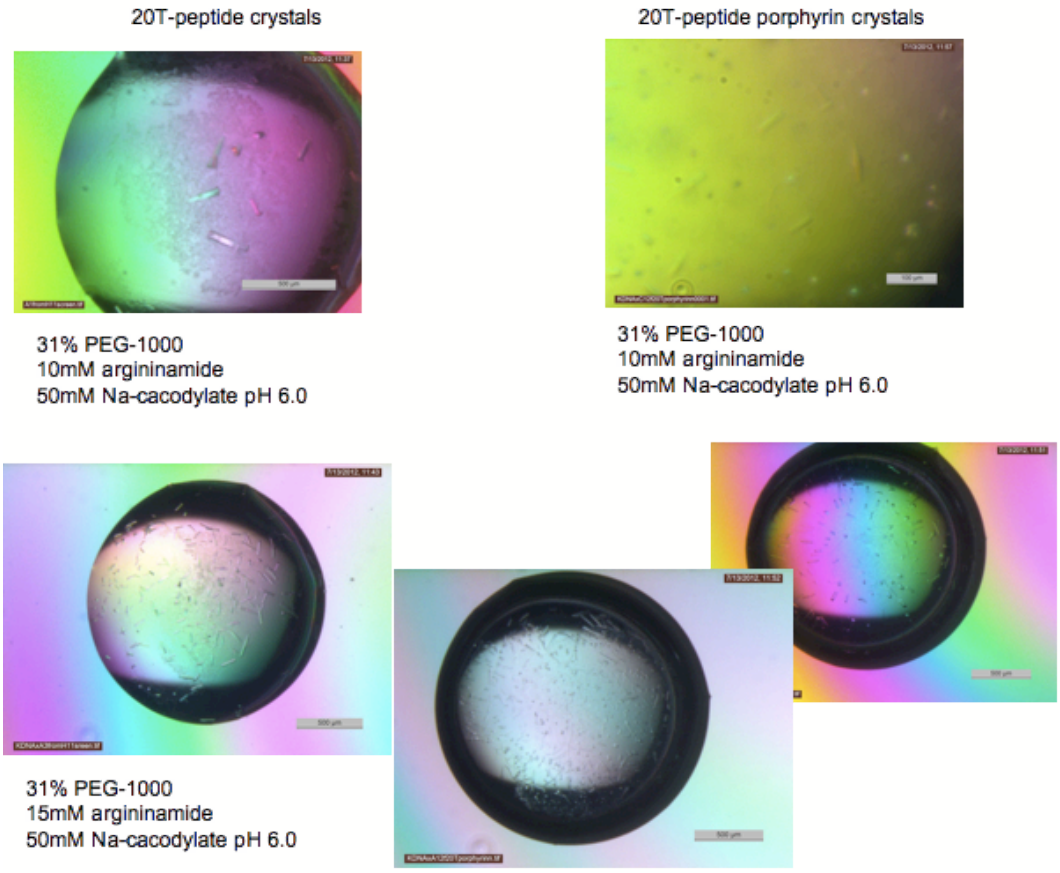

Figure 5.47. Crystals of the 20T-peptide and 20T-peptide-porphyrin structures. Crystals grew in approximately 3 days.

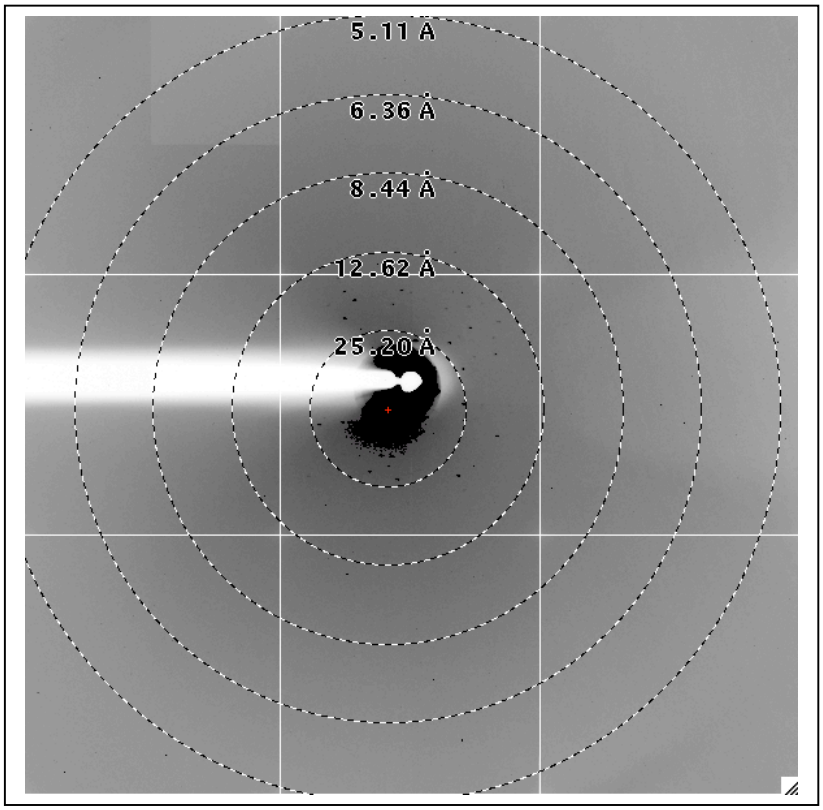

Figure 5.48. Single diffraction pattern of 20T-peptide-porphyrin crystals. These crystals are more tolerant to longer x-ray exposure times than the tetrahedron crystals.

6. CONCLUSION AND OUTLOOK

In this work, the conjugation of the tetrahedron with internally assembled peptides and porphyrins has been achieved. The same design could be applied in future constructs using the peptides based on PSII and assembly of the metal cluster. This requires the synthesis of the remaining two peptide sequences described in the proposed complex in Figure 2.3 and conjugating them to four additional sites within the tetrahedron. This would be very challenging as it would require use of up to five different coupling chemistries to be employed. An alternate strategy would employ the use of a cyclic peptide that would have all of the critical amino acids that provide ligands to the manganese cluster, and conjugate it to only one or two bases in the tetrahedron instead of the previously proposed five sites. This would drastically simplify the coupling challenge as only one conjugation to the tetrahedron would be necessary. The cyclic peptide design is currently underway.

In another strategy, PNA-peptides could be used to hybridize with the DNA (work of Justin Flory), which does not require chemical conjugation directly to the DNA. In this strategy, the PNA hybridizes to the DNA and the peptide is already co-synthesized with the PNA. This technique could be combined with the chemical conjugation strategy described in this work to incorporate all of the peptide sequences inside of the cage.

A different alternative strategy would include the use of high-valent manganese porphyrins as catalysts for water oxidation. This strategy is very interesting as it could use the same method developed in this work for the iron

porphyrins with the goal of observing water oxidation further down the road. In any case, the results described with iron porphyrin encapculation can be further used to facilitate the re-designing of the water oxidation complex in PSII. In order to improve the diffraction quality of the crystals, techniques may be used in the future to remove aggregates from solution that may hinder the formation of higher-quality crystals. Additionally, a stable single-stranded DNA design would have the potential to deliver promising results and could maybe be used as a template or as a film to organize redox-active proteins and photo-excitable pigments.

Lastly, other metals can be incorporated into the macrocycle of other porphyrins so that different spectroscopic techniques can be employed, such as fluorescence. Different metals can be selected based on their excited state lifetimes so other spectroscopy can be used. As a functional strategy for the Fe(III) porphyrins described in this work, a reducing agent such as dithionite or ascorbate can be added to see if the agent can migrate into the cage, reducing the Fe(III) to Fe(II). The Soret band and Q bands would verify this reduction of the iron.

Electrochemical techniques are also in the pipeline, as the ultimate goal is to show the complex's redox properties. A scale-up of the experiment is underway which would provide a concentrated sample for electrochemical measurements. Electrochemistry would also verify the oxidation state of the iron after reduction.

REFERENCES

1. Fromme P, Allen JP (2008) X-Ray Crystallography of Photosynthetic Proteins. In: Aartsma TJ, Matysik J, editors. Biophysical Techniques in Photosynthesis II: Springer. pp. 97-124.

2. Fromme P, Grotjohann I (2011) Structure of Cyanobacterial Photosystems I and II. In: Peschek GA, Obinger C, Renger G, editors. Bioenergetic Processes of Cyanobacteria: From Evolutionary Singularity to Ecological Diversity. Dordrecht: Springer.

3. Hohmann-Marriott MF, Blankenship RE (2011) Evolution of Photosynthesis. Annual Reviews in Plant Biology: 515-548.

4. Holland HD (2006) The Oxygenation of the Atmosphere and Oceans. Philosophical Transactions: Biological Sciences 361: 903-915.

5. Umena Y, Kawakami K, Shen J-R, Kamiya N (2011) Crystal structure of oxygen-evolving photosystem II at a resolution of 1.9 A. Nature: 1-7.

6. Zouni A, Witt H-T, Kern J, Fromme P, Kraus N, et al. (2001) Crystal structure of photosystem II from Synechococcus elongatus at 3.8 A resolution. Nature 409: 739-743.

7. Ferreira KN, Iverson TM, Maghlaoui K, Barber J, Iwata S (2004) Architecture of the Photosynthetic Oxygen-Evolving Center. Science 303: 1831-1838.

8. Loll B, Kern J, Saenger W, Zouni A, Biesiadka J (2005) Towards complete cofactor arrangement in the 3.0 A resolution structure of photosystem II. Nature 438: 1040-1044.

9. Yano J, Yachandra VK (2008) Where Water Is Oxidized to Dioxygen: Structure of the Photosynthetic Mn4Ca Cluster from X-ray Spectroscopy. Inorganic Chemistry 47: 1711-1726.

10. Luber S, Rivalta I, Umena Y, Kawakami K, Shen JR, et al. (2011) S-1-State Model of the O-2-Evolving Complex of Photosystem II. Biochemistry 50: 6308-6311.

11. Barber J, Ferreira K, Maghlaoui K, Iwata S (2004) Structural model of the oxygen-evolving centre of photosystem II with mechanistic implications. Physical Chemistry Chemical Physics 6: 4737-4742.

12. Rapatskiy L, Cox N, Savitsky A, Ames WM, Sander J, et al. (2012) Detection of the Water-Binding Sites of the Oxygen-Evolving Complex of

Photosystem II Using W-Band O-17 Electron-Electron Double Resonance-Detected NMR Spectroscopy. Journal of the American Chemical Society 134: 16619-16634.

13. Mukherjee S, Stull JA, Yano J, Stamatatos TC, Pringouri K, et al. (2012) Synthetic model of the asymmetric Mn3CaO4 cubane core of the oxygen-evolving complex of photosystem II. Proceedings of the National Academy of Sciences of the United States of America 109: 2257-2262.

14. Galstyan A, Robertazzi A, Knapp EW (2012) Oxygen-Evolving Mn Cluster in Photosystem II: The Protonation Pattern and Oxidation State in the High-Resolution Crystal Structure. Journal of the American Chemical Society 134: 7442-7449.

15. Smolentsev G, Soldatov AV, Messinger J, Merz K, Weyhermuller T, et al. (2009) X-ray Emission Spectroscopy To Study Ligand Valence Orbitals in Mn Coordination Complexes. Journal of the American Chemical Society 131: 13161-13167.

16. Pushkar YL, Yano J, Sauer K, Boussac A, Yachandra VK (2008) Structural changes in the Mn4Ca cluster and the mechanism of photosynthetic water splitting. Proceedings of the National Academy of Sciences of the United States of America 105: 1879-1884.

17. Yano J, Kern J, Sauer K, Latimer MJ, Pushkar Y, et al. (2006) Where water is oxidized to dioxygen: Structure of the photosynthetic Mn4Ca cluster. Science 314: 821-825.

18. Kok B, Forbush B, McGloin M (1970) COOPERATION OF CHARGES IN PHOTOSYNTHETIC O2 EVOLUTION .1. A LINEAR 4STEP MECHANISM. Photochemistry and Photobiology 11: 457-&.

19. Kok B (1957) ABSORPTION CHANGES INDUCED BY THE PHOTOCHEMICAL REACTION OF PHOTOSYNTHESIS. Nature 179: 583-584.

20. Vass I (2012) Molecular mechanisms of photodamage in the Photosystem II complex. Biochimica Et Biophysica Acta-Bioenergetics 1817: 209-217.

21. Baena-Gonzalez E, Aro E-M (2002) Biogenesis, Assembly and Turnover of Photosystem II Units. Philosophical Transactions: Biological Sciences 357: 1451-1460.

22. Liao D-I, Qian J, Chisholm DA, Jordan DB, Diner BA (2000) Crystal structures of the photosystem II D1 C-terminal processing protease. Nature 7: 749-753.

23. Franklin RE, Gosling RG (1954) THE ANALYSIS OF X-RAY FIBRE DIAGRAMS OF DNA AND THE DEPENDENCE OF STRUCTURE ON WATER CONTENT. Transactions of the Faraday Society 50: 298-299.

24. Jiang Q, Song C, Nangreave J, Liu XW, Lin L, et al. (2012) DNA Origami as a Carrier for Circumvention of Drug Resistance. Journal of the American Chemical Society 134: 13396-13403.

25. Liu CH, Kim E, Demple B, Seeman NC (2012) A DNA-Based Nanomechanical Device Used To Characterize the Distortion of DNA by Apo-SoxR Protein. Biochemistry 51: 937-943.

26. Yang Y, Han DR, Nangreave J, Liu Y, Yan H (2012) DNA Origami with Double-Stranded DNA As a Unified Scaffold. ACS Nano 6: 8209-8215.

27. Seeman NC (2010) Nanomaterials Based on DNA. In: Kornberg RD, Raetz CRH, Rothman JE, Thorner JW, editors. Annual Review of Biochemistry, Vol 79. Palo Alto: Annual Reviews. pp. 65-87.

28. Feldkamp U, Niemeyer CM (2006) Rational Design of DNA Nanoarchitectures. Angewandte Chemie International Edition: 1856-1876.

29. Goodman RP, Schaap AT, Tardin CF, Erben CM, Berry RM, et al. (2005) Rapid Chiral Assembly of Rigid DNA Building Blocks for Molecular Nanofabrication. Science 310: 1661-1665.

30. Zheng J, Birktoft JJ, Chen Y, Wang T, Sha R, et al. (2009) From molecular to macroscopic via the rational design of a self-assembled 3D DNA crystal. Nature 461: 74-77.

31. Kato T, Goodman RP, Erben CM, Turberfield AJ, Namba K (2009) High-Resolution Structural Analysis of a DNA Nanostructure by cryoEM. Nano Letters 9: 2747-2750.

32. Chhabra R, Sharma J, Wang HN, Zou SL, Lin S, et al. (2009) Distance-dependent interactions between gold nanoparticles and fluorescent molecules with DNA as tunable spacers. Nanotechnology 20.

33. Stearns LA, Chhabra R, Sharma J, Liu Y, Petuskey WT, et al. (2009) Template-Directed Nucleation and Growth of Inorganic Nanoparticles on

DNA Scaffolds. Angewandte Chemie-International Edition 48: 8494-8496.

34. Lu M, Guo Q, Seeman NC, Kallenbach NR (1990) DRUG-BINDING BY BRANCHED DNA - SELECTIVE INTERACTION OF THE DYE STAINS-ALL WITH AN IMMOBILE JUNCTION. Biochemistry 29: 3407-3412.

35. Lu N, Pei H, Ge ZL, Simmons CR, Yan H, et al. (2012) Charge Transport within a Three-Dimensional DNA Nanostructure Framework. Journal of the American Chemical Society 134: 13148-13151.

36. Erben CM, Goodman RP, Turberfield AJ (2006) Single-Molecule Protein Encapsulation in a Rigid DNA Cage. Angewandte Chemie: 7574-7577.

37. Liu WY, Zhong H, Wang RS, Seeman NC (2011) Crystalline Two-Dimensional DNA-Origami Arrays. Angewandte Chemie-International Edition 50: 264-267.

38. Simmons CR, Schmitt D, Wei X, Han D, Volosin AM, et al. (2011) Size-Selective Incorporation of DNA Nanocages into Nanoporous Antimony-Doped Tin Oxide Materials. ACS Nano 5: 6060-6068.

39. Wang T, Sha RJ, Birktoft J, Zheng JP, Mao CD, et al. (2010) A DNA Crystal Designed to Contain Two Molecules per Asymmetric Unit. Journal of the American Chemical Society 132: 15471-15473.

40. Seeman NC (2007) An Overview of Structural DNA Nanotechnology. Molecular Biotechnology 37: 246-257.

41. Hoegh-Guldberg O, Mumby PJ, Hooten AJ, Steneck RS, Greenfield P, et al. (2007) Coral reefs under rapid climate change and ocean acidification. Science 318: 1737-1742.

42. Schurr JM (1986) Dynamic Light Scattering Studies of Biopolymers: Effects of Charge, Shape, and Flexibility. Annual Reviews in Physical Chemistry 37: 271-305.

43. Chu B (1991) Laser Light Scattering: Basic Principles and Practice. Boston, USA: Academic Press.

44. (1993) Dynamic Light Scattering: the Method and Some Applications; Brown W, editor. New York, USA: Oxford Science Publications.

45. Dierks K, Meyer A, Einspahr H, Betzel C (2008) Dynamic Light Scattering in Protein Crystallization Droplets: Adaptations for Analysis and Optimization of Crystallization Processes. Crystal Growth and Design 8: 1628-1634.

46. Borgstahl GEO (2007) How to Use Dynamic Light Scattering to Improve the Likelihood of Growing Macromolecular Crystals. In: Doublie S, editor. Methods in Molecular Biology. Totowa, NJ: Humana Press, Inc. pp. 109-129.

47. Rupp B, Kantardjieff KA (2008) Macromolecular Crystallography. In: Walker JM, Rapley R, editors. Molecular Biomethods Handbook. Totowa, NJ: Humana Press. pp. 821-849.

48. Grant TD, Luft JR, Wolfley JR, Tsuruta H, Martel A, et al. (2011) Small Angle X-ray Scattering as a Complementary Tool for High-Throughput Structural Studies. Biopolymers 95: 517-530.

49. Fischetti RF, Rodi DJ, Mirza A, Irving TC, Kondrashkina E, et al. (2003) High-resolution wide-angle X-ray scattering of protein solutions: effect of beam dose on protein integrity. Journal of Synchrotron Radiation 10: 398-404.

50. Rhodes G (2006) Crystallography Made Crystal Clear. Oxford: Elsevier.

51. Chayen NE, Saridakis E (2008) Protein crystallization: from purified protein to diffraction-quality crystal. Nature Methods 5: 147-153.

52. Ravelli RBG, Garman EF (2006) Radiation damage in macromolecular cryocrystallography. Current Opinion in Structural Biology 16: 624-629.

53. Brown GE, Sutton SR, Calas G (2006) User facilities around the world. Elements 2: 9-14.

54. Sanishvili R, Nagarajan V, Yoder D, Becker M, Xu S, et al. (2008) A 7 um mini-beam improves diffraction data from
small or imperfect crystals of macromolecules. Acta Crystallographica Section D D64: 425-435.

55. Roat-Malone RM (2007) Bioinorganic Chemistry, A Short Course. Hoboken, New Jersey, USA: John Wiley & Sons, Inc.

56. Porra RJ, Thompson WA, Kriedemann PE (1989) DETERMINATION OF ACCURATE EXTINCTION COEFFICIENTS AND SIMULTANEOUS-EQUATIONS FOR ASSAYING CHLOROPHYLL-A AND

CHLOROPHYLL-B EXTRACTED WITH 4 DIFFERENT SOLVENTS - VERIFICATION OF THE CONCENTRATION OF CHLOROPHYLL STANDARDS BY ATOMIC-ABSORPTION SPECTROSCOPY. Biochimica Et Biophysica Acta 975: 384-394.

57. Ede NJ, Tregear GW, Haralambidis J (1994) Routine Preparation of Thiol Oligonucleotides: Application to the Synthesis of Oligonucleotide-Peptide Hybrids. Bioconjugate Chemistry 5: 373-378.

58. Williams BAR, Chaput JC (2010) Synthesis of Peptide-Oligonucleotide Conjugates Using a Heterobifunctional Crosslinker. Curent Protocols in Nucleic Acid Chemistry: 4.41.41-44.41.20.

59. Gut IG (2004) DNA Analysis by MALDI-TOF Mass Spectrometry. Human Mutation 23: 437-441.

60. Robertson SA, Harada K, Frankel AD, Wemmer DE (2000) Structure Determination and Binding Kinetics of a DNA Aptamer-Argininamide Complex. Biochemistry 39: 946-954.

61. Sauter C, Ng JD, Lorber B, Keith G, Brion P, et al. (1999) Additives for the crystallization of proteins and nucleic acids. Journal of Crystal Growth 196: 365-376.

62. Lipscomb LA, Peek ME, Morningstar ML, Verghis SM, Miller EM, et al. (1995) X-ray structure of a DNA decamer containing 7,8-dihydro-8-oxoguanine. Proceedings of the National Academy of Sciences 92: 719-723.

63. Scharer OD (2001) Chemical Biology of Mammalian DNA Repair. Chimia 55: 340-344.

64. Heideker J, Lis ET, Romesberg FE (2007) Phosphatases, DNA Damage Checkpoints and Checkpoint Deactivation. Cell Cycle 6: 3058-3064.

65. Garman E (2003) 'Cool' crystals: macromolecular cryocrystallography and radiation damage. Current Opinion in Structural Biology 13: 545-551.

66. Boutet S, Lomb L, Williams GJ, Barends TRM, Aquila A, et al. (2012) High-Resolution Protein Structure Determination by Serial Femtosecond Crystallography. Science 337: 362-364.

67. Chapman HN, Fromme P, al e (2011) Femtosecond X-Ray Protein Nanocrystallography. Nature 470: 73-78.

68. Gaffney KJ, Chapman HN (2007) Imaging atomic structure and dynamics with ultrafast X-ray scattering. Science 316: 1444-1448.

69. Greenfield NJ (2006) Using circular dichroism spectra to estimate protein secondary structure. Nature Protocols 1: 2876-2890.

70. Williams BAR, Lund K, Liu Y, Yan H, Chaput JC (2007) Self-Assembled Peptide Nanoarrays: An Approach to Studying Protein-Protein Interactions. Angewandte Chemie 46: 3051-3054.

71. Gibney BR, Dutton PL (1999) Histidine placement in de novo-designed heme proteins. Protein Science 8: 1888-1898.

72. Inuzuka T, Yun B-G, Ishikawa H, Takahashi S, Hori H, et al. (2004) Identification of Crucial Histidines for Heme Binding in the N-terminal Domain of the Heme-regulated eIF2α Kinase. Journal of Biological Chemistry 279: 6778-6782.

73. Cordova JM, Noack PL, Hilcove SA, Lear JD, Ghirlanda G (2007) Design of a Functional Membrane Protein by Engineering a Heme-Binding Site in Glycophorin A. Journal of the American Chemical Society 129: 512-518.

74. Walker FA, Lo M-W, Ree MT (1975) Electronic Effects in Transition Metal Porphyrins. The Reactions of Imidazoles and Pyridines with a Series of Para-Substituted Tetraphenylporphyrin Complexes of Chloroiron(III). Journal of the American Chemical Society 98: 5552-5560.

75. Bois-Poltoratsky R, Ehrenberg A (1967) Magnetic and Spectrophotometric Investigations of Cytochrome b5. European Journal of Biochemistry 2: 361-365.

76. Patra R, Sahoo D, Dey S, Sil D, Rath SP (2012) Switching Orientation of Two Axial Imidazole Ligands between Parallel and Perpendicular in Low-Spin Fe(III) and Fe(II) Nonplanar Porphyrinates. Inorganic Chemistry: A-L.

77. Romera C, Sabater L, Garofalo A, Dixon IM, Pratviel G (2010) Interaction of Cationic Nickel and Manganese Porphyrins with the Minor Groove of DNA. Inorganic Chemistry 49: 8558-8567.

APPENDIX A

20T FINE SCREEN 1

EXAMPLES OF FINE SCREEN SOLUTIONS USED IN 20T TETRAHEDRON CRYSTALLIZATION EXPERIMENTS

20T Fine Screen 1 – 10 mL screen solutions

50 mM sodium cacodylate pH 6.0, 20 mM L-argininamide, 30% PEG 1000
Stock solutions:

1. 1M sodium cacodylate pH 6.0
2. 1M L-argininamide
3. 50% PEG 1000

	33% PEG 1000	34% PEG 1000	35% PEG 1000	36% PEG 1000	37% PEG 1000	38% PEG 1000
10mM argininamide	.5 mL of cacodylate .1 mL argininamide 6.6 mL 33% PEG 1000 2.8 mL H_2O	.5 mL .1 mL, 6.8 mL 2.60 mL	.5 mL .1 mL 7 mL 2.40 mL	.5 mL .1 mL 7.2 mL 2.20 mL	.5 mL .1 mL 7.4 mL 2.0 mL	.5 mL .1 mL 7.6 mL 1.80 mL
15mM argininamide	.5 mL of cacodylate .15 mL argininamide 6.6 mL 33% PEG 1000 2.75 mL H_2O	.5 mL .15 mL 6.8 mL 2.55 mL	.5 mL .15 mL 7 mL 2. 35 mL	.5 mL .15 mL 7.2 mL 2.15 mL	.5 mL .15 mL 7.4 mL 1.95 mL	.5 mL .15 mL 7.6 mL 1.75 mL
20mM argininamide	.5 mL of cacodylate .2 mL argininamide 6.6 mL 33% PEG 1000 2.7 mL H_2O	.5 mL, .2 mL 6.8 mL 2.5 mL	.5 mL .2 mL 7mL 2.3 mL	.5 mL .2 mL 7.2 mL 2.1 mL	.5 mL .2 mL 7.4 mL 1.9 mL	.5 mL .2 mL 7.6 mL 1.7 mL
25mM argininamide	.5 mL of cacodylate .25 mL argininamide 6.6 mL 33% PEG 1000 2.65 mL H_2O	.5 mL .25 mL 6.8 mL 2.45 mL	.5 mL .25 mL 7 mL 2.25 mL	.5 mL .25 mL 7.2 mL 2.05 mL	.5 mL .25 mL 7.4 mL 1.85 mL	.5 mL .25 mL 7.6 mL 1.65 mL

APPENDIX B

20T FINE SCREEN 2

20T Fine Screen 2 - 10 mL screen solutions

50 mM sodium cacodylate pH 6.0, 20 mM L-argininamide, 30% PEG 1000

Stock solutions:

1. 1M sodium cacodylate pH 6.0
2. 1M L-argininamide
3. 50% PEG 1000

	23% PEG 1000	24% PEG 1000	25% PEG 1000	26% PEG 1000	27% PEG 1000	28% PEG 1000
argininamide 10mM	.5 mL of cacodylate .1 mL argininamide 4.6 mL 28% PEG 1000 4.8 mL H_2O	.5 mL .1 mL 4.8 mL 4.60 mL	.5 mL .1 mL 5 mL 4.40 mL	.5 mL .1 mL 5.2 mL 4.20 mL	.5 mL .1 mL 5.4 mL 4.00 mL	.5 mL .1 mL 5.6 mL 3.80 mL
argininamide 15mM	.5 mL of cacodylate .15 mL argininamide 4.6 mL 28% PEG 1000 4.75 mL H_2O	.5 mL .15 mL 4.8 mL 4.55 mL	.5 mL .15 mL 5 mL 4.35 mL	.5 mL .15 mL 5.2 mL 4.15 mL	.5 mL .15 mL 5.4 mL 3.95 mL	.5 mL .15 mL 5.6 mL 3.75 mL
argininamide 20mM	.5 mL of cacodylate .2 mL argininamide 4.6 mL 28% PEG 1000 4.7 mL H_2O	.5 mL, .2 mL 4.8 mL 4.50 mL	.5 mL .2 mL 5 mL 4.30 mL	.5 mL .2 mL 5.2 mL 4.10 mL	.5 mL .2 mL 5.4 mL 3.90 mL	.5 mL .2 mL 5.6 mL 3.70 mL
argininamide 25 mM	.5 mL of cacodylate .25 mL argininamide 4.6 mL 28% PEG 1000 4.65 mL H_2O	.5 mL .25 mL 4.8 mL 4.45 mL	.5 mL .25 mL 5 mL 4.25 mL	.5 mL .25 mL 5.2 mL 4.05 mL	.5 mL .25 mL 5.4 mL 3.85 mL	.5 mL .25 mL 5.6 mL 3.65 mL

APPENDIX C

20T FINE SCREEN 3

H11 Screen 3 - 10 mL screen solutions

H11 - 50 mM sodium cacodylate pH 6.0, 20 mM L-argininamide, 30% PEG 1000

Stock solutions:

1. 1M sodium cacodylate pH 6.0
2. 1M L-argininamide
3. 50% PEG 1000

	28% PEG 1000	30% PEG 1000	32% PEG 1000	34% PEG 1000	36% PEG 1000	38% PEG 1000
argininamide 10mM	.5 mL of cacodylate .1 mL argininamide 5.6 mL 28% PEG 1000 3.8 mL H_2O	.5 mL .1 mL 6 mL 3.4 mL	.5 mL .1 mL 6.4 mL 3 mL	.5 mL .1 mL 6.8 mL 2.6 mL	.5 mL .1 mL 7.2 mL 2.2 mL	.5 mL .1 mL 7.6 mL 1.8 mL
argininamide 15mM	.5 mL of cacodylate .15 mL argininamide 5.6 mL 28% PEG 1000 3.75 mL H_2O	.5 mL .15 mL 6 mL 3.35 mL	.5 mL .15 mL 6.4 mL 2.95 mL	.5 mL .15 mL 6.8 mL 2.55 mL	.5 mL .15 mL 7.2 mL 2.15 mL	.5 mL .15 mL 7.6 mL 1.75 mL
argininamide 20mM	.5 mL of cacodylate .2 mL argininamide 5.6 mL 28% PEG 1000 3.7 mL H_2O	.5 mL, .2 mL 6 mL 3.3 mL	.5 mL .2 mL 6.4 mL 2.9 mL	.5 mL .2 mL 6.8 mL 2.5 mL	.5 mL .2 mL 7.2 mL 2.1 mL	.5 mL .2 mL 7.6 mL 1.7 mL
argininamide 25 mM	.5 mL of cacodylate .25 mL argininamide 5.6 mL 28% PEG 1000 3.65 mL H_2O	.5 mL .25 mL 6 mL 3.25 mL	.5 mL .25 mL 6.4 mL 2.85 mL	.5 mL .25 mL 6.8 mL 2.45 mL	.5 mL .25 mL 7.2 mL 2.05 mL	.5 mL .25 mL 7.6 mL 1.65 mL

APPENDIX D

20T FINE SCREEN 4

20T Fine Screen 4 – 10 mL screen solutions - 50 mM Cacodylate pH 6.0, 1M Argininamide, 29-34% PEG 1000

Stock solutions:

1. 0.5M sodium cadodylate pH 6.0
2. 1M L-argininamide
3. 50% PEG 1000

	29% PEG 1000	30% PEG 1000	31% PEG 1000	32% PEG 1000	33% PEG 1000	34% PEG 1000
argininamide 10mM	.5 mL of cacodylate .1 mL argininamide 5.8 mL 50% PEG 1000 3.6 mL H_2O	.5 mL .1 mL 6.0 mL 3.4 mL	.5 mL .1 mL 6.2 mL 3.2 mL	.5 mL .1 mL 6.4 mL 3 mL	.5 mL .1 mL 6.6 mL 2.8 mL	.5 mL .1 mL 6.8 mL 2.6 mL
argininamide 15mM	.5 mL of cacodylate .15 mL argininamide 5.8 mL 50% PEG 1000 3.55 mL H_2O	.5 mL .15 mL 6.0 mL 3.35 mL	.5 mL .15 mL 6.2 mL 3.15 mL	.5 mL .15 mL 6.4 mL 2.95 mL	.5 mL .15 mL 6.6 mL 2.75 mL	.5 mL .15 mL 6.8 mL 2.55 mL
argininamide 20mM	.5 mL of cacodylate .2 mL argininamide 5.8 mL 50% PEG 1000 3.5 mL H_2O	.5 mL, .2 mL 6.0 mL 3.3 mL	.5 mL .2 mL 6.2 mL 3.1 mL	.5 mL .2 mL 6.4 mL 2.9 mL	.5 mL .2 mL 6.6 mL 2.7 mL	.5 mL .2 mL 6.8 mL 2.5 mL
argininamide 25mM	.5 mL of cacodylate .25 mL argininamide 5.8 mL 50% PEG 1000 3.45 mL H_2O	.5 mL .25 mL 6.0 mL 3.25 mL	.5 mL .25 mL 6.2 mL 3.05 mL	.5 mL .25 mL 6.4 mL 2.85 mL	.5 mL .25 mL 6.6 mL 2.65 mL	.5 mL .25 mL 6.8 mL 2.45 mL

APPENDIX E

20T FINE SCREEN 5a

20T Fine Screen 5a (TRIS)- 10 mL screen solutions - 50 mM MES pH 6.0, 50 mM Tris pH 7.0, 50 mM Tris pH 8.0, 50 mM Tris pH 9.0, 15 mM Argininamide, 18-28% PEG 1000

Stock solutions:

1. 0.5M MES pH 6.0
2. 0.5M Tris pH 7.0
3. 0.5M Tris pH 8.0
4. 0.5M Tris pH 9.0
5. 1M Argininamide
6. 50% PEG 1000

	18% PEG 1000	20% PEG 1000	22% PEG 1000	24% PEG 1000	26% PEG 1000	28% PEG 1000
MES pH 6.0 50mM	.5 mL of MES .15 mL Argininamide 3.6 mL 50% PEG 1000 5.75 mL H_2O	.5 mL .15 mL 4.0 mL 5.35 mL	.5 mL .15 mL 4.4 mL 4.95 mL	.5 mL .15 mL 4.8 mL 4.55 mL	.5 mL .15 mL 5.2 mL 4.15 mL	.5 mL .15 mL 5.6 mL 3.75 mL
Tris pH 7.0 50mM	.5 mL of Tris pH 7.0 .15 mL Argininamide 3.6 mL 50% PEG 1000 5.75 mL H_2O	.5 mL .15 mL 4.0 mL 5.35 mL	.5 mL .15 mL 4.4 mL 4.95 mL	.5 mL .15 mL 4.8 mL 4.55 mL	.5 mL .15 mL 5.2 mL 4.15 mL	.5 mL .15 mL 5.6 mL 3.75 mL
Tris pH 8.0 50mM	.5 mL of Tris pH 8.0 .15 mL Argininamide 3.6 mL 50% PEG 1000 5.75 mL H_2O	.5 mL, .15 mL 4.0 mL 5.35 mL	.5 mL .15 mL 4.4 mL 4.95 mL	.5 mL .15 mL 4.8 mL 4.55 mL	.5 mL .15 mL 5.2 mL 4.15 mL	.5 mL .15 mL 5.6 mL 3.75 mL
Tris pH 9.0 50 mM	.5 mL of Tris pH 9.0 .15 mL Argininamide 3.6 mL 50% PEG 1000 5.75 mL H_2O	.5 mL .15 mL 4.0 mL 5.35 mL	.5 mL .15 mL 4.4 mL 4.95 mL	.5 mL .15 mL 4.8 mL 4.55 mL	.5 mL .15 mL 5.2 mL 4.15 mL	.5 mL .15 mL 5.6 mL 3.75 mL

APPENDIX F

20T FINE SCREEN 5b

20T Fine Screen 5b (TRIS)- 10 mL screen solutions - 50 mM MES pH 6.0, 50 mM Tris pH 7.0, 50 mM Tris pH 8.0, 50 mM Tris pH 9.0, 15 mM Argininamide, 30-40% PEG 1000

Stock solutions:

1. 0.5M MES pH 6.0
2. 0.5M Tris pH 7.0
3. 0.5M Tris pH 8.0
4. 0.5M Tris pH 9.0
5. 1M L-argininamide
6. 50% PEG 1000

	30% PEG 1000	32% PEG 1000	34% PEG 1000	36% PEG 1000	38% PEG 1000	40% PEG 1000
MES pH 6.0 50mM	.5 mL of MES .15 mL Argininamide 6.0 mL 50% PEG 1000 3.35 mL H_2O	.5 mL .15 mL 6.4 mL 2.95 mL	.5 mL .15 mL 6.8 mL 2.55 mL	.5 mL .15 mL 7.2 mL 2.15 mL	.5 mL .15 mL 7.6 mL 1.75 mL	.5 mL .15 mL 8.0 mL 1.35 mL
Tris pH 7.0 50mM	.5 mL of Tris pH 7.0 .15 mL Argininamide 6.0 mL 50% PEG 1000 3.35 mL H_2O	.5 mL .15 mL 6.4 mL 2.95 mL	.5 mL .15 mL 6.8 mL 2.55 mL	.5 mL .15 mL 7.2 mL 2.15 mL	.5 mL .15 mL 7.6 mL 1.75 mL	.5 mL .15 mL 5.6 mL 3.75 mL
Tris pH 8.0 50mM	.5 mL of Tris pH 8.0 .15 mL Argininamide 6.0 mL 50% PEG 1000 3.35 mL H_2O	.5 mL, .15 mL 6.4 mL 2.95 mL	.5 mL .15 mL 6.8 mL 2.55 mL	.5 mL .15 mL 7.2 mL 2.15 mL	.5 mL .15 mL 7.6 mL 1.75 mL	.5 mL .15 mL 5.6 mL 3.75 mL
Tris pH 9.0 50 mM	.5 mL of Tris pH 9.0 .15 mL Argininamide 6.0 mL 50% PEG 1000 3.35 mL H_2O	.5 mL .15 mL 6.4 mL 2.95 mL	.5 mL .15 mL 6.8 mL 2.55 mL	.5 mL .15 mL 7.2 mL 2.15 mL	.5 mL .15 mL 7.6 mL 1.75 mL	.5 mL .15 mL 5.6 mL 3.75 mL

APPENDIX G

20T FINE SCREEN 6a

20T Fine Screen 6a (TRIS + cacodylate)- 10 mL screen solutions - 50 mM MES + 50 mM Cacodylate pH 6.0, 50 mM Tris + 50 mM Cacodylate pH 7.0, 50 mM Tris + 50mM Cacodylate pH 8.0, 50 mM Tris + 50mM Cacodylate pH 9.0, 15 mM Argininamide, 18-28% PEG 1000

Stock solutions:

1. 0.5M MES + 0.5M Cacodylate pH 6.0
2. 0.5M Tris + 0.5M Cacodylate pH 7.0
4. 0.5M Tris + 0.5M Cacodylate pH 8.0
5. 0.5M Tris + 0.5M Cacodylate pH 9.0
6. 1M Argininamide
7. 50% PEG 1000

	18% PEG 1000	20% PEG 1000	22% PEG 1000	24% PEG 1000	26% PEG 1000	28% PEG 1000
MES + Cacodylate pH 6.0 50mM	.5 mL of MES + Caco .15 mL Argininamide 3.6 mL 50% PEG 1000 5.75 mL H_2O	.5 mL .15 mL 4.0 mL 5.35 mL	.5 mL .15 mL 4.4 mL 4.95 mL	.5 mL .15 mL 4.8 mL 4.55 mL	.5 mL .15 mL 5.2 mL 4.15 mL	.5 mL .15 mL 5.6 mL 3.75 mL
Tris + Cacodylate pH 7.0 50mM	.5 mL of Tris + Caco pH 7.0 .15 mL Argininamide 3.6 mL 50% PEG 1000 5.75 mL H_2O	.5 mL .15 mL 4.0 mL 5.35 mL	.5 mL .15 mL 4.4 mL 4.95 mL	.5 mL .15 mL 4.8 mL 4.55 mL	.5 mL .15 mL 5.2 mL 4.15 mL	.5 mL .15 mL 5.6 mL 3.75 mL
Tris + Cacodylate pH 8.0 50mM	.5 mL of Tris + Caco pH 8.0 .15 mL Argininamide 3.6 mL 50% PEG 1000 5.75 mL H_2O	.5 mL, .15 mL 4.0 mL 5.35 mL	.5 mL .15 mL 4.4 mL 4.95 mL	.5 mL .15 mL 4.8 mL 4.55 mL	.5 mL .15 mL 5.2 mL 4.15 mL	.5 mL .15 mL 5.6 mL 3.75 mL
Tris + Cacodylate pH 9.0 50mM	.5 mL of Tris + Caco pH 9.0 .15 mL Argininamide 3.6 mL 50% PEG 1000 5.75 mL H_2O	.5 mL .15 mL 4.0 mL 5.35 mL	.5 mL .15 mL 4.4 mL 4.95 mL	.5 mL .15 mL 4.8 mL 4.55 mL	.5 mL .15 mL 5.2 mL 4.15 mL	.5 mL .15 mL 5.6 mL 3.75 mL

APPENDIX H

20T FINE SCREEN 6b

20T Fine Screen 6b (TRIS + Cacodylate)- 10 mL screen solutions - 50 mM MES + 50mM Cacodylate pH 6.0, 50 mM Tris + 50mM Cacodylate pH 7.0, 50 mM Tris + 50mM Cacodylate pH 8.0, 50 mM Tris + 50mM Cacodylate pH 9.0, 15 mM Argininamide, 30-40% PEG 1000

Stock solutions:

1. 0.5M MES + 0.5M Cacodylate pH 6.0
2. 0.5M Tris + 0.5M Cacodylate pH 7.0
3. 0.5M Tris + 0.5M Cacodylate pH 8.0
4. 0.5M Tris + 0.5M Cacodylate pH 9.0
5. 1M Argininamide
6. 50% PEG 1000

	30% PEG 1000	32% PEG 1000	34% PEG 1000	36% PEG 1000	38% PEG 1000	40% PEG 1000
MES + Cacodylate pH 6.0 50mM	.5 mL of MES + Caco .15 mL Argininamide 6.0 mL 50% PEG 1000 3.35 mL H_2O	.5 mL .15 mL 6.4 mL 2.95 mL	.5 mL .15 mL 6.8 mL 2.55 mL	.5 mL .15 mL 7.2 mL 2.15 mL	.5 mL .15 mL 7.6 mL 1.75 mL	.5 mL .15 mL 8.0 mL 1.35 mL
Tris + Cacodylate pH 7.0 50mM	.5 mL of Tris + Caco pH 7.0 .15 mL Argininamide 6.0 mL 50% PEG 1000 3.35 mL H_2O	.5 mL .15 mL 6.4 mL 2.95 mL	.5 mL .15 mL 6.8 mL 2.55 mL	.5 mL .15 mL 7.2 mL 2.15 mL	.5 mL .15 mL 7.6 mL 1.75 mL	.5 mL .15 mL 5.6 mL 3.75 mL
Tris + Cacodylate pH 8.0 50mM	.5 mL of Tris + Caco pH 8.0 .15 mL Argininamide 6.0 mL 50% PEG 1000 3.35 mL H_2O	.5 mL, .15 mL 6.4 mL 2.95 mL	.5 mL .15 mL 6.8 mL 2.55 mL	.5 mL .15 mL 7.2 mL 2.15 mL	.5 mL .15 mL 7.6 mL 1.75 mL	.5 mL .15 mL 5.6 mL 3.75 mL
Tris + Cacodylate pH 9.0 50 mM	.5 mL of Tris + Caco pH 9.0 .15 mL Argininamide 6.0 mL 50% PEG 1000 3.35 mL H_2O	.5 mL .15 mL 6.4 mL 2.95 mL	.5 mL .15 mL 6.8 mL 2.55 mL	.5 mL .15 mL 7.2 mL 2.15 mL	.5 mL .15 mL 7.6 mL 1.75 mL	.5 mL .15 mL 5.6 mL 3.75 mL

APPENDIX I

20T FINE SCREEN 7a

20T Fine Screen 7a (New Buffers)- 10 mL screen solutions - 50 mM MES pH 6.0, 50 mM HEPES pH 7.0, 50 mM Tris pH 8.0, 50 mM Tris pH 9.0, 15 mM Argininamide, 18-28% PEG 1000

Stock solutions:

1. 0.5M MES pH 6.0
2. 0.5M HEPES pH 7.0
3. 0.5M Tris pH 8.0
4. 0.5M Tris pH 9.0
5. 1M Argininamide
6. 50% PEG 1000

	18% PEG 1000	20% PEG 1000	22% PEG 1000	24% PEG 1000	26% PEG 1000	28% PEG 1000
MES pH 6.0 50mM	.5 mL of MES .15 mL Argininamide 3.6 mL 50% PEG 1000 5.75 mL H_2O	.5 mL .15 mL 4.0 mL 5.35 mL	.5 mL .15 mL 4.4 mL 4.95 mL	.5 mL .15 mL 4.8 mL 4.55 mL	.5 mL .15 mL 5.2 mL 4.15 mL	.5 mL .15 mL 5.6 mL 3.75 mL
HEPES pH 7.0 50mM	.5 mL of HEPES pH 7.0 .15 mL Argininamide 3.6 mL 50% PEG 1000 5.75 mL H_2O	.5 mL .15 mL 4.0 mL 5.35 mL	.5 mL .15 mL 4.4 mL 4.95 mL	.5 mL .15 mL 4.8 mL 4.55 mL	.5 mL .15 mL 5.2 mL 4.15 mL	.5 mL .15 mL 5.6 mL 3.75 mL
Tris pH 8.0 50mM	.5 mL of Tris pH 8.0 .15 mL Argininamide 3.6 mL 50% PEG 1000 5.75 mL H_2O	.5 mL, .15 mL 4.0 mL 5.35 mL	.5 mL .15 mL 4.4 mL 4.95 mL	.5 mL .15 mL 4.8 mL 4.55 mL	.5 mL .15 mL 5.2 mL 4.15 mL	.5 mL .15 mL 5.6 mL 3.75 mL
Tris pH 9.0 50 mM	.5 mL of Tris pH 9.0 .15 mL Argininamide 3.6 mL 50% PEG 1000 5.75 mL H_2O	.5 mL .15 mL 4.0 mL 5.35 mL	.5 mL .15 mL 4.4 mL 4.95 mL	.5 mL .15 mL 4.8 mL 4.55 mL	.5 mL .15 mL 5.2 mL 4.15 mL	.5 mL .15 mL 5.6 mL 3.75 mL

APPENDIX J

20T FINE SCREEN 7b

20T Fine Screen 7b (New Buffers)- 10 mL screen solutions - 50 mM MES pH 6.0, 50 mM HEPES pH 7.0, 50 mM Tris pH 8.0, 50 mM Tris pH 9.0, 15 mM Argininamide, 30-40% PEG 1000

Stock solutions:

1. 0.5M MES pH 6.0
2. 0.5M HEPES pH 7.0
3. 0.5M Tris pH 8.0
4. 0.5M Tris pH 9.0
5. 1M Argininamide
6. 50% PEG 1000

	30% PEG 1000	32% PEG 1000	34% PEG 1000	36% PEG 1000	38% PEG 1000	40% PEG 1000
MES pH 6.0 50mM	.5 mL of MES .15 mL Argininamide 6.0 mL 50% PEG 1000 3.35 mL H_2O	.5 mL .15 mL 6.4 mL 2.95 mL	.5 mL .15 mL 6.8 mL 2.55 mL	.5 mL .15 mL 7.2 mL 2.15 mL	.5 mL .15 mL 7.6 mL 1.75 mL	.5 mL .15 mL 8.0 mL 1.35 mL
Tris pH 7.0 50mM	.5 mL of HEPES pH 7.0 .15 mL Argininamide 6.0 mL 50% PEG 1000 3.35 mL H_2O	.5 mL .15 mL 6.4 mL 2.95 mL	.5 mL .15 mL 6.8 mL 2.55 mL	.5 mL .15 mL 7.2 mL 2.15 mL	.5 mL .15 mL 7.6 mL 1.75 mL	.5 mL .15 mL 5.6 mL 3.75 mL
Tris pH 8.0 50mM	.5 mL of Tris pH 8.0 .15 mL Argininamide 6.0 mL 50% PEG 1000 3.35 mL H_2O	.5 mL, .15 mL 6.4 mL 2.95 mL	.5 mL .15 mL 6.8 mL 2.55 mL	.5 mL .15 mL 7.2 mL 2.15 mL	.5 mL .15 mL 7.6 mL 1.75 mL	.5 mL .15 mL 5.6 mL 3.75 mL
Tris pH 9.0 50 mM	.5 mL of Tris pH 9.0 .15 mL Argininamide 6.0 mL 50% PEG 1000 3.35 mL H_2O	.5 mL .15 mL 6.4 mL 2.95 mL	.5 mL .15 mL 6.8 mL 2.55 mL	.5 mL .15 mL 7.2 mL 2.15 mL	.5 mL .15 mL 7.6 mL 1.75 mL	.5 mL .15 mL 5.6 mL 3.75 mL

APPENDIX K

20T FINE SCREEN 8

20T Fine Screen 8 - New Salts + different pHs (NO ARGININAMIDE—ONLY $Mg(Ac)_2$ – 10 mL screen solutions - 50 mM Tris pH 7.0, 50mM Tris pH 9.0, 50mM Tris + 50mM Cacodylate pH 7.0, 50mM Tris + 50mM Cacodylate pH 9.0, 15 mM $Mg(Ac)_2$, 29-34% PEG 1000

Stock solutions:

1. 0.5M Tris pH 7.0
2. 0.5M Tris pH 9.0
3. 0.5M Tris + 0.5M Cacodylate pH 7.0
4. 0.5M Tris + 0.5M Cacodylate pH 9.0
5. 1M Magnesium acetate
6. 50% PEG 1000

	29% PEG 1000	30% PEG 1000	31% PEG 1000	32% PEG 1000	33% PEG 1000	34% PEG 1000
Tris pH 7.0 50mM	.5 mL of Tris pH 7.0 .15 mL $Mg(Ac)_2$ 5.8 mL 50% PEG 1000 3.55 mL H_2O	.5 mL .15 mL 6.0 mL 3.35 mL	.5 mL .15 mL 6.2 mL 3.15 mL	.5 mL .15 mL 6.4 mL 2.95 mL	.5 mL .15 mL 6.6 mL 2.75 mL	.5 mL .15 mL 6.8 mL 2.55 mL
Tris pH 9.0 50mM	.5 mL of Tris pH 9.0 .15 mL $Mg(Ac)_2$ 5.8 mL 50% PEG 1000 3.55 mL H_2O	.5 mL .15 mL 6.0 mL 3.35 mL	.5 mL .15 mL 6.2 mL 3.15 mL	.5 mL .15 mL 6.4 mL 2.95 mL	.5 mL .15 mL 6.6 mL 2.75 mL	.5 mL .15 mL 6.8 mL 2.55 mL
Tris + Cacodylate pH 7.0 50mM	.5 mL of Tris + Caco pH 7.0 .15 mL $Mg(Ac)_2$ 5.8 mL 50% PEG 1000 3.55 mL H_2O	.5 mL, .15 mL 6.0 mL 3.35 mL	.5 mL .15 mL 6.2 mL 3.15 mL	.5 mL .15 mL 6.4 mL 2.95 mL	.5 mL .15 mL 6.6 mL 2.75 mL	.5 mL .15 mL 6.8 mL 2.55 mL
Tris + Cacodylate pH 9.0 50 mM	.5 mL of Tris + Caco pH 9.0 .15 mL $Mg(Ac)_2$ 5.8 mL 50% PEG 1000 3.55 mL H_2O	.5 mL .15 mL 6.0 mL 3.35 mL	.5 mL .15 mL 6.2 mL 3.15 mL	.5 mL .15 mL 6.4 mL 2.95 mL	.5 mL .15 mL 6.6 mL 2.75 mL	.5 mL .15 mL 6.8 mL 2.55 mL

APPENDIX L

20T FINE SCREEN 9

20T Fine Screen 9 - New Salts + different pHs (50% ARGININAMIDE + 50% $Mg(Ac)_2$) – 10 mL screen solutions - 50 mM Tris pH 7.0, 50mM Tris pH 9.0, 50mM Tris + 50mM Cacodylate pH 7.0, 50mM Tris + 50mM Cacodylate pH 9.0, 7.5 mM $Mg(Ac)_2$, 7.5 mM Argininamide, 29-34% PEG 1000

Stock solutions:

1. 0.5M Tris pH 7.0
2. 0.5M Tris pH 9.0
3. 0.5M Tris + 0.5M Cacodylate pH 7.0
4. 0.5M Tris + 0.5M Cacodylate pH 9.0
5. 1M Magnesium acetate
6. 1M L-Argininamide
7. 50% PEG 1000

	29% PEG 1000	30% PEG 1000	31% PEG 1000	32% PEG 1000	33% PEG 1000	34% PEG 1000
	.5 mL of Na-caco pH 6.0 .05 mL $Mg(Ac)_2$					
	.05 mL	.5 mL	.5 mL	.5 mL	.5 mL	.5 mL
5mM	Argininamide	.05 mL	.05 mL	.05 mL	.05 mL	.05 mL
Argininamide	5.8 mL 50%	.05 mL	.05 mL	.05 mL	.05 mL	.05 mL
+	PEG 1000	6.0 mL	6.2 mL	6.4 mL	6.6 mL	6.8 mL
5mM $Mg(Ac)_2$	3.6 mL H_2O	3.4 mL	3.2 mL	3.0 mL	2.8 mL	2.6 mL
	.5 mL of Na-caco pH 6.0 .15 mL $Mg(Ac)_2$					
	5.8 mL 50%	.5 mL	.5 mL	.5 mL	.5 mL	.5 mL
15mM	PEG 1000	.15 mL	.15 mL	.15 mL	.15 mL	.15 mL
$Mg(Ac)_2$	3.55 mL H_2O	6.0 mL	6.2 mL	6.4 mL	6.6 mL	6.8 mL
		3.35 mL	3.15 mL	2.95 mL	2.75 mL	2.55 mL
	.5 mL of Na-caco pH 6.0 .1 mL $Mg(Ac)_2$					
10mM	.1 mL	.5 mL,	.5 mL	.5 mL	.5 mL	.5 mL
Argininamide	Argininamide	.1 mL	.1 mL	.1 mL	.1 mL	.1 mL
+	5.8 mL 50%	.1 mL	.1 mL	.1 mL	.1 mL	.1 mL
10mM	PEG 1000	6.0 mL	6.2 mL	6.4 mL	6.6 mL	6.8 mL
$Mg(Ac)_2$	3.5 mL H_2O	3.3 mL	3.1 mL	2.9 mL	2.7 mL	2.5 mL
	.5 mL of Na-caco pH 6.0 .25 mL $Mg(Ac)_2$					
	5.8 mL 50%	.5 mL	.5 mL	.5 mL	.5 mL	.5 mL
25mM	PEG 1000	.25 mL	.25 mL	.25 mL	.25 mL	.25 mL
$Mg(Ac)_2$	3.45 mL H_2O	6.0 mL	6.2 mL	6.4 mL	6.6 mL	6.8 mL
		3.25 mL	3.05 mL	2.85 mL	2.65 mL	2.45 mL

APPENDIX M

20T FINE SCREEN 10

20T Fine Screen 10 - New Salts + old conditions of Screen 4 (Argininamide + $Mg(Ac)_2$ as salts) – 10 mL screen solutions - 50 mM Na-cacodylate pH 6.0, varying [ ] of $Mg(Ac)_2$ and Argininamide, 29-34% PEG 1000

Stock solutions:

1. 0.5M Sodium cacodylate pH 6.0 (buffer)
2. 1M Magnesium acetate (salt)
3. 1M L-Argininamide (salt)
4. 50% PEG 1000 (ppt)

	29% PEG 1000	30% PEG 1000	31% PEG 1000	32% PEG 1000	33% PEG 1000	34% PEG 1000
Tris pH 7.0 50mM	.5 mL of Tris pH 7.0 .075 mL $Mg(Ac)_2$ .075 mL Argininamide 5.8 mL 50% PEG 1000 3.55 mL H_2O	.5 mL .075 mL .075 mL 6.0 mL 3.35 mL	.5 mL .075 mL .075 mL 6.2 mL 3.15 mL	.5 mL .075 mL .075 mL 6.4 mL 2.95 mL	.5 mL .075 mL .075 mL 6.6 mL 2.75 mL	.5 mL .075 mL .075 mL 6.8 mL 2.55 mL
Tris pH 9.0 50mM	.5 mL of Tris pH 9.0 .075 mL $Mg(Ac)_2$ .075 mL Argininamide 5.8 mL 50% PEG 1000 3.55 mL H_2O	.5 mL .075 mL .075 mL 6.0 mL 3.35 mL	.5 mL .075 mL .075 mL 6.2 mL 3.15 mL	.5 mL .075 mL .075 mL 6.4 mL 2.95 mL	.5 mL .075 mL .075 mL 6.6 mL 2.75 mL	.5 mL .075 mL .075 mL 6.8 mL 2.55 mL
Tris + Cacodylate pH 7.0 50mM	.5 mL of Tris + Caco pH 7.0 .075 mL $Mg(Ac)_2$ .075 mL Argininamide 5.8 mL 50% PEG 1000 3.55 mL H_2O	.5 mL, .075 mL .075 mL 6.0 mL 3.35 mL	.5 mL .075 mL .075 mL 6.2 mL 3.15 mL	.5 mL .075 mL .075 mL 6.4 mL 2.95 mL	.5 mL .075 mL .075 mL 6.6 mL 2.75 mL	.5 mL .075 mL .075 mL 6.8 mL 2.55 mL
Tris + Cacodylate pH 9.0 50 mM	.5 mL of Tris + Caco pH 9.0 .075 mL $Mg(Ac)_2$ .075 mL Argininamide 5.8 mL 50% PEG 1000 3.55 mL H_2O	.5 mL .075 mL .075 mL 6.0 mL 3.35 mL	.5 mL .075 mL .075 mL 6.2 mL 3.15 mL	.5 mL .075 mL .075 mL 6.4 mL 2.95 mL	.5 mL .075 mL .075 mL 6.6 mL 2.75 mL	.5 mL .075 mL .075 mL 6.8 mL 2.55 mL

APPENDIX N

20T FINE MINI SCREEN 11

20T Fine Mini-Screen 11

Stock solutions:
50% (w/w) PEG-1000
1M $MgSO_4$
1M L-argininamide
1M sodium cacodylate pH 6.0
0.5M Tris pH 9.0

(1) 29% PEG-1000 5mM argininamide 5mM $MgSO_4$ 50mM sodium cacodylate pH 6.0	5.8 mL PEG-1000 50 μL argininamide 50 μL $MgSO_4$ 500 μL sodium cacodylate 3.6 mL H_2O
(2) 29% PEG-1000 10mM argininamide 10mM $MgSO_4$ 50mM sodium cacodylate pH 6.0	5.8 mL 100 μL 100 μL 500 μL 3.5 mL H_2O
(3) 29% PEG-1000 20mM $MgSO_4$ 50mM Tris pH 9.0	5.8 mL 200 μL 1 mL 3 mL H_2O
(4) 30% PEG-1000 50mM Tris pH 9.0 7.5mM argininamide 7.5mM $MgSO_4$	6.0 mL 1 mL 75 μL 75 μL 2.85 mL H_2O